2019

Allosteric Functionality In Mechanical And Flow Networks

Jason William Rocks
University of Pennsylvania, jasonwillyrocks@gmail.com

Allosteric Functionality In Mechanical And Flow Networks

Abstract

Functionally optimized networks abound in nature, efficiently and precisely controlling the propagation of inputs to perform specific tasks. The regulation of protein activity via allostery presents one of the most well-studied examples: such proteins utilize specific conformational or dynamical changes upon the binding of ligands to facilitate communication between distant active sites. Venation networks in animals, plants, fungi and slime molds also display a type of allosteric communication, having the ability to precisely distribute oxygen and nutrients from a limited number of inputs to locally support growth and activity. Whether via genetic evolution or dynamic adaptation, many of these networks are able to create and control allosteric functionality by locally tuning interactions between nodes. Taking inspiration from this ability to regulate function, we approach allostery as a problem in metamaterials design, asking whether it is possible to create synthetic mechanical and flow networks with allosteric properties. We show that not only is this possible, but is remarkably easy, only requiring a small percentage of interactions in a network to be tuned. Leveraging the large statistical ensembles of allosteric networks generated in this way, we show that the limits of multifinctionality in both flow and mechanical networks are governed by the same constraint satisfaction phase transition, unifying both systems into a single theoretical framework. Finally, we investigate the underlying mechanisms by which allosteric function is created in flow networks. We show that the relationship between structure and function in flow networks is topological in nature, not depending on local details of the network architecture. The approaches presented in this work for studying allostery in both flow and mechanical networks set the blueprint for understanding and controlling general functional complex networks.

Degree Type

Dissertation

Degree Name

Doctor of Philosophy (PhD)

Graduate Group

Physics & Astronomy

First Advisor

Andrea J. Liu

Keywords

allostery, flow netoworks, mechanical networks, metamaterials, network optimization, persistent homology

Subject Categories

Physics

ALLOSTERIC FUNCTIONALITY IN MECHANICAL AND FLOW NETWORKS

Jason W. Rocks

A DISSERTATION

in

Physics and Astronomy

Presented to the Faculties of the University of Pennsylvania
in
Partial Fulfillment of the Requirements for the
Degree of Doctor of Philosophy

2019

Andrea J. Liu, Ph.D., Professor of Physics and Astronomy
Supervisor of Dissertation

Joshua R. Klein, Ph.D., Professor of Physics and Astronomy
Graduate Group Chairperson

Dissertation Committee:
Douglas J. Durian, Ph.D., Professor of Physics and Astronomy
Randall D. Kamien, Ph.D., Professor of Physics and Astronomy
Eleni Katifori, Ph.D., Assistant Professor of Physics and Astronomy
Ravi Radhakrishnan, Ph.D., Professor of Bioengineering and Chemical and Biomolecular Engineering

Dedication

For my grandmother

Acknowledgments

I will remember my time in graduate school fondly due to the large number of wonderful people who have provided me with guidance and support over the years. First and foremost, I would like to thank my advisor, Andrea Liu. She has been an incredibly supportive mentor, both through the good times and the bad, helping to shape me into both the scientist and the person I am today. Among the many things she has taught me, one piece of advice in particular will stick with me no matter what my futures holds: the most important key to success in science is to work on what you enjoy. I am profoundly grateful that she has been able to overcome the harsh obstacles she faced in the last few years, and I hope she will continue to be a cornerstone of my academic life.

I want to thank Eleni Katifori for essentially playing the role of my unofficial advisor when Andrea was unavailable. At a time when my research felt grueling and stale, she helped to push me in new scientific directions, reinvigorating my excitement and enthusiasm for science. Since then she has been a wealth of advice and support. I would also like to thank Randy Kamien for making the soft matter theory community

at Penn feel like a family. I always appreciated his sense of humor as a self-proclaimed "social misanthrope" and his ability to create such a light-hearted atmosphere. He provided me with a lot of guidance and support, teaching me how to cut through the BS in life. In addition, I want to thank the the other members of my thesis committee, Doug Durian and Ravi Radhakrishnan, for graciously giving me their time and advice.

I am extremely lucky to have been a part of the soft matter community at Penn. It is a truly special place both academically and socially. I want to thank everyone with whom I had the pleasure of knowing and working with here. In particular, I would like to thank Kevin Chiou and Carl Goodrich, both of whom were exceptionally generous and patient with me when I first started graduate school. I learned a lot of from both of them and really appreciated that they took me under their wings, providing guidance on some of my first research projects. I also want to thank Henrik Ronellenfitsch and Sean Ridout for being a pleasure to collaborate with. There are many, many, many more people that I would like to thank, but I would like to keep this relatively short, so I will once again thank everyone that has passed through this community in the last six years for providing me with a place to thrive.

Thanks to Sid Nagel for also helping me learn how to navigate the first research project in which I had a lead role. I have always appreciated his input and advice as both a mentor and collaborator. Also, thanks to Nidhi Pashine and Irmgard Bischofberger for being wonderful people to work with and providing me with amazing experimental support.

I want to thank my family and friends for always being there for me. Bill Balunas and Johanna-Laina Fischer, you will always be two of my closest friends. You provided me with some of my happiest memories and I hope that we remain close friends into the far future. Thank you to my siblings, Rachel and Brian Rocks - I'm proud of you both and will always be supportive of you, just as you have been supportive of me. I want to thank my grandmother, Jean Greenblatt. She taught me to always see humor in life and I will miss her deeply. Mom and Dad – to be honest, I get a little teary-eyed writing this – thank you for everything. You two are the main reason I am the person who I am today. You have always done everything possible to support me at every step of my life. I am proud to be your son and love both of you from the bottom of my heart. Finally, I want to thank my partner, Katie Siewert. Thank you for always being a source of reason and inspiration in my life, helping me to be the best person I can be. I am lucky to have had someone so special to share this journey with.

ABSTRACT

ALLOSTERIC FUNCTIONALITY IN MECHANICAL AND FLOW NETWORKS

Jason W. Rocks

Andrea J. Liu, Ph.D.

Functionally optimized networks abound in nature, efficiently and precisely controlling the propagation of inputs to perform specific tasks. The regulation of protein activity via allostery presents one of the most well-studied examples: such proteins utilize specific conformational or dynamical changes upon the binding of ligands to facilitate communication between distant active sites. Venation networks in animals, plants, fungi and slime molds also display a type of allosteric communication, having the ability to precisely distribute oxygen and nutrients from a limited number of inputs to locally support growth and activity. Whether via genetic evolution or dynamic adaptation, many of these networks are able to create and control allosteric functionality by locally tuning interactions between nodes. Taking inspiration from this ability to regulate function, we approach allostery as a problem in metamaterials design, asking whether it is possible to create synthetic mechanical and flow networks with allosteric properties. We show that not only is this possible, but is remarkably easy, only requiring a small percentage of interactions in a network to be tuned. Leveraging the large statistical ensembles of allosteric networks generated in

this way, we show that the limits of multifinctionality in both flow and mechanical networks are governed by the same constraint satisfaction phase transition, unifying both systems into a single theoretical framework. Finally, we investigate the underlying mechanisms by which allosteric function is created in flow networks. We show that the relationship between structure and function in flow networks is topological in nature, not depending on local details of the network architecture. The approaches presented in this work for studying allostery in both flow and mechanical networks set the blueprint for understanding and controlling general functional complex networks.

Contents

List of Tables

List of Figures

Chapter 1

Introduction

The term *allostery* was originally coined in 1961 by Monod and Jacob [46] to describe the inhibition of proteins "where the inhibitor is not a steric analogue of the substrate [8]." Accordingly, it is composed of two Greek roots: *allos*, meaning "other" or "different" and *stereos*, meaning "solid" or "body", signifying the "difference in specificity of the two binding sites for regulatory effector and for substrate [8]." Since its conception, allostery has become a central focus in molecular biology, arriving at its modern definition as "the process by which biological macromolecules (mostly proteins) transmit the effect of binding at one site to another, often distal, functional site, allowing for regulation of activity [47]."

Although allosteric proteins are ubiquitous in nature, with some even claiming that all proteins are allosteric to some extent [31], a general theory of protein allostery remains elusive [47]. The wide variation in observed allosteric mechanisms, along with

the structural complexity inherent to proteins, poses a significant barrier towards developing a theoretical model that generally applies to all proteins. Faced with this apparent disconnect between protein structure and function, much effort has instead concentrated on developing methods to characterize allosteric mechanisms in individual proteins. These methods often focus on quantifying the dynamic and structural conformational changes undergone by allosteric proteins or identifying pathways of residues responsible for communicating allosteric signals [59, 14]. The guiding hope behind this approach is that understanding the allosteric mechanisms of enough individual proteins will help to identify generic motifs, eventually providing enough insight to develop a unified conceptual description.

Over the last few decades, a common perspective has arisen that allostery is a property of a protein's underlying network of interactions. In many of the approaches that have been developed to characterize allostery, a protein is approximated as a mechanical (or elastic) network, with edges (bonds) representing interactions between amino acids [35]. When a localized source is applied at one site, the signal is mediated by the network to induce a specific localized response at a second distant site. Although this phenomenon has historically been discussed in the context of proteins, allostery has also been more broadly framed as a property of any molecular system composed of a network of interactions [14]. Here we propose an even more inclusive definition of allostery: it is not just a property of molecules, but rather a property of complex *networks* in general. Given this broader definition, many other types of naturally occurring and synthetic networks could potentially exhibit allostery-like behaviors.

In particular, venation networks in animals [77], plants [55, 66], fungi [33], and slime molds [74] present an interesting example, as they are often composed of complex hierarchical network structures that are optimized to direct flow from a limited number of inputs to support local activity or growth throughout the system. While much effort has been devoted to understanding the design and optimization of general transport networks [1], the problem of fuctional control in flow networks has never been framed in the context of allostery. This is in spite of the close mathematical relationship between mechanical and flow networks; in the linear regime, flow (or resistor) networks can be mapped onto one-dimensional linear spring networks [73]. This correspondence provides an alternative framework within which to study allostery, as flow networks are less mathematically complex (having less degrees of freedom per node), but still share many of the qualitative behaviors of their higher-dimensional counterparts. Experimental studies of biological flow networks suffer from some of the same obstacles encountered when studying proteins. This is especially apparent in systems such as the brain vasculature where significant variation in micro-scale architectures can exist between individuals [32], although brains from individuals within the same species (or even between different species) are ostensibly able to redistribute blood in the same ways. Understanding how this variation does or does not affect function is difficult as experiments are limited to sampling network architectures from relatively small numbers of – or even single – individuals [13].

One of the most interesting properties shared by both proteins and venation networks is the ability to regulate and change their allosteric functionality. In proteins, this

occurs over many generations via the accumulation of genetic mutations, modifying a protein's constituent amino acids and consequently its network of interactions. If these changes cause the protein to develop some beneficial allosteric functionality, then the corresponding genes may experience positive selection. On the other hand, many venation networks can actively redirect flow as dictated by the needs of the system. For example, the cerebral vasculature can dynamically contract and dilate blood vessels, enabling the brain to actively control the propagation of blood to support local neuronal activity [29, 26]. More generally, the ability to locally tune the conductances of individual vessels in venation networks enable animals, fungi, and slime molds to control the spatial distribution of water, nutrients, oxygen, or metabolic byproducts.

Taking inspiration from the ability of both proteins and venation networks to modulate functionality, this dissertation follows an alternative route towards developing an understanding of allostery. We approach allostery from the perspective of metamaterials design, developing techniques to create synthetic allosteric networks in both flow and mechanical systems. In mechanical networks, we define allostery in terms of the elastic response to applied strains, while in flow networks we consider the redistribution of pressures upon the application of external pressure sources. In both cases, an allosteric function is one in which a specific target site responds in a predetermined way when a source is applied at a predetermined site elsewhere in the network.

Not only does designing synthetic allosteric systems allow us to determine the ingredients necessary for allostery to exist, but also allows us to generate large ensembles

of such networks. By using these ensembles, we are better able to investigate the types of allosteric function that are possible and simultaneously reveal the seemingly complex relationship between structuture and function. We can also investigate to what extent allosteric mechanisms are optimal and the trade-offs between this optimality and adaptability. By efficiently creating synthetic allosteric networks, we can also better study the statistical variation in the network architectures of such systems without the constraints imposed by limited experimental data. The inclusion of flow networks in our studies helps to generalize our results, providing a system which is often simpler to understand while still giving us insight in mechanical systems.

This thesis contains content that is primarily reproduced in order from Refs. [61], [62], and [63]. Chapter 2 starts by presenting methods to create synthetic allosteric mechanical networks in both theory and experiment. We find that creating allosteric functionality is remarkably easy; by simply removing a small percentage of the bonds in a spring network, almost any initial network can be tuned to exhibit allosteric behavior. This shows that the requirements of allostery are minimal, simply necessitating a network to have enough tunable degrees of freedom. Next, Chapter 3 extends the tuning method to include flow networks. Using this combined framework, we show that the limits of multifunctionality in both systems are set by the same constraint satisfaction phase transition. This provides strong evidence that the problems of controlling allosteric behavior in flow and mechanical networks belong to the same class. Chapter 4 uses topological data analysis to identify the structural means by which allosteric functionality is created in flow networks. We find that

the relationship between structure and function is topological in nature, providing a universal characterization that applies to all tuned allosteric flow networks.

An additional supplemental chapter is provided at the end of the thesis, reproducing content from Ref. [6]. This chapter contains work to which I contributed significantly at the beginning of my doctoral studies, but does not fit as cleanly into the narrative of this dissertation outlined above. In this work, we developed a model of the embryonic chicken heart as a mechanically active medium. When the heart beats, cardiac muscle cells contract in a coordinated fashion, generating a nonlinear contractile wavefront that propagates across the heart. Traditional models of this behavior assume this wavefront is coordinated via electrical signaling between cells. However, recent experiments revealed that the velocity of this wavefront can depend on the mechanical properties of the cardiac tissue, behavior that cannot be explained by standard electrochemical signaling. To remedy this, we proposed a mechanical signaling mechanism in which cells contract in response to strains exerted by their neighbors. Our prediction that the embryonic heart would continue to beat even in the absence of electrical signaling was confirmed experimentally using gap junction blocking drugs. This result demonstrated that the embryonic heart does indeed use mechanical signaling to coordinate the heartbeat. While this work is not specifically concerned with allostery in biological networks, it still adheres to the theme of long-range signaling in complex biological systems. By utilizing a mechanical signaling mechanism, the embryonic heart is able to robustly propagate mechanical strains generated by a small collection of cells in a localized area throughout the entire organ.

If one desired, this long-range signaling behavior could be interpreted as a dynamic form of allostery, further demonstrating that developing a general understanding of allosteric mechanisms could give insight into a very broad range of biological systems.

Chapter 2

Designing allotery-inspired response in mechanical networks

Note: The following content is reproduced with minor revision from Ref. [61].

2.1 Introduction

The ability to tune the response of mechanical networks has significant applications for designing meta-materials with unique properties. For example, the ratio G/B of the shear modulus G to the bulk modulus B can be tuned by over 16 orders of magnitude by removing only 2% of the bonds in an ideal spring network [28]. Such a pruning procedure allows one to create a network that has a Poisson ratio ν anywhere between the auxetic limit ($\nu = -1$) and the incompressible limit ($\nu = 1/(d-1)$ in d dimensions). In another example, the average coordination number of

a network controls the width of a failure zone under compression or extension [15]. Both these results are specific to tuning the global responses of a material. However, many applications rely on targeting a local response to a local perturbation applied some distance away. For example, allostery in a protein is the process by which a molecule binding locally to one site affects the activity at a second distant site [59]. Often this process involves the coupling of conformational changes between the two sites [11]. Here we ask whether disordered networks, which generically do not exhibit this behavior, can be tuned to develop a specific allostery-inspired structural response by pruning bonds.

We introduce a formalism for calculating how each bond contributes to the mechanical response anywhere in the network to an arbitrary applied source strain. This allows us to develop algorithms to control how the strain between an arbitrarily chosen pair of target nodes responds to the strain applied between an arbitrary pair of source nodes. In the simplest case, bonds are removed sequentially until the desired target strain is reached. For almost all of the initial networks studied, only a small fraction of the bonds need to be removed in order to achieve success. As was the case in tuning the bulk and shear moduli, we can achieve the desired response in a number of ways by pruning different bonds. We have extended our approach to manipulate multiple targets simultaneously from a single source, as well as to create independent responses to different locally applied strains in the same network. Our central result is the ease and precision with which allostery-inspired conformational responses can be created with only minimal changes to the network structure.

We demonstrate the success of this method by reproducing our theoretical networks in macroscopic physical systems constructed in two dimensions by laser cutting a planar sheet and in three dimensions by using 3D printing technology. Thus, we have created a new class of mechanical meta-materials with specific allostery-inspired functions.

2.2 Theoretical Approach

Our networks are generated from random configurations of soft spheres in three dimensions or discs in two dimensions with periodic boundary conditions that have been brought to a local energy minimum using standard jamming algorithms [51, 43]; the spheres overlap and are in mechanical equilibrium. We convert a jammed packing into a spring network by joining the centers of each pair of overlapping particles with an unstretched central-force spring. We chose this ensemble because it is disordered and provides initial networks with properties – such as elastic moduli – that depend on the coordination of the network in ways that are understood [19, 20, 28]. We can work either with the entire system that is periodically continued in space or with a finite region with free boundaries that is cut from the initial network.

Starting with a network with N nodes and N_b bonds in d dimensions, our aim is to tune the strain ε_T between a pair of target nodes in response to the strain ε_S applied between two source nodes. (The two nodes comprising each of the target or source are

chosen so that they are not initially connected by a bond; see Appendix). We create a specific response in our system by tuning the strain ratio $\eta = \varepsilon_T/\varepsilon_S$ to a desired value η^*. At each step, we calculate to linear order the change in η in response to the removal of each bond in the network using a computationally-efficient linear algebra approach (see Methods). We then remove the bond which minimizes the difference between η and η^* and repeat until we reach a desired tolerance.

2.3 Computational Results

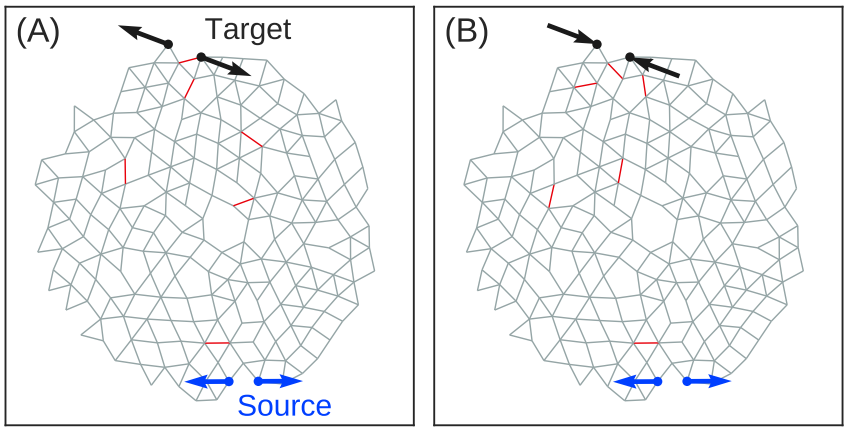

Figure 2.1: Network with 194 nodes, 407 bonds at $\Delta Z = 0.19$ tuned to exhibit (A) expanding ($\eta = +1$) and (B) contracting ($\eta = -1$) responses to within 1% of the desired response. Source nodes are shown in blue, while target nodes are shown in black. Arrows indicate the sign and magnitude of the extension between the pairs of source and target nodes. The removed bonds are shown as red lines.

We apply our tuning approach to networks with free boundaries in both two and three dimensions (see Methods). We characterize the connectivity of our networks by the excess coordination number $\Delta Z \equiv Z - Z_{\text{iso}}$. Here Z is the average number of bonds per node and $Z_{\text{iso}} \equiv 2d - d(d+1)/N$ is the minimum number of bonds needed

for rigidity in a network with free boundary conditions [27]. For each trial, a pair of source nodes was chosen randomly on the network's surface, along with a pair of target nodes located on the surface at the opposing pole. (Note that we could have chosen anywhere in the network for the location of the source and target.) In two dimensions we chose networks that on average had 190 nodes and 400 bonds before tuning, with $\Delta Z \approx 0.19$. In three dimensions networks had on average 240 nodes, 740 bonds and $\Delta Z \approx 0.18$. Prior to pruning, the average strain ratio of the networks in two dimensions was $\eta \approx 0.03$ and in three dimensions was $\eta \approx 0.2$ for the system sizes and ΔZ values we studied. The response of each network was tuned by sequentially removing bonds until the difference between the actual and desired strain ratios, η and η^* respectively, was less than 1%.

To demonstrate the ability of our approach to tune the response, we show results for $\eta = \pm 1$. Note that $\eta > 0$ (< 0) corresponds to a larger (smaller) separation between the target nodes when the source nodes are pulled apart. Fig. 2.1 shows a typical result for a two-dimensional network: in Fig. 2.1(A), the strain ratio has been tuned to $\eta = +1$ with just 6 (out of 407) bonds removed; Fig. 2.1(B) shows the same network tuned to $\eta = -1$ with a different set of 6 removed bonds. The red lines in each figure indicate the bonds that were pruned. Animations of the full nonlinear responses of these networks are provided in Videos 2.8 and 2.9 of the Appendix. We note that some of the removed bonds are the same for both $\eta = +1$ and $\eta = -1$.

The average strain ratio versus the number of removed bonds is shown in Fig. 2.2(A). Remarkably few bonds need to be removed in order to achieve strain ratios of $\eta = \pm 1$.

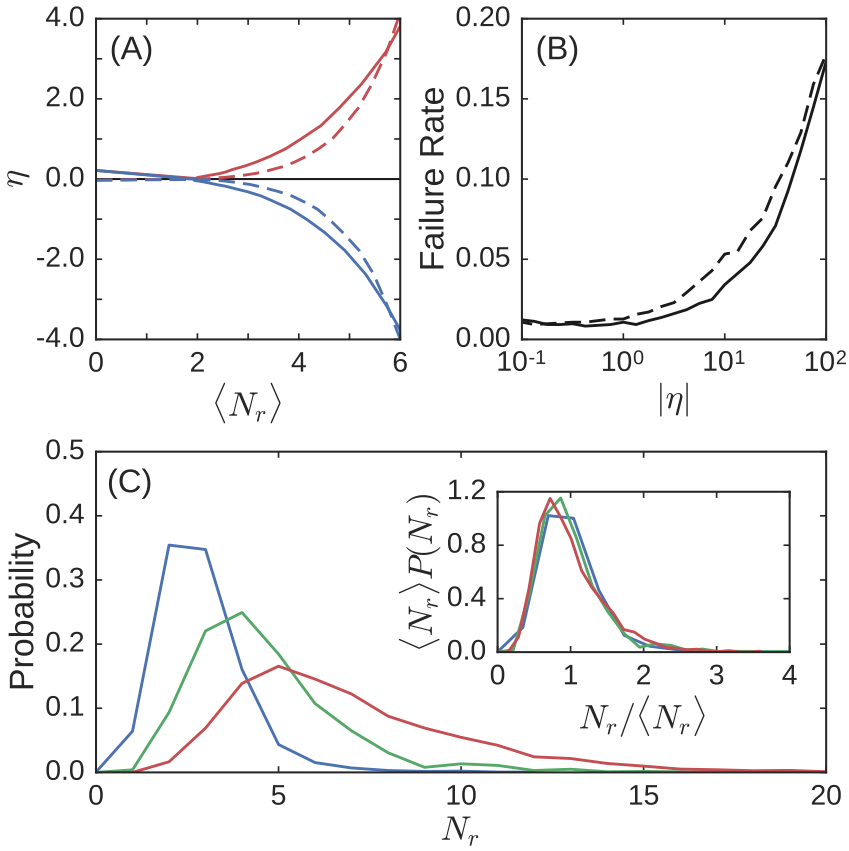

Figure 2.2: (A) Strain ratio η versus the number of removed bonds N_r for expanding (red) and contracting (blue) responses in both 2D (solid lines) and 3D (dashed lines). For each response type and dimension, the strain ratio is averaged over 1024 tuned networks constructed from 512 initial systems. Networks in 2D have about 190 nodes and 400 bonds on average with an initial excess bond coordination of $\Delta Z \approx 0.19$, while those in 3D have about 240 nodes and 740 bonds on average with $\Delta Z \approx 0.18$. (B) Failure rate of tuning systems to within 1% of a specified strain ratio magnitude in 2D (dashed lines) and 3D (solid lines) averaged over contracting and expanding responses. (C) The distribution of the number of removed bonds for three different strain ratio magnitudes: $|\eta| = 0.1$ (blue), $|\eta| = 1.0$ (green), and $|\eta| = 10.0$ (red). Inset: All three distributions collapse when scaled by the average number of removed bonds $\langle N_r \rangle$.

In two dimensions only about 5 bonds out of about 400 were removed on average (∼1%); similarly, in three dimensions only about 4 bonds out of about 740 were removed on average (∼0.5%). Fig. 2.2(B) shows the fraction of networks that cannot be tuned successfully to within 1% of a given strain ratio. The failure rate is less

than 2% for strain ratios of up to $|\eta| = 1$ in two dimensions and less than 1% in three dimensions. Therefore, not only does our algorithm allow for precise control of the response, it also works the vast majority of the time. The failure rate increases significantly for $|\eta| \gg 1$, but here we are considering only the linear response of the network. Extremely large values of η necessitate an extremely small input strain at the source and may therefore not be physically relevant.

The failure rate is insensitive to ΔZ except at very small values. In the small ΔZ regime the failure rate is higher because very few bonds can be removed without compromising the rigidity of the system. If we increase the bond connectivity to $\Delta Z \approx 1.0$ for networks in two dimensions, the failure rate remains very low, but bonds are removed in a thin region connecting the target and source. This narrowing of the "damage" region is reminiscent of the results of Ref. [15], in which bonds above a threshold stress were broken, or of Ref. [28], in which bonds that contribute the most to either the bulk or shear modulus were successively pruned.

Fig. 2.2(C) shows the distribution of the number of bonds that must be removed to tune a network to within 1% of a desired strain ratio for $|\eta| = 0.1$, 1, and 10. These distributions are broad and the mean shifts upwards as η increases. The inset shows that the distributions collapse when normalized by the average number of removed bonds $\langle N_r \rangle$. Note that we do not achieve the desired strain ratio simply by tuning the entire free surface of the network to have large strain ratios; the response of the designated target is large while the response between other pairs of nodes is essentially unaffected by the source strain (see Fig. 2.12 in the Appendix).

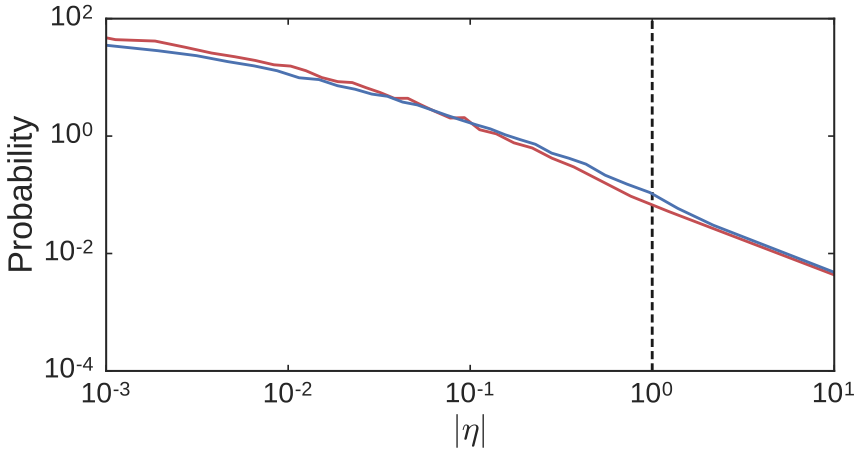

Figure 2.3: Distribution of strain ratios for pairs of neighboring nodes on the surface (excluding the source and target pairs) of the networks before (red) and after (blue) tuning. Results are shown for 2D networks that had on average 190 nodes and 400 bonds with $\Delta Z \approx 0.19$. This includes 512 initial networks each tuned separately to a positive and negative strain ratio with magnitude $|\eta| = 1.0$ for a total of 1024 tuned networks. Tuned networks are only included if the tuned strain ratio is within 1% of the desired strain ratio. The response for pairs other than the source and target are essentially unaffected. The target strain ratio is shown with a vertical dashed line. All distributions include both contracting and expanding responses.

Fig. 2.4 demonstrates the variety of responses that we are able to create. Fig. 2.4 3(A-I) and (A-II) show a single network with two independent sources and targets whose responses were tuned simultaneously and independently of one another. When a strain is applied to the first pair of source nodes, its target responds strongly while the other target does not respond at all. Likewise, when the strain is applied to the second pair of source nodes, its target responds while the first target does not. In Fig. 2.4(B), a network with one pair of source nodes controls three targets, each of which has been tuned to a different strain ratio. These networks have $\Delta Z = 1.0$; the failure rate for creating these more complicated responses is generally higher for lower values of ΔZ in two dimensions. Fig. 2.4(C) shows a periodic disordered network with one source and target, demonstrating that a network can be tuned successfully

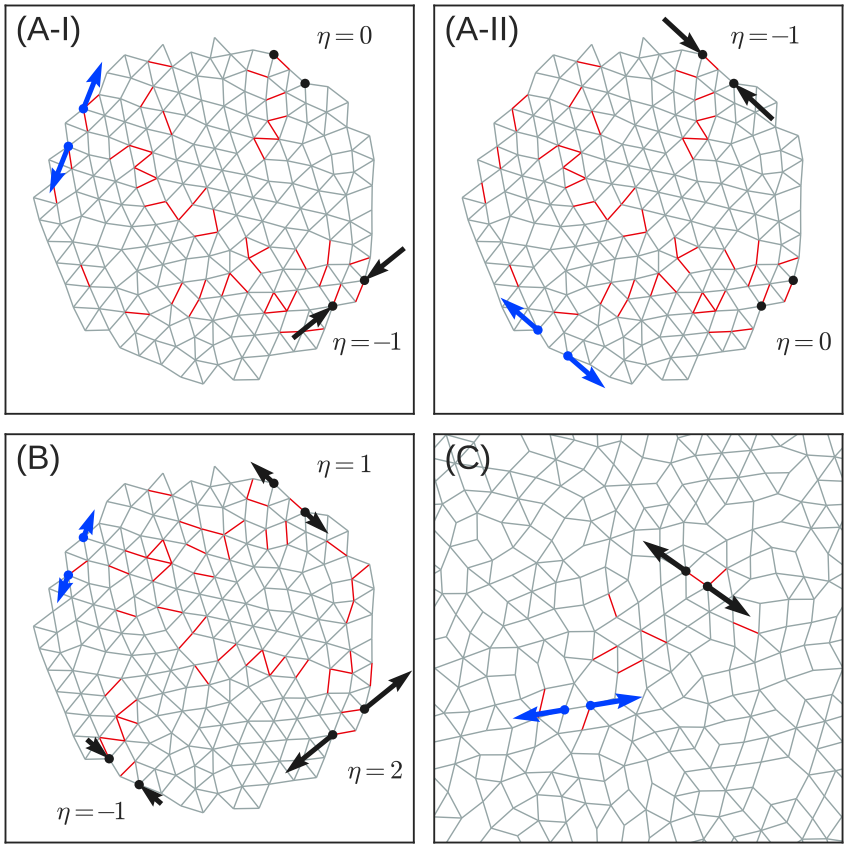

Figure 2.4: (A) Network with 200 nodes and 502 bonds at $\Delta Z = 1.0$ with two independent responses tuned simultaneously into the system. (A-I) One target contracts in response to a strain at the first pair of source nodes while the other target does not respond. (A-II) Second target responds to a strain at the second source while the first target remains unaffected. This demonstrates that separate responses can be shielded effectively from one another. (B) Same network tuned to show responses at three targets with responses of $\eta = 1$, 2, and -1. All three targets are controlled by a single pair of source nodes. (C) Periodic network with 254 nodes and 568 bonds at $\Delta Z = 0.47$ tuned to display an expanding response with $\eta = 1$, showing that open boundaries are not necessary for tuning to be successful.

without free boundaries (see Video 2.10 in the Appendix for an animation of the nonlinear response). We have also found that initial disorder in the network is not necessary for success (Fig. 2.5(A)), nor is close proximity of the two nodes comprising the source or the target (Fig. 2.5(B)).

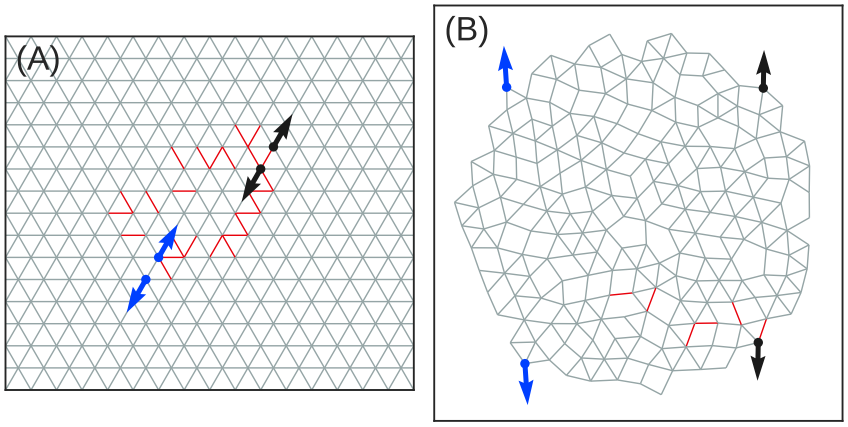

Figure 2.5: (A) Periodic triangular lattice with 256 nodes and 768 bonds at $\Delta Z = 2.0$ tuned to exhibit a strain ratio of $\eta = 1.0$. This example shows that disorder in the initial network is not necessary for a response to be tuned successfully. (B) Network with 200 nodes and 457 bonds with $\Delta Z = 0.57$ tuned to show a strain ratio of $\eta = 1.0$. This demonstrates that the proximity of the source nodes to each other, and similarly the target nodes, is also not necessary for success.

2.4 Experimental Results

Fig. 2.5(A) shows an image of a two-dimensional network created by laser cutting a flat sheet. The network is the same as the simulation shown in Fig. 2.1(A). The zoomed-in areas show the strain response at the target along with the applied strain at the source nodes. Video 2.11 of the Appendix shows the response of a similarly designed network. Fig. 2.6(B) shows an image of a three-dimensional network created by 3D printing. In this case, the network was designed to have a strain ratio of $\eta = -5$. The insets again show the relative strains between the pairs of target and source nodes.

In order to obtain a quantitative analysis of how well the physical realizations agree with the simulated networks, we measure the strain on every bond in the two-dimensional example when the distance between the source nodes is varied. A major-

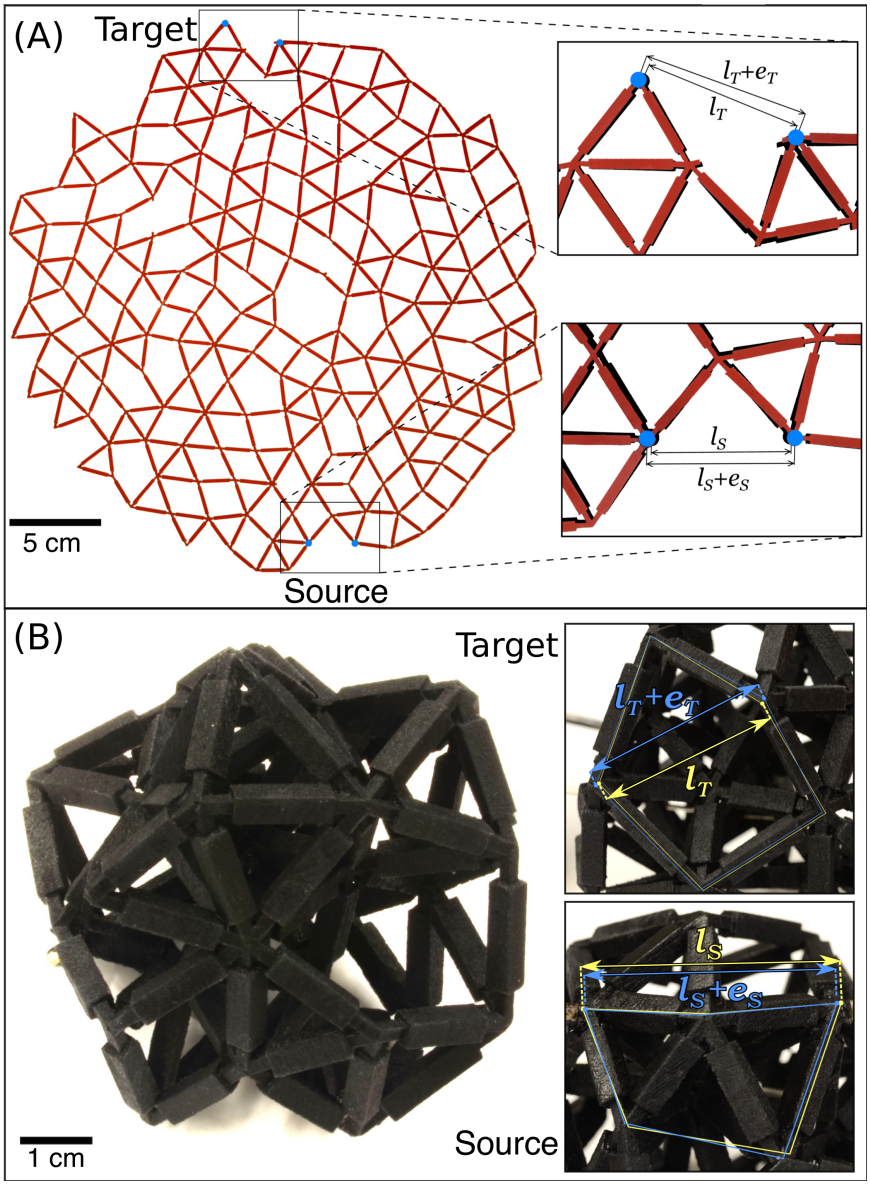

Figure 2.6: (A) Physical realization of the network in Fig. 2.1(A). The zoomed-in photographs show the initial and final distance between the pair of source nodes, l_S and $l_S + e_S$, respectively, and between the pair of target nodes, l_T and $l_T + e_T$. The undeformed network is shown in black, while the deformed network is superimposed in red. (B) Photograph of a three-dimensional network constructed by 3D printing with 33 nodes and 106 bonds at $\Delta Z = 0.42$ tuned to exhibit a negative response ($\eta = -5.0$). In the zoomed-in photographs, the yellow and blue arrows show the distance between the undeformed, l_S (l_T), and deformed, $l_S + e_S$ ($l_T + e_T$), source (target) nodes, respectively.

ity of the bonds do not change their length appreciably. We therefore focus only on the distance between nodes that were connected by bonds that were removed as the

network was tuned. As one might expect, these are the most sensitive to the applied source strain. We calculate, for those changes in distances, the Pearson correlation coefficient between the experiments and the simulations:

$$C = \frac{\langle (x_i - \langle x_i \rangle)(c_i - \langle c_i \rangle) \rangle}{\sigma_x \sigma_c} \tag{2.4.1}$$

Here x_i (c_i) is defined as the fractional change due to the source strain in the distance between nodes initially connected by bond i as measured in experiments (computer simulations). The standard deviations of x_i and c_i are σ_x and σ_c, respectively. We find that when averaged over 4 experimental realizations of different designed networks, $C = 0.98 \pm 0.02$. This indicates that the experiments are very accurate realizations of the theoretical models.

In contrast to our simulations, where junctions are connected only via central-force springs, our experimental systems have physical struts between the nodes. This introduces bond-bending forces because the struts emerging from a node have preferred angles between them. In order to minimize such forces, we have manufactured the struts with a non-uniform width so that they are thinner at their ends where they attach to a node than along the rest of their length. This ensures that the struts deform preferentially near the nodes rather than buckling in their middle. Figure 5 shows that decreasing the width of the thinnest part of the struts alleviates effects due to bond-bending and monotonically increases the response. This is crucial for determining how much of the designed response survives in our physical networks.

Apart from bond-bending, there is also a possibility of two-dimensional networks buckling out of the plane, along with nonlinear effects that are present in real systems undergoing finite strains. All these factors can weaken the designed response. To investigate these effects, we used laser cutting to create realizations of 10 of the two-dimensional networks produced from the computations in Fig. 2.2. The networks chosen were tuned successfully in the linear regime and had nonlinear responses within a factor of two of the linear prediction at a source strain of 5%, according to our computations. For the experimental realizations, we found that in the nonlinear regime, 3 of the networks demonstrated a response that was more than 10% of the designed response at a source strain of 5%.

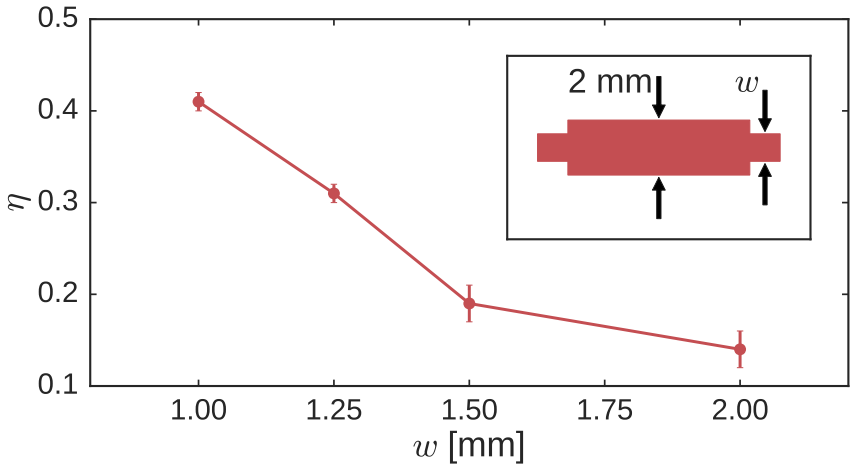

Figure 2.7: Strain ratio η versus w, the width of the struts near their ends. These are responses of the network shown in Fig. 2.1(A) for 4 values of w. The response increases monotonically as the bonds are made thinner near the nodes. At their center, the struts have a full width of 2 mm. Inset shows the strut geometry.

2.5 Discussion

We have shown that it is strikingly easy to tune allosteric deformation responses into an arbitrary spring network by removing only a small fraction of the bonds. Not only can we tune the strain ratio to large negative or positive values for the same network, but we achieve strain ratios of order $|\eta| \sim 1$ with almost 100% success. Our theoretical approach can also be extended to more general responses. We can control multiple pairs of target nodes simultaneously with the same pair of source nodes and we can tune multiple independent source/target responses simultaneously into a network. We have also achieved similarly excellent results for tuning responses in periodically-continued systems.

The approach we have described here performs a discrete optimization of the response. We have also tuned the response using a standard numerical optimization technique (e.g., gradient descent), by varying the stiffnesses of all the bonds continuously. This brute-force method is less efficient but equally successful in producing a desired response, and has the advantage of being able to tune nonlinear behavior. Our approach can also be generalized to other types of bond manipulation such as introducing new bonds.

Our theoretical approach provides a framework for understanding and controlling the response of networks relevant to a wide range of fields. For example, networks with built-in localized, long-distance responses could be a novel way of designing architectural structures based on disordered frameworks that have added functionalities.

In addition, our theoretical approach can be generalized to other problems such as origami, where one may wish to tune the fold structure so that the system folds in a specific way in response to locally applied external forces [24]. This problem is similar to ours, except that folds are added instead of bonds being removed. Ref. [24] introduces an optimization technique in which fold rigidities vary continuously. This technique is computationally expensive because the network response must be recalculated with each optimization step. A generalization of our theoretical approach to origami, using language similar to that of Ref. [67], could lead to a more efficient algorithm.

The network responses we create are reminiscent of the localized, long-range-correlated deformations which characterize allostery in proteins. In fact, folded proteins have long been modeled as elastic networks [35] and the response to localized forces in the resulting networks has been studied [2]. Our results demonstrate the ease with which allosteric conformational changes in networks can be achieved by removing a very small set of bonds. As such, it suggests why allostery is so common in large biological molecules [31].

Similarly, our finding that networks can be tuned to have a variety of different responses may help elucidate multifunctional behavior [49] and multiple allosterically interacting sites [84] in proteins. It has also been observed that small changes in a protein's covalent structure can often change its biochemical function [37]. One might ask whether our method could be extended to develop a systematic way to determine which intra-protein interactions to modify or create new allosteric functions. It has

been emphasized that the ability to control allosteric responses in folded proteins could lead to significant advances in drug design [50, 30]. While much work has focused on identifying, understanding and controlling pre-existing allosteric properties, the question of how to introduce new allosteric functions is relatively unexplored [14].

Our success in constructing experimental systems in spite of nonlinear and bond-bending effects suggests that results are often robust even outside the simple linear regime. However, proteins are thermal whereas our networks are athermal structures. Statistical fluctuations in the structure of proteins has been shown to play an important role in allosteric functionality [76, 47]. In the linear response regime, the equilibrium response at finite temperature is equivalent to that at zero-temperature, so the set of bonds that are removed and the average strain ratio are independent of temperature in the harmonic regime. However, the nonlinear response will show differences, particularly at temperatures beyond the harmonic regime. It is thus important to investigate how thermal effects can influence the ability to design a desired response in the nonlinear regime. In addition, protein contact networks generally contain pre-stressed bonds, as well as bond-bending and twisting constraints, while our theoretical networks are constructed in the absence of such effects [18, 75, 71].

Further work needs to be done to understand why removing specific bonds achieves the desired response. Our method of identifying the elements of the stress basis associated with individual bonds indicates that these stress states are fundamental to this understanding. The dependence on network size and node connectivity also needs to be understood in greater detail. The limits of our algorithm are not yet known,

including the number of targets that can be controlled and the number of independent responses that can be tuned for networks of a given size and coordination. To understand experimental systems ranging from proteins to the macroscopic networks we have fabricated, we must extend the theory to include temperature, dynamics, pre-stress, bond-bending, and nonlinear effects due to finite strains. Our approach provides a starting point for addressing these issues.

2.6 Materials and Methods

2.6.1 Computed Networks and Choice of Source and Target Nodes

To create a finite network, we choose a cut-off radius from the center of our box and remove all bonds that cross that surface. This process often creates zero energy modes at the boundary of our network. Since we require rigid networks, we remove nodes associated with these modes. We calculate zero modes by performing a spectral decomposition of the dynamical matrix. For each zero mode calculated this way, we identify the node with the largest displacement amplitude and remove it. We then recalculate the zero modes and repeat this process until no zero modes exist. This method of removing zero modes works in any dimension and does not require an arbitrary threshold for whether a node contributes to a zero mode or not. Our final networks are approximately disc-shaped in two dimensions or ball-shaped in three

dimensions with N nodes and N_b bonds.

We choose the pair of source nodes to lie on the exposed surface of the networks. The pair of target nodes is chosen to be on the opposing pole of the network surface. When choosing a pair of nodes, we also ensure that they are not connected by a bond. This is done to avoid surface bonds whose tensions do not couple the the rest of the network. However, since our formalism relies on applying tensions and measuring the strains of bonds, we introduce a bond of zero stiffness, called a "ghost" bond, between each pair of nodes for convenience (see Appendix).

2.6.2 Further Details of Theoretical Approach

Our approach tunes the ratio $\eta = \varepsilon_T/\varepsilon_S$ of the target strain ε_T to the source strain ε_S by removing bonds sequentially, one at a time. First, we define the cost function which measures the difference between the network's response η and the desired response η^*. This is given by

$$\Delta^2 \equiv \sum_{j=1}^{n} \begin{cases} (\eta_j/\eta_j^* - 1)^2 & \text{if} \quad \eta_j^* \neq 0 \\ \eta_j^2 & \text{if} \quad \eta_j^* = 0 \end{cases} \tag{2.6.1}$$

where j indexes the targets and their corresponding sources (e.g., $n = 1, 2, 3$ in Fig. 2.1, Fig. 2.4(A) and Fig. reffig:examples(B), respectively). Target/source pairs may be defined for the same network response, or for separate independent responses for the same network with different applied source strains. With each step, we choose

to remove the bond which creates the largest decrease in Δ^2.

To decide which bond to remove, we must calculate how the removal of each bond changes η. First we define the vectors of bond extensions $|e\rangle$ and bond tensions $|t\rangle$ in response to the externally applied strain, each of length N_b. In order to access the extensions and tensions on individual bonds, we define the complete orthonormal bond basis $|i\rangle$ where i indexes the bonds. The extension on bond i can then be found, $e_i = \langle i|e\rangle$, along with the bond tension, $t_i = \langle i|t\rangle$. The strain of bond i is $\varepsilon_i = e_i/l_i$ where l_i is the bond's equilibrium length. The tension and extension are related by a form of Hooke's law,

$$|t\rangle = F^{-1}\,|e\rangle \tag{2.6.2}$$

where the flexibility matrix is defined as $\langle i|F|j\rangle = \delta_{ij}/k_i$. Here we choose the stiffness of bond i to be $k_i = \lambda_i/l_i$ where λ_i is the bond's material modulus with units of energy per unit length.

In addition to the bond tensions and extensions, we can define the dN-vectors of node displacements $|u\rangle$ and net forces on nodes $|f\rangle$. The equilibrium matrix Q relates quantities defined on the bonds to those defined on the nodes through the expressions $Q^T\,|u\rangle = |e\rangle$ and $Q\,|t\rangle = |f\rangle$ [7]. In general Q, is a rectangular matrix with dN rows and N_b columns. The total energy can then be written

$$E = \frac{1}{2}\,\langle u|H|u\rangle \tag{2.6.3}$$

where the Hessian matrix $H = QF^{-1}Q^T$ is a $dN \times dN$ matrix. In the presence of an externally applied set of tensions $|t^*\rangle$, the minimum energy configuration satisfies

$$H\,|u\rangle = Q\,|t^*\rangle\,. \tag{2.6.4}$$

To calculate the change in the displacements if a bond were removed, the naive approach would be to set the stiffness to zero for that bond in the flexibility matrix and to solve this equation. However, performing this matrix inversion to test the removal of each bond can be prohibitively expensive with a computational cost of $\mathcal{O}(N_b N^3)$, so we have developed a more efficient approach. Note that here we calculate the response to applied tensions, not the strains we need to calculate η. However, since we are only interested in the ratio of the target strain to the source strain and are working in the linear regime, we do not need to explicitly apply a strain nor specify the tension amplitude.

We use the equilibrium matrix Q to define a convenient basis of the bond tensions and extensions. Performing a singular value decomposition of Q gives access to is right singular vectors [54]. This yields two mutually orthonormal sub-bases of vectors that together form a complete basis of size N_b. The first sub-basis is comprised of vectors with singular values of Q that are zero; that is, tensions that do not result in net forces on the nodes. These are commonly known as the *states of self-stress* (SSS), and we denote them as $|s_\beta\rangle$ where β indicates the particular basis vector. These vectors can also be interpreted as incompatible extensions, or extensions that do not

correspond to valid displacements. The second sub-basis is comprised of vectors with positive singular values of Q; tensions that correspond to net forces on nodes, or extensions that are compatible with node displacement. We call these vectors the *states of compatible stress* (SCS) and denote them as $|c_\alpha\rangle$ where α indicates the basis vector. In total there are N_c SCS basis vectors and N_s SSS basis vectors which total to $N_c + N_s = N_b$.

Using these two sub-bases (and rescaling the bond stiffnesses so they are identicall k; see Appendix), we can calculate the discrete Green's function

$$G = \frac{1}{k} \sum_{\alpha} |c_\alpha\rangle \, \langle c_\alpha| \tag{2.6.5}$$

which maps bond tensions to extensions. Using this result, we calculate the change in the bond extension vector $|e\rangle$ if bond i were to be removed,

$$|\Delta e\rangle = |C_i\rangle \, \frac{\langle C_i | t^* \rangle}{k(1 - C_i^2)} \tag{2.6.6}$$

where $|C_i\rangle = kG\,|i\rangle$ and $C_i^2 \equiv \langle C_i | C_i \rangle$. From this equation we can calculate the changes in both ε_T and ε_S and therefore the change η. This result can also be derived by inverting (2.6.4) and using the Sherman-Morrison formula to calculate the change in the inverse of the Hessian [70]. Note that this calculation does not include the zero stiffnesses of the ghost bonds, which cannot be mapped to unity with the rest of the system. A generalization of (2.6.6) is needed in order to take this into account (see Appendix).

The next step is to calculate (2.6.6) (or its generalization found in the Appendix) for the removal of each bond. We choose the bond which minimizes Δ^2 in (2.6.1) upon removal. One restriction is that we do not choose bonds which introduce zero modes (see Appendix). Finally, once a bond is chosen, we recalculate the SCS and SSS sub-bases with the bond removed (see Appendix).

A summary of our tuning algorithm contains the following steps:

1. Transform to a system where all bonds initially have the same stiffnesses and add a ghost bond of zero stiffness for each pair of target and source nodes (see Appendix).

2. Use the equilibrium matrix to calculate the initial SCS and SSS bases.

3. Calculate the initial extensions of the source and target bonds in response to the applied tension t^* using (2.6.5). Use this result to calculate the initial η.

4. For each bond, use the general form of (2.6.6) found in Eq. 2.7.15 of the Appendix to calculate the change in η if that bond were to be removed.

5. Remove the bond that minimizes Δ^2 in (2.6.1). Recalculate the SCS and SSS sub-bases with the bond removed.

We repeat steps (3) - (5) until $\sqrt{\Delta^2} < 0.01$ or the process fails. The computational cost of determining and removing a bond using this algorithm is dominated by step (5) with a complexity of $\mathcal{O}(N_b^3)$; much faster than the naive approach of directly solving (2.6.4) with a complexity of $\mathcal{O}(N_b N^3)$.

There are three potential sources of failure represented in Fig. 2(B): $\sqrt{\Delta^2}$ cannot be lowered below 0.01 by removing any bond, no bonds can be removed without creating zero modes, or the numerical error in Δ^2 exceeds 0.01. This third source of failure arises because numerical error is introduced as bonds are removed. In order to ensure that our results are accurate, we compare Δ^2 to the value obtained from the solution of (2.6.4) with the given set of pruned bonds removed. If the absolute value of the difference exceeds 1%, we call it a failure. Our results constitute an upper bound on the failure rate, which could potentially be reduced by using more accurate techniques to decrease numerical error or more sophisticated minimization algorithms.

2.6.3 Experimental Networks

We create experimental realizations of the theoretically-designed networks in both two and three dimensions. To make two-dimensional networks, we obtain the positions of the nodes and struts from our design algorithm. Next, we laser cut the shape of the network from a silicone rubber sheet. To reduce out-of-plane buckling, we use 1.6 mm thick polysiloxane sheets with a Shore value of A90. The ratio of strut length to width within the plane of the network is approximately 10:1. The struts are designed to be thinner at their ends in order to alleviate bond-bending.

To make three-dimensional networks, we determine the positions of nodes and struts from the computer simulations and fabricate the networks using 3D printing technology. The proprietary material is a mixture of rubber (simulating styrene based ther-

moplastic elastomers) and rigid plastic (simulating acrylonitrile butadiene styrene, ABS) with a Shore value of A85. The dimensions of each strut have a ratio of approximately 1:1:11. As in our two-dimensional networks, the struts are made thinner at their ends.

2.7 Appendix

2.7.1 Ghost bonds

On the surface of our networks there are many nodes with exactly d bonds in d dimensions. Any bond attached to one of these nodes is uncoupled from the rest of the network - applying a tension to one of these bonds does not affect any tensions or extensions on any of the other bonds in the network to linear order. Likewise, no extensions can be measured on these bonds when a tension is applied elsewhere in the network. Therefore, we avoid choosing pairs of source or target nodes that are connected by uncoupled bonds. This is done by ensuring that neither the pair of nodes comprising the source nor the target share a bond.

However, all calculations involve the bonds, so in order to apply a tension or measure an extension between two nodes, it is convenient if they share a bond. To apply our approach, we introduce a "ghost" bond of zero stiffness between each pair of source or target nodes. These bonds do not affect our results, but allow us to work without

any direct reference to the nodes.

2.7.2 Creating identical bond stiffnesses

In order to calculate the Green's function in Eq. 2.6.5 in the main text, it is necessary to work in a system where all bonds have identical stiffness. However, we do not want to be restricted to systems that satisfy this special requirement. The bonds in our experimental systems all have the same material modulus $\lambda_i = \lambda$, but their equilibrium lengths l_i differ, resulting in bonds with non-identical stiffnesses $k_i = \lambda/l_i$. To handle this, we start with a system in which the bond stiffnesses are all different and map it onto an equivalent system in which all the default bond stiffnesses are identical. This is done by introducing a flexibility matrix F (as defined below Eq. 2.6.2 in the main text) and scaling the equilibrium matrix so that $\bar{Q} = QF^{-\frac{1}{2}}$. (Note: We can only scale out stiffnesses that are nonzero.) The energy can then be written in terms of $\bar{Q}$:

$$E = \frac{1}{2} u^T \bar{Q} \bar{F}^{-1} \bar{Q}^T u \tag{2.7.1}$$

where the scaled flexibility matrix $\bar{F}$ is proportional to the identity matrix except for any entries that are zero. This energy is the same as that in Eq. 2.6.3 in the main text, so the minimum energy configurations should have a one-to-one correspondence.

Scaled extension or tension vectors are related to the unscaled versions by

$$|\bar{e}\rangle = F^{-\frac{1}{2}} |e\rangle \tag{2.7.2}$$

$$|\bar{t}\rangle = F^{\frac{1}{2}} |e\rangle \tag{2.7.3}$$

Thus we have implicitly performed all of our calculations on the scaled system and have converted back when calculating η.

2.7.3 Discrete Green's function

Using the SSS and SCS sub-bases, our goal is to calculate the discrete Green's function shown in Eq. 2.6.5. We start by decomposing the bond tensions and extensions,

$$|t\rangle = \sum_{\alpha} |c_\alpha\rangle \langle c_\alpha|t\rangle + \sum_{\beta} |s_\beta\rangle \langle s_\beta|t\rangle \tag{2.7.4}$$

$$|e\rangle = \sum_{\alpha} |c_\alpha\rangle \langle c_\alpha|e\rangle + \sum_{\beta} |s_\beta\rangle \langle s_\beta|e\rangle \tag{2.7.5}$$

Now suppose we apply some external tension to the bonds, $|t^*\rangle$. The part of the external tension that projects onto the SCS basis will be balanced by tensions in the bonds, so that $\langle c_\alpha|t\rangle = \langle c_\alpha|t^*\rangle$. Additionally, the bond extensions that project onto the incompatible extensions, or SSS basis, should be zero because they are unphysical, $\langle s_\beta|e\rangle = 0$. Inserting our decompositions of the tension and extension into Eq. 2.6.2,

we get

$$\sum_{\alpha} |c_\alpha\rangle \langle c_\alpha|t^*\rangle + \sum_{\beta} |s_\beta\rangle \langle s_\beta|t\rangle = \sum_{\alpha} F^{-1} |c_\alpha\rangle \langle c_\alpha|e\rangle \tag{2.7.6}$$

If we project this equation onto the SCS vector $\langle c_{\alpha'}|$, we get a system of N_c equations,

$$\langle c_{\alpha'}|t^*\rangle = \sum_{\alpha} \langle c_{\alpha'}|F^{-1}|c_\alpha\rangle \langle c_\alpha|e\rangle \tag{2.7.7}$$

$$= \sum_{\alpha} K_{\alpha'\alpha} \langle c_\alpha|e\rangle \tag{2.7.8}$$

where $K_{\alpha'\alpha} = \langle c_{\alpha'}|F^{-1}|c_\alpha\rangle$ is an $N_c \times N_c$ square matrix. If we invert this system of equations to solve for the extensions, we get

$$\langle c_\alpha|e\rangle = \sum_{\alpha'} K^{-1}_{\alpha\alpha'} \langle c_{\alpha'}|t^*\rangle \tag{2.7.9}$$

The full extension is then

$$|e\rangle = \sum_{\alpha} |c_\alpha\rangle \langle c_\alpha|e\rangle = \sum_{\alpha\alpha'} |c_\alpha\rangle K^{-1}_{\alpha\alpha'} \langle c_{\alpha'}|t^*\rangle \tag{2.7.10}$$

In general, calculating the matrix inverse $K^{-1}_{\alpha\alpha'}$ is computationally intensive since it is a square matrix of size N_c. To improve this, we map our system to one where all the bond stiffnesses are identically k or zero as described in the previous section. Finally, we arrive at the Green's function in Eq. 2.6.5,

$$G = \frac{1}{k} \sum_{\alpha} |c_\alpha\rangle \langle c_\alpha| \tag{2.7.11}$$

2.7.4 Modifying a single bond

Using the Green's function in (2.7.11), our goal is to find the change in $|e\rangle$ when the stiffness of a given bond is modified. First we define a unique SCS basis vector for bond i,

$$|C_i\rangle = kG\,|i\rangle \tag{2.7.12}$$

This SCS is closely related to the unique SSS defined in Ref. [72]. We rotate the SCS basis so that one of the SCS vectors is $|c_\mu\rangle = |C_i\rangle\,/\sqrt{\langle C_i|C_i\rangle}$, making sure to re-orthonormalize the rest of the basis with respect to this unique SCS. The benefit of this rotation is that now only the unique SCS contains a nonzero element for bond i. Next, we introduce a separate stiffness for bond i, k_i which is not necessarily identical to the rest of the bonds. The matrix $K_{\alpha'\alpha}$ defined in the previous section can then be simplified to

$$K_{\alpha'\alpha} = \begin{cases} k_i C_i^2 + k(1 - C_i^2) & \text{if} \quad \alpha = \alpha' = \mu \\ k\delta_{\alpha\alpha'} & \text{otherwise} \end{cases} \tag{2.7.13}$$

where we have defined $C_i^2 \equiv \langle C_i|C_i\rangle = \langle i|C_i\rangle$. The resulting extensions are

$$|e\rangle = \frac{|C_i\rangle\ \langle C_i|t^*\rangle}{C_i^2[k_i C_i^2 + k(1 - C_i^2)]} + \frac{1}{k}\sum_{\alpha\neq\mu} |c_\alpha\rangle\ \langle c_\alpha|t^*\rangle \tag{2.7.14}$$

with change in extensions

$$|\Delta e\rangle = |C_i\rangle \frac{\langle C_i|t^*\rangle}{k(1-C_i^2)} \tag{2.7.15}$$

where we have taken k_i from an initial value of k to zero.

2.7.5 Modifying multiple bonds

Here we extend (2.7.15) to allow for multiple bonds that do not have identical stiffness k. Suppose that all the bond stiffnesses are identically $k_i = k$, except for a small subset of bonds which we call $\mathcal{B}$. We say a bond $i \in \mathcal{B}$ if and only if $k_i \neq k$. This set includes any ghost bonds with zero stiffness, along with bonds that are being tested for removal or modification.We typically include just three bonds in $\mathcal{B}$ – the source and target ghost bonds of zero-stiffness, along with the bond tested for removal.

Our goal now is to rotate our SCS sub-basis $|c_\alpha\rangle$ so that as few basis vectors as possible project onto the bonds in $\mathcal{B}$. We will denote this new rotated SCS sub-basis $|\tilde{c}_\alpha\rangle$. We define a special set of basis vectors $\mathcal{V}$ such that $\alpha \in \mathcal{V}$ if and only if $\langle i|\tilde{c}_\alpha\rangle \neq 0$ for some $i \in \mathcal{B}$. Typically, the size of $\mathcal{B}$ will equal the size of $\mathcal{V}$. In other words, the basis vectors in $\mathcal{V}$ are the only vectors with non-zero elements for the set of bonds with non-identical stiffnesses $\mathcal{B}$

In order to calculate our rotated SCS sub-basis, $|\tilde{c}_\alpha\rangle$, we first find the unique SCS for each bond in $\mathcal{B}$, which we denote $|C_i\rangle$ shown in (2.7.12). These unique SCS vectors

are then orthonormalized using a modified Graham-Schmidt algorithm. The result is the set of basis vectors $\mathcal{V}$ described previously. The remainder of the rotated SCS basis is found by using the modified Graham-Schmidt algorithm to orthonormalize the original SCS basis with respect to the set of vectors $\mathcal{V}$, throwing out any vectors that are completely zeroed out. The result is our set of N_c orthonormal rotated SCS vectors. However, it will be shown that only the vectors in $\mathcal{V}$ will be necessary for our solution.

Each basis vector that is not in $\mathcal{V}$ has zero projection onto bonds that are in $\mathcal{B}$, i.e. if $\alpha \notin \mathcal{V}$, then $\langle i|\tilde{c}_\alpha\rangle = 0$ for all $i \in \mathcal{B}$. This means that if either $\alpha \notin \mathcal{V}$ or $\alpha' \notin \mathcal{V}$, then $|\tilde{c}_\alpha\rangle$ and $|\tilde{c}_{\alpha'}\rangle$ are orthogonal over a reduced basis such that

$$\langle\tilde{c}_\alpha| \left(\sum_i |i\rangle \langle i|\right) |\tilde{c}_{\alpha'}\rangle = \langle\tilde{c}_\alpha| \left(\sum_{i\notin\mathcal{B}} |i\rangle \langle i|\right) |\tilde{c}_{\alpha'}\rangle \tag{2.7.16}$$

This new basis now gives us the means to rewrite $K_{\alpha\alpha'}$ for $\alpha \notin \mathcal{V}$ or $\alpha' \notin \mathcal{V}$,

$$K_{\alpha\alpha'} = \langle c_{\alpha'}|F^{-1}|c_\alpha\rangle \tag{2.7.17}$$

$$= \langle\tilde{c}_\alpha| \left(\sum_{i\in\mathcal{B}} k_i |i\rangle \langle i| + \sum_{i\notin\mathcal{B}} k |i\rangle \langle i|\right) |\tilde{c}_{\alpha'}\rangle \tag{2.7.18}$$

$$= k \sum_{i\notin\mathcal{B}} \langle\tilde{c}_\alpha|i\rangle \langle i|\tilde{c}_{\alpha'}\rangle \tag{2.7.19}$$

$$= k \langle\tilde{c}_\alpha|\tilde{c}_{\alpha'}\rangle = k\delta_{\alpha\alpha'} \tag{2.7.20}$$

The total matrix is then

$$K_{\alpha\alpha'} = \begin{cases} \tilde{K}_{\alpha\alpha'} & \text{if} \quad \alpha, \alpha' \in \mathcal{V} \\ k\delta_{\alpha\alpha'} & \text{otherwise} \end{cases} \tag{2.7.21}$$

where we have defined the sub-matrix $\tilde{K}_{\alpha\alpha'} = \langle c_{\alpha'}|F^{-1}|c_\alpha\rangle$ for $\alpha, \alpha' \in \mathcal{V}$. We see that the matrix inversion problem is simplified to just inverting $\tilde{K}_{\alpha\alpha'}$.

$$K^{-1}_{\alpha\alpha'} = \begin{cases} \tilde{K}^{-1}_{\alpha\alpha'} & \text{if} \quad \alpha, \alpha' \in \mathcal{V} \\ \frac{1}{k}\delta_{\alpha\alpha'} & \text{otherwise} \end{cases} \tag{2.7.22}$$

Since the size of $\mathcal{B}$ is very small (in our case typically a set of size 3), calculating the inverse of this matrix is very fast. The extension can now be represented as

$$|e\rangle = \sum_{\alpha,\alpha' \in \mathcal{V}} |\tilde{c}_\alpha\rangle \, \tilde{K}^{-1}_{\alpha\alpha'} \, \langle \tilde{c}_{\alpha'}|t^*\rangle + \sum_{\alpha \notin \mathcal{V}} \frac{1}{k} \, |\tilde{c}_\alpha\rangle \, \langle \tilde{c}_\alpha|t^*\rangle \tag{2.7.23}$$

The change in extension on bond i when the stiffnesses are modified is then

$$|\Delta e\rangle = \sum_{\alpha,\alpha' \in \mathcal{V}} |\tilde{c}_\alpha\rangle \, \Delta(\tilde{K}^{-1}_{\alpha\alpha'}) \, \langle \tilde{c}_{\alpha'}|t^*\rangle \tag{2.7.24}$$

Note that the solution only depends on the basis vectors in $\mathcal{V}$. This means that only this small number vectors must calculated and the rest may be neglected.

2.7.6 Avoiding the introduction of zero modes

We impose the constraint that we do not introduce any zero energy modes into the system when we remove bonds. We ensure this by only removing bonds which contribute to the SSS sub-basis. By Maxwell-Calladine counting, $N_0 - N_s = dN - N_b$, where N_0 is the number of zero modes [7]. This means that if we remove a bond, we can either add a zero mode (increase N_0) or remove a SSS (decrease N_s). If a bond is removed that contributes to the SSS sub-basis, a unique SSS will also be removed and no zero mode will be created [54]. This unique SSS, which we define as $|S_i\rangle$ for bond i, is calculated analogously to the unique SCS, $|C_i\rangle$, shown in Eq. 2.6.6. We find that

$$|S_i\rangle = \sum_{\beta} |s_\beta\rangle \, \langle s_\beta | i\rangle \tag{2.7.25}$$

As long as $S_i^2 \equiv \langle S_i | S_i \rangle > 0$, then bond i contributes to the SSS sub-basis.

2.7.7 Removing bonds from SSS and SCS sub-bases

When a bond i is removed, we remove the unique SSS vector $|S_i\rangle$ from our SSS sub-basis by subtracting off its projection onto each SSS basis vector. We also remove the entries for bond i from all vectors in both our SSS and SCS sub-bases. The two bases are then reorthonormalized using a modified Graham-Schmidt algorithm.

2.7.8 Animations

Videos 2.8 and 2.9 show animations of the responses of the networks in Fig. 2.1 in the main text, while Video 2.11 shows the response of the network in Fig. 2.4(C) (Note: To view animations and videos, please see web links in Ref. [61]). Although our algorithm only considers and controls the linear response, we show the full nonlinear deformations in these videos so that the source and target strains are clearly visible.

To calculate the nonlinear response, we start with a tuned network and minimize the nonlinear configurational energy for increments of the source strain in a cycle from from 0% to $\varepsilon_{\max}$ and back to 0%, and then to -$\varepsilon_{\max}$ and back to 0% again .The quantity $\varepsilon_{\max}$ is the maximum strain amplitude. In the network's undeformed state, each node i has an initial position vector $\mathbf{R}_i$. If the network is deformed in some way, then each node will have a new position

$$\mathbf{X}_i = \mathbf{R}_i + \mathbf{u}_i \tag{2.7.26}$$

where $\mathbf{u}_i$ is the node's displacement vector. If two nodes share a bond, then the bond vector going from node i to node j is $\mathbf{R}_{ij}$ with magnitude l_{ij}, while the deformed

bond vector is

$$\mathbf{X}_{ij} = \mathbf{X}_j - \mathbf{X}_i \tag{2.7.27}$$

$$= \mathbf{R}_j - \mathbf{R}_i + \mathbf{u}_j - \mathbf{u}_i \tag{2.7.28}$$

$$= \mathbf{R}_{ij} + \Delta\mathbf{u}_{ij} \tag{2.7.29}$$

where $\Delta\mathbf{u}_{ij}$ is the bond extension vector. The configurational energy summed over all bonds $\langle ij \rangle$ with central-force harmonic potentials is then

$$E = \sum_{\langle ij \rangle} \frac{1}{2} k_{ij} (X_{ij} - l_{ij}) \tag{2.7.30}$$

where $X_{ij} = |\mathbf{X}_{ij}|$ and k_{ij} is the stiffness of bond $\langle ij \rangle$. We minimize this energy numerically with respect to the displacement vectors $\mathbf{u}_i$ under the constraint that the source strain ε_S is a specified value.

2.7.9 Response of experimental networks

We measured the target strain of the physical realization of the network in Fig. 2.1(A) for a range of source strains. Fig. 2.12 shows that the response is a monotonic function of the source strain. Our networks, though designed in the linear regime, work well even for source strains in the nonlinear regime.

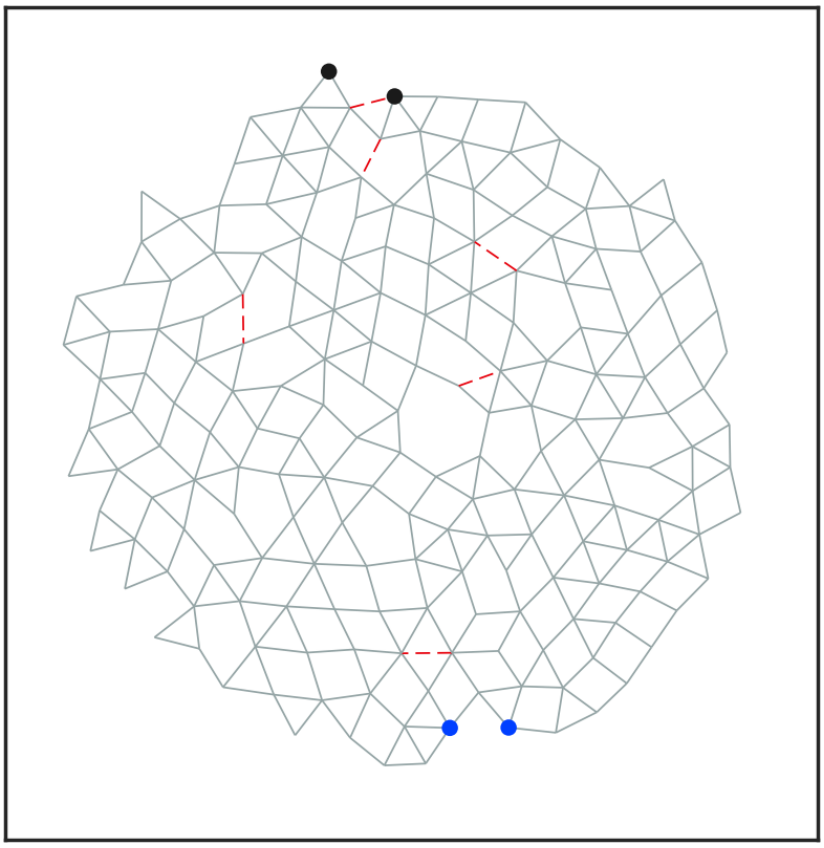

Figure 2.8: Animation of the tuned expansion response of the network in Fig. 2.1(A). The source nodes are indicated in blue, while the target nodes are black. The network has been tuned to have a strain ratio of $\eta = +1$ in the linear regime. Here we calculate the full nonlinear response for oscillatory source strain of amplitude $\varepsilon_{\max} = 40\%$ by minimizing the nonlinear configurational energy (see Appendix).

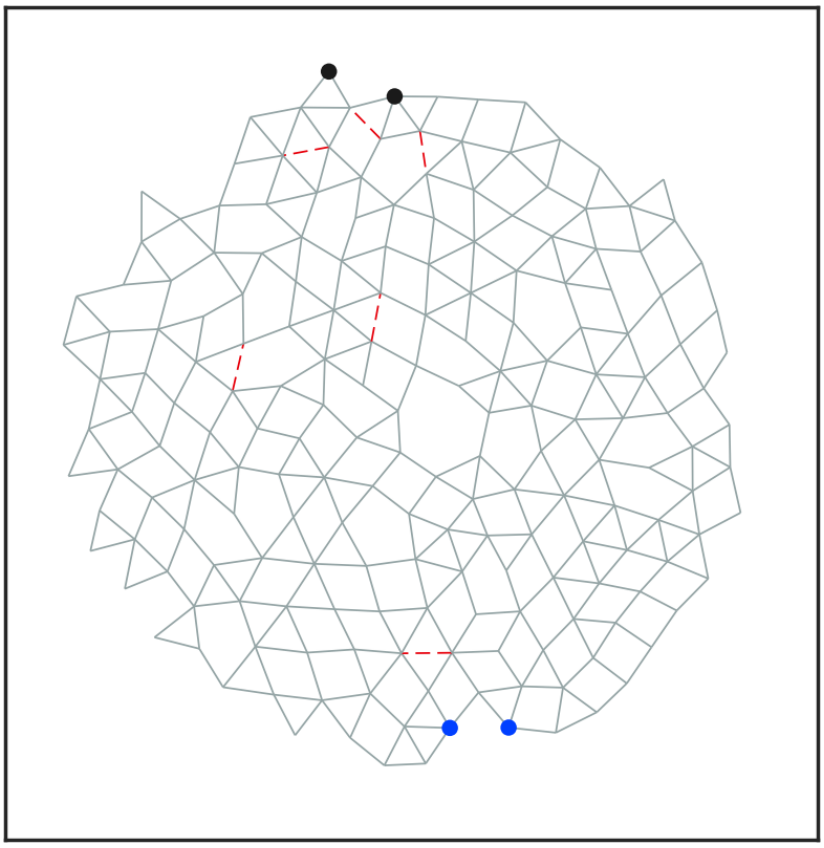

Figure 2.9: Animation of the tuned contraction response of the network in Fig. 2.1(B). The source nodes are indicated in blue, while the target nodes are black. The network has been tuned to have a strain ratio of $\eta = -1$ in the linear regime. Here we calculate the full nonlinear response for oscillatory source strain of amplitude $\varepsilon_{\max} = 40\%$ by minimizing the nonlinear configurational energy (see Appendix).

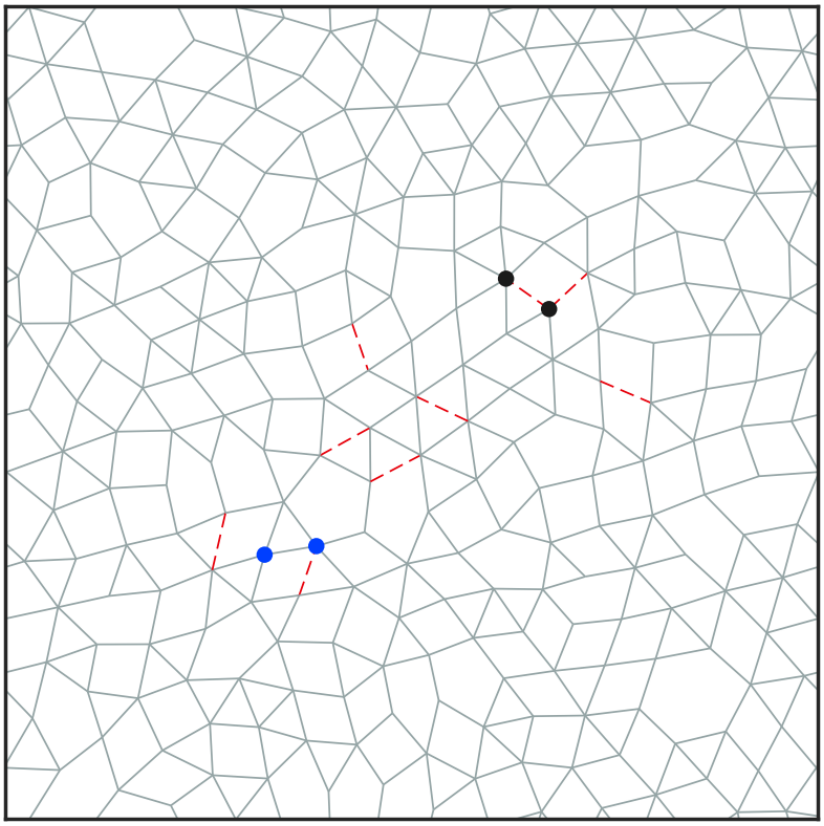

Figure 2.10: Animation of the tuned expansion response of the network in Fig. 2.4(C). The source nodes are indicated in blue, while the target nodes are black. The network has been tuned to have a strain ratio of $\eta = 1$ in the linear regime. Here we calculate the full nonlinear response for oscillatory source strain of amplitude $\varepsilon_{\max} = 40\%$ by minimizing the nonlinear configurational energy (see Appendix).

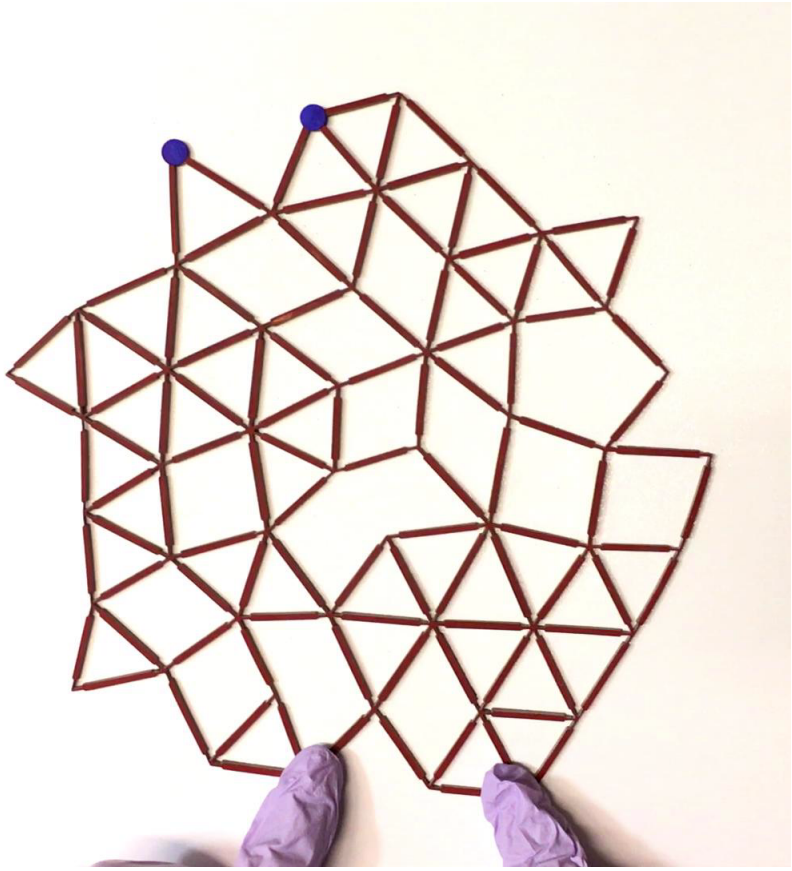

Figure 2.11: Movie of an experimental network with 51 nodes and 112 bonds tuned to show an expansion response. Output nodes are indicated in blue. The network has been tuned to have a strain ratio of $\eta = 2$ in the linear regime.

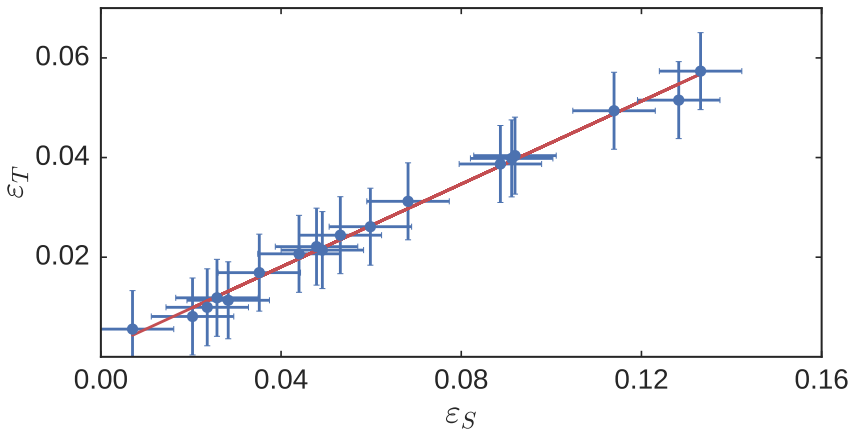

Figure 2.12: The target strain ε_T as a function of source strain ε_S is shown in blue for a physical realization of the network depicted in Fig. 2.6(A). The red line shows that the response is linear over a large range of input strains.

Chapter 3

Limits of multifunctionality in tunable networks

Note: The following content is reproduced with minor revision from Ref. [62].

3.1 Introduction

Many naturally occurring and synthetic networks are endowed with specific and efficient functionality. For example, allosteric proteins globally adjust their conformation upon ligand binding to control the activity of a distant active site [47, 59]. Venation networks in the leaves of plants are highly optimized for water and nutrient transport [66]. In some cases, networks can change their function depending on the needs of the system; vascular networks in animals [77, 48, 26], fungi [33], and slime molds [74] can reroute the transport of fluids, enhancing or depleting nutrient levels in order

to support local growth or activity. Modern power grids must precisely distribute electrical energy generated from a limited number of sources to a large number of consumers with widely varying consumption needs at different times [53]. All of these networks are optimized to some degree, by evolution via natural selection, dynamic reconfiguration, or human planning.

A key aspect of such functionality is the complexity of a specific task. We define a "function" as an optimized response of a localized component of a network when another predefined, localized component of the system is activated. A "task" is then defined as the collective response of a set of individual functions due to a single input. The number of functions representing a specific task is the task complexity.

In this work we address the limits of complexity for a single task: how many functions comprising a single task can be programmed into a network? We consider two examples: (i) mechanical networks – in which nodes are connected by central-force harmonic springs – locally flexing in response to an applied strain and (ii) flow (or resistor) networks – in which nodes are connected by linear resistors – locally producing a pressure drop due to an applied pressure at the source. These systems are related; flow networks are mathematically equivalent to mechanical networks embedded in one spatial dimension – but with a nontrivial node topology [73].

Macroscopic properties of mechanical networks, such as their bulk and and shear moduli, can be tuned by modifying only a tiny fraction of the springs between nodes [28, 34, 58] (in contrast to random removal [19]). This idea was extended

to show that such networks can be tuned to develop allosteric behavior via selective spring removal [61, 82, 21]. Allostery in these systems is a single-function task in which a randomly selected spring (the target) responds in a specified way to a strain imposed on a separate pair of nodes (the source). Here we study complex tasks in which multiple targets are controlled by a single source. We study the scaling of the maximal complexity of a task with network size by asking how many individual targets can be successfully tuned simultaneously, and show that in both flow and mechanical networks, the limit of task complexity is set by a phase transition.

3.2 Network Tuning Protocol

Our method for tuning networks follows the general scheme described in our previous work [61] with slight modifications. We start with two-dimensional configurations of soft spheres with periodic boundary conditions created using standard jamming algorithms. We construct networks by placing nodes at the centers of each sphere and links (edges) between nodes corresponding to overlapping particles. This ensemble of networks is used for both spring networks, in which edges are unstretched central-force springs, and flow networks, in which edges are resistive conduits. By using the same set of nodes and edges for both systems, we can directly compare results. We chose this ensemble because it is disordered and provides initial networks with properties reminiscent of the corresponding biological systems. Elastic networks with close-range interactions have often been used to model proteins [35], while many natural

flow networks have high numbers of closed loops [39] and are highly interconnected [5]. However, our networks do not exhibit modular topologies which can appear in some systems [53]. While we briefly touch on modularity, an in-depth study of modular networks is outside the scope of this work.

For each network, a pair of source nodes is chosen randomly, along with a set of N_T target edges. Our goal is to tune the extension (or pressure drop) e_α of each target edge, indexed by α, in response to an extension (pressure drop) e_S applied to the source nodes by adding and removing edges from the network. We explore two different types of sources: pairs of nodes connected by a randomly chosen edge and pairs of nodes that are each chosen randomly anywhere in the network (see Appendix for global compression and shear sources in mechanical networks).

To control the response of the targets, we define the response ratio $\eta_\alpha \equiv e_\alpha/e_S$ for each target. Each η_α is in general a collective property of the network; the response of each target is a function of the total network structure. Before tuning the network, we measure the initial extension (pressure drop) $e_\alpha^{(0)}$ to obtain the initial response ratio of each target $\eta_\alpha^{(0)} = e_\alpha^{(0)}/e_S$. We then tune the response ratio of each target so that its relative change as compared to the initial state is greater than or equal to a specified positive constant Δ; that is, we tune each response ratio to satisfy the constraint

$$\frac{\eta_\alpha - \eta_\alpha^{(0)}}{\eta_\alpha^{(0)}} \geq \Delta, \quad \alpha = 1, \ldots, N_T. \tag{3.2.1}$$

Thus, for mechanical networks we require contracting edges to contract more, and expanding edges to expand more. For flow networks, we require the magnitude of the pressure drop to increase without changing the direction of the flow through each target link.

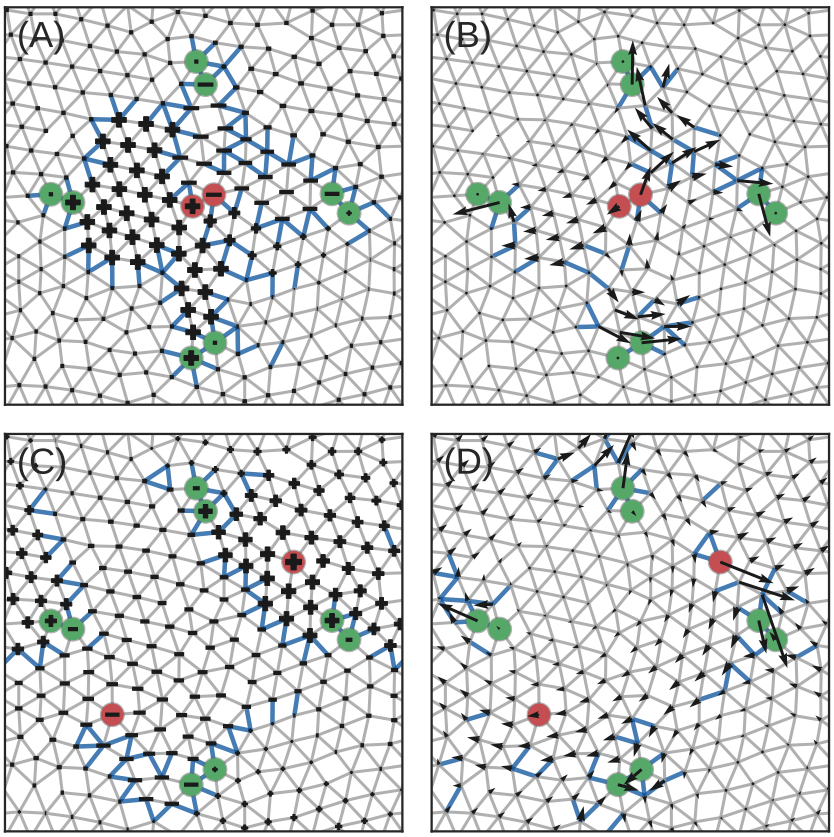

Figure 3.1: Networks tuned to display multifunctional responses. Each network starts with the same initial topology and same choice of four target edges (corresponding nodes shown in green). (A) and (C) are flow networks while (B) and (D) are mechanical network. For each network a source extension (pressure drop) is applied to a pair of source nodes (shown in red). In (A) and (B) the pair of source nodes is connected by an edge, while in (C) and (D) the source nodes are not connected by an edge. For flow networks, response ratios are tuned to $\eta_\alpha \geq 0.5$, while for the mechanical networks they are $\eta_\alpha \geq 1.0$. The edges removed by tuning are shown as thick blue lines. For flow networks, the magnitude of the pressure on each node is indicated by the node size and the sign of the node pressure is represented by the shape. For mechanical networks, the node displacements are shown as black arrows.

Our optimization scheme involves minimizing a loss function which penalizes devi-

ations from the constraints in (3.2.1) (Methods and Materials). Each optimization step consists of either removing a single link, or reinserting a previously removed link to modify the network topology in discrete steps. More specifically, at each step we measure the resulting change in the loss function for each single link removal or reinsertion, and remove or reinsert the link to most decrease the loss function.

Fig. 3.1 depicts examples of both flow and mechanical networks which have been tuned using our prescribed method for the two different types of applied sources. Fig. 3.1(A) and (B) show flow and mechanical networks, respectively, tuned to respond to a source applied to a pair of nodes connected by an edge. Fig. 3.1(C) and (D) show the same networks, but with a pair of source nodes that are not connected by an edge.

3.3 Results

For both flow and mechanical networks, we explore the effects of various aspects of the tuning problem, with particular focus on task complexity. Figs. 3.2(A) and (B) display typical results for the fraction of networks that can be tuned successfully, P_{SAT}, for flow and mechanical networks, respectively. Data is shown for a randomly chosen edge source and N_T randomly chosen target edges with a desired relative change in target response of $\Delta = 0.1$. System sizes range from $N = 8$ to 4096 nodes. Each value of P_{SAT} is calculated by tuning at least 512 independent randomly generated networks. At low N_T, $P_{SAT} \approx 1$ while at large N_T, P_{SAT} drops to zero.

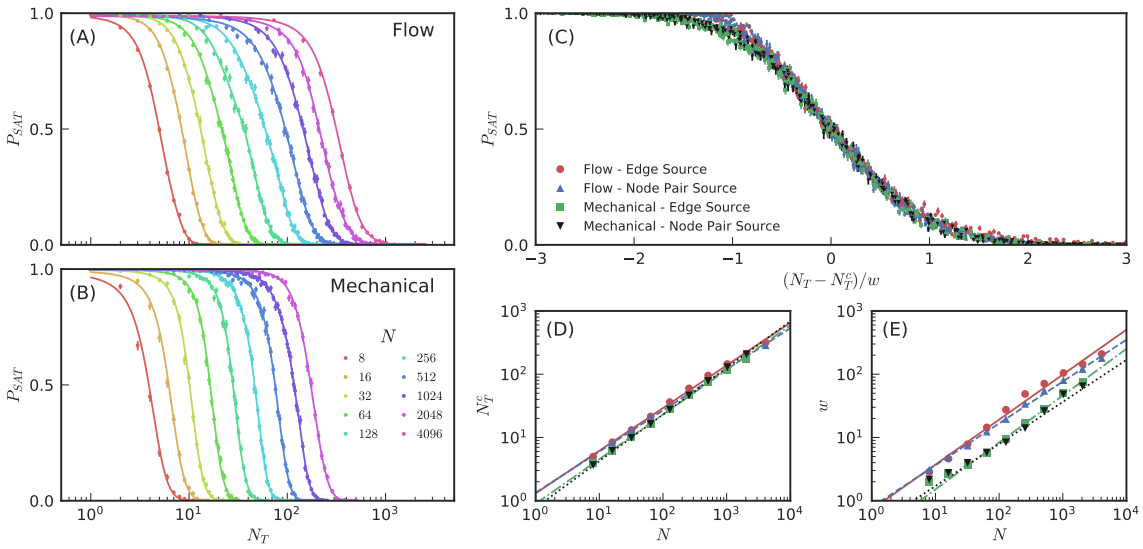

Figure 3.2: The fraction of satisfied configurations P_{SAT} for (A) flow networks and (B) mechanical networks as a function of number of targets N_T for systems of N nodes. Results are shown for a pressure or extension applied to a single source edge with a desired response ratio of $\Delta = 0.1$. Curves are smoothing splines and estimated error bars are shown for binomially distributed data (Appendix). (C) Scaling collapse for all N for four cases: flow networks with an edge source (red circles) and with a node pair source (blue triangles) and mechanical networks with an edge source (green squares) and with a node pair source (black triangles). In each case, we plot P_{SAT} vs. $(N_T - N_T^c)/w$ where $P_{SAT} = \frac{1}{2}$ at N_T^c and w is the interval in N_T over which $0.25 < P_{SAT} < 0.75$. (D) The transition points N_T^C and (E) width of the transition w are reasonably described by power laws in N with fits for N_T^c giving exponents 0.67 and 0.65 for flow networks and 0.71 and 0.74 for mechanical networks with an edge and node pair source, respectively. In the same order, the power law fits for w have exponents of 0.71, 0.66, 0.74, and 0.66.

In Fig. 3.2(C), we plot the transition curves for all system sizes for the four cases studied on the same axes. Using the smoothing spline interpolations shown in Fig. 3.2(A) and (B) (Appendix), we estimate the number of targets N_T^c at which $P_{SAT} = 0.5$. Next, we estimate the width of the transition, w, taken as the interval in N_T over which $0.25 < P_{SAT} < 0.75$. We attempt to collapse each curve by plotting P_{SAT} vs. $(N_T - N_T^c)/w$. We find a similar functional form for all cases, with only a slight difference between flow and mechanical networks near $(N_T - N_T^c)/w \approx -1$.

Figs. 3.2(D) and (E) show that flow networks and mechanical networks have similar power-law behaviors for N_T^c and w. Both the transition location and width scale approximately as N^ν with $\nu \approx 0.7$. Because the scaling exponent for N_T^c is less than 1, the critical *fraction* of functions that can be tuned simultaneously approaches zero as N goes to infinity, even though the *number* of simultaneously tuned functions diverges with system size. Thus small networks are relatively more tunable than large ones. In addition, the sub-linear scaling of the transition width shows that P_{SAT} drops more rapidly with N_T/N as N increases, implying that the crossover becomes sharp as $N \to \infty$. At the same time, Fig. 3.3 shows that the average number of links that need to be removed for a successful tuning operation grows approximately linearly with the number of targets. Thus, those networks that can be tuned successfully typically only require removal of a constant fraction of edges. Together, our results suggest $P_{SAT}(N_T/N) \sim F[(N_T/N - \rho^\infty)N^{1-\nu}]$ with ρ^∞ consistent with zero. For $\nu < 1$, this implies a random first order transition in the thermodynamic limit, with a discontinuity in P_{SAT} and power-law finite-size scaling. Such hybrid transitions are typical of constraint-satisfaction problems.

3.4 Discussion

We framed the problem of the maximum number of target edges that can be tuned successfully in a mechanical or flow network as a type of discrete constraint-satisfaction problem, in which we asked how many inequality constraints can be satisfied simul-

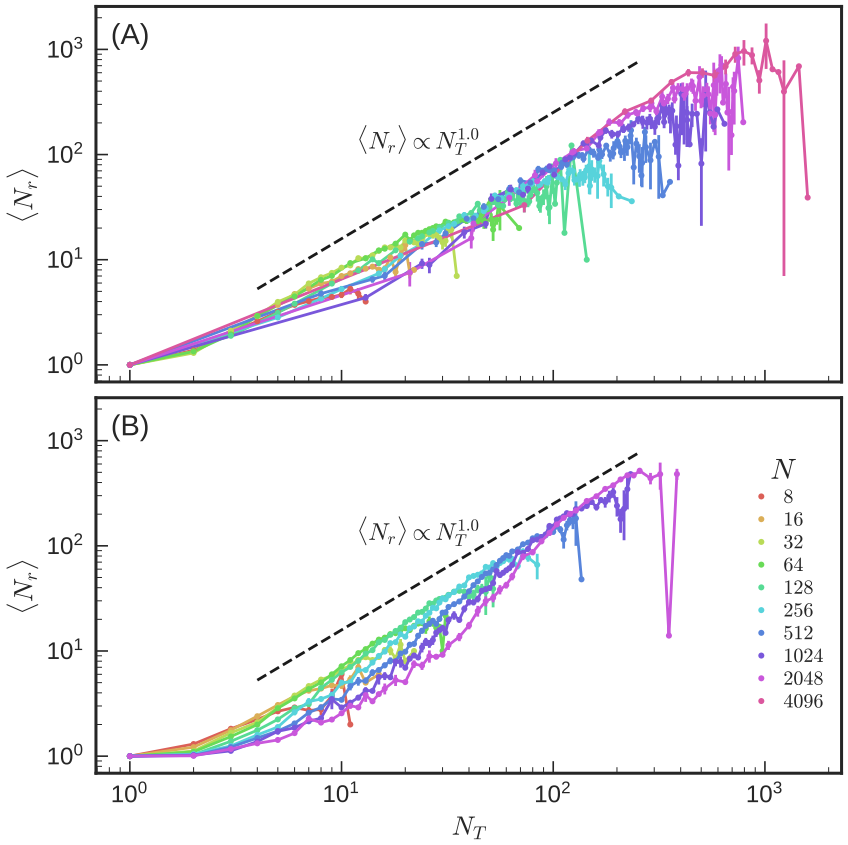

Figure 3.3: Power law behavior of the average number of removed edges as a function of number of targets N_T for (A) flow networks and (B) mechanical networks for various system sizes N. Included networks correspond to those that have been tuned successfully in Figs. 3.2(A) and (B) with an edge source and desired change in target response of $\Delta = 0.1$. Error bars indicate the error on the mean. Power laws with an exponent of 1.0 are depicted as black dashed lines for comparison.

taneously. This places the tuning of multifunctionality in the context of a variety of other problems including jamming [51], spin glasses [4], the k-SAT problem [44], k-core percolation [69], and the perceptron [23]. Much progress has been made by linking such transitions to the statistical physics of critical phenomena. The hallmark of these systems is the emergence of a SAT-UNSAT transition between regions in parameter space where the constraints can always (or with high probability) be satisfied and regions where the system is *frustrated*, such that not all constraints can

be satisfied simultaneously [23]. In mean-field, and in some cases in finite dimensions, the SAT-UNSAT transition is a random first-order transition, with a discontinuous jump in the order parameter (the fraction of satisfied configurations P_{SAT}) as in a first-order phase transition, but with power law scaling as in a second-order transition.

We have demonstrated a SAT-UNSAT transition in the complexity of a single task that can be tuned into disordered mechanical and flow networks. In both cases, the maximum task complexity diverges with a power law that is sublinear in N, the number of nodes in the network. The width of the SAT-UNSAT transition (relative to N) vanishes as N diverges, showing that the transition is a true phase transition.

Although we find $P_{SAT}(N_T/N) \sim F[(N_T/N - \rho^{\infty})N^{1-\nu}]$ for the four cases displayed in Fig. 3.2, both $F(x)$ and ν can vary depending on a variety of factors. These factors include: (i) the local or global nature of the source, (ii) the magnitude of desired change in target response Δ, (iii) disorder in the link topology, (iv) initial coordination of the network, and (v) the choice of whether to tune the link tensions (currents) or extensions (pressure drops) (Appendix). The values of ν lie in the range of 0.6-0.8, with the exception of one case of 1.0 for a very large relative change in target response of $\Delta = 1000$ (Table 3.1). We find that the behavior is not well-described by a power law for tuning negative relative changes in target response ($\Delta < 0$) and for tuning small changes in current or tension. The former case is still under investigation, while the latter exception has a simple explanation (Appendix).

Overall, the divergence of the maximum number of tunable targets with system size

and the corresponding vanishing of the transition width (indicating the existence of a phase transition) are very robust observations for positive and sufficiently large relative changes in target responses. We note also that both mechanical networks and flow networks exhibit very similar quantitative behavior despite the fact that flow networks are purely topological, requiring no explicit spatial embedding.

The SAT-UNSAT transition of the task complexity problem introduced here represents a new class of discrete constraint-satisfaction transitions due to a new complication that arises in the form of the constraints. When tuning a mechanical network, the removal of links can introduce soft modes, making it impossible to uniquely evaluate the network response, and subsequently tune a given target. Similarly, in a flow network the tuning process can lead to regions being disconnected from the source, making it impossible to tune any target in that region. To avoid such cases, at each step of the tuning process we are forced to exclude specific link removals (Methods and Materials). In both mechanical and flow networks, we find that it becomes more and more likely to introduce a soft mode/disconnected region as the task complexity increases. This makes the problem more difficult to tackle both numerically and analytically compared to previously-studied constraint-satisfaction transitions, and may lead to differences in the nature of the transition.

For mechanical functions, a perfectly engineered mechanism (e.g., a pair of chopsticks, which creates a large displacement at the tips in response to strain applied where they are held) may perform exactly one function superlatively well, but we have shown that more complex network structures are able to adapt to a number of functions

that diverges with the system size. The same argument holds for flow networks: an optimally engineered distribution network is a topological tree, perfectly suited for a specified task but at the same time "rigid," in the sense that it can not easily adapt to other tasks. The networks that we have studied are more complex than a pair of chopsticks or a topological tree, and this allows them to be tuned successfully to perform arbitrarily complex tasks.

Our finding that a disordered network topology allows for tunability may have relevance to real biological networks. For example, the development of certain vascular structures within animals are characterized by the initial appearance of a tightly meshed disordered network of veins (the vascular plexus) that is subsequently pruned and tuned to its function [6]. The initial disordered network may be a prerequisite of the great variability and versatility seen in natural networks. The tuned mechanical networks serve as simple models for multifunctional allostery in proteins (with a single regulatory site that can control more than one active site, e.g., [68, 42]) or multifunctional metamaterials. Our flow network results give insight into how to control, for example, blood and oxygen distribution in vascular systems, or power in an electrical network. Indeed, we find very similar behavior in a flow network with nonplanar topology derived from the UK railroad network, which exhibits a high degree of modularity. P_{SAT} exhibits a qualitatively similar transition in the number of targets that can be tuned as the networks studied here (Appendix).

Our results raise a number of issues for future investigation. The divergence in the task complexity and vanishing of the transition width with system size are reasonably

well-approximated by power laws but may deviate for larger system sizes (Appendix). The measured exponents appear to depend on many specific properties of the problems studied. This may be due to corrections to scaling or to a more fundamental deviation from power-law scaling. Also, it is not clear what conditions on the network topology are necessary to observe the transition we see. For example, networks with high degrees of modularity may not be able to support tasks spanning multiple neighborhoods. However, our results for the UK railroad network suggest that even in this case, we observe identical qualitative behavior, but with an overall decreased P_{SAT} corresponding to the possibility of choosing sources and targets in different neighborhoods (Appendix). More generally, it has not been investigated how the results depend on network structure/topology and dimensionality nor how they depend on the tuning algorithm. For instance, the values of N_T^c/N and ν might be higher for simulated annealing, which explores a wider region of solution space than the minimization algorithm studied here.

One further aspect of our results deserves mention: a simple function that controls only a single pair of target nodes can be achieved in an extremely large number of ways. We have shown that a task can be complex with N_T randomly chosen target nodes controlled by a single source. However, if one is only interested in controlling a single target, one can create different paths for its control by choosing any of the N other nodes in the system also to be a target. Likewise, one could specify a third node to be controlled as well, etc. That means that there are at least $\sim (N-1)!/(N-N_T^c)!(N_T^c-1)!$ ways of creating that simple function. Because we

find $N_T^c \sim N^\nu$, for $\nu < 1$ this lower bound is smaller than the prediction of $e^{\mathcal{O}(N)}$ solutions in the large-N limit [82].

Here we studied the limits of the complexity of a single task. It would be interesting to understand how many different tasks can be designed successfully, and whether that is controlled by a similar SAT-UNSAT transition. Finally, we note that for the mechanical and flow networks studied here, the behavior is governed by a discrete Laplacian operator [57]–mechanical networks obey force balance on each node and flow networks obey Kirchhoff's law. However, many networks, such as gene regulatory networks, metabolic networks, social networks, etc. are non-conservative. Moreover, the problems we have studied are linear in their couplings but ecological networks or neural networks, for example, are typically nonlinear. It is known that even non-conservative and/or nonlinear networks, such as the Hopfield model and jammed packings, can support SAT-UNSAT transitions as well [22, 43]. It would interesting to study systematically how conservation constraints and linearity affect the nature of the transition.

3.5 Methods

3.5.1 Linear Response

Our networks are described by a set of N nodes and N_E edges. The response of a flow network to external stimuli is represented by a pressure p_i on each node i. Analogously, the response of a d-dimensional mechanical network is the d-dimensional displacement vector $\vec{u}_i$ of each node. Each edge linking nodes i and j is characterized by either a conductance or stiffness, denoted k_{ij} in both cases. For mechanical networks, $k_{ij} = \lambda_{ij}/\ell_{ij}$ where λ_{ij} is the stretch modulus per unit length and ℓ_{ij} is the rest length. Initially, we set all stretch moduli λ_{ij} identically to one. Similarly, for flow networks we set all conductivities k_{ij} to one. Removing an edge ij corresponds to setting k_{ij} to zero, whereas reinserting an edge corresponds to setting k_{ij} back to its original value.

To calculate the response of each type of network, we minimize the corresponding functional. In the case of flow networks, we minimize the power loss through the network,

$$P = \sum_{\langle ij \rangle} k_{ij}(p_j - p_i)^2 \tag{3.5.1}$$

where $\langle ij \rangle$ indicates a sum over all edges. For mechanical networks, we minimize the

elastic energy

$$E = \frac{1}{2} \sum_{\langle ij \rangle} k_{ij} \left[\hat{b}_{ij} \cdot (\vec{u}_j - \vec{u}_i) \right]^2 \tag{3.5.2}$$

where $\hat{b}_{ij}$ is a unit vector pointing from node i to node j in the undeformed configuration. The power loss for a flow network can be mapped to the energy of a mechanical network for $d = 1$ by mapping the pressure on each node to a one-dimensional displacement [73]. In this case, the unit vectors $\hat{b}_{ij}$ are scalars with values of either ± 1, which drop out when squared; the embedding of the network in space does not matter as is be expected for flow networks.

Minimizing (3.5.1) for a flow network in the presence of externally applied boundary currents q_i on each node i, we obtain a system of linear equations characterized by a graph Laplacian L,

$$L \left| p \right\rangle = \left| q \right\rangle \tag{3.5.3}$$

where $\left| p \right\rangle$ is an N-dimensional vector of node pressures and $\left| q \right\rangle$ is a N-dimensional vector of external currents on nodes. We define the vector $\left| i \right\rangle$ so that the pressure and current on the ith node are $p_i = \langle i | p \rangle$ and $q_i = \langle i | q \rangle$, respectively. Similarly for mechanical networks, minimizing (3.5.2) in the presence of externally applied forces, we obtain

$$H \left| u \right\rangle = \left| f \right\rangle \tag{3.5.4}$$

where $|u\rangle$ is an dN-dimensional vector of node displacements and $|f\rangle$ is a dN-dimensional vector of external forces on nodes. Again we define the $N \times d$ matrix $|i_d\rangle$ to pick out the displacement and force on the ith node, $\vec{u}_i = \langle i_d|u\rangle$ and $\vec{f}_i = \langle i_d|f\rangle$. The matrix H is the matrix of second derivatives known as the dynamical or Hessian matrix and can be interpreted as graph Laplacian where each element is a $d \times d$ matrix. We define the d-Laplacian, denoted L_d, as a generalized version of the standard Laplacian matrix. The case $d = 1$ corresponds to the Laplacian of a flow network (or a one-dimensional mechanical network) such that $L_1 = L$, while for $d > 1$, L_d is a Hessian for a d-dimensional mechanical network, i.e. $L_{d>1} = H$. The ijth $d \times d$-block of the d-Laplacian is

$$\langle i_d|L_d|j_d\rangle = \begin{cases} \sum_{l\neq i} k_{il}\hat{b}_{il}\hat{b}_{il}^T & \text{if} \quad i = j \\ -k_{ij}\hat{b}_{ij}\hat{b}_{ij}^T & \text{if} \quad i \neq j \end{cases} \tag{3.5.5}$$

where k_{ij} is nonzero only if edge ij exists.

Consequently, the response of either type of network is calculated by solving the corresponding set of linear equations rewritten as

$$L_d\,|u\rangle = |f\rangle \tag{3.5.6}$$

where $|u\rangle$ and $|f\rangle$ are the appropriate dN-dimensional response and source vectors, respectively. To apply a pressure drop or edge extension source, we use a bordered Laplacian formulation.

3.5.2 Bordered Laplacian Formulation

Calculating the linear response requires solving (3.5.6). However, there are two complications. The first is that the Laplacian operator is in general not invertible due to the presence of global degrees of freedom. For a periodic network, in d dimensions, there are d global translational degrees of freedom. Second, we apply edge extension (pressure drop) sources, rather than tension (current) sources. These sources can be applied as constraints on the system. Using a bordered Laplacian formulation, we add a constraint for each global translation and for the source.

First, we define the extension (or pressure drop) of the source as

$$e_S = \hat{b}_S \cdot (\vec{u}_{S_2} - \vec{u}_{S_1}) = \langle S|u\rangle \tag{3.5.7}$$

with source nodes S_1 and S_2. The unit vector $\hat{b}_S$ points from node S_1 to S_2 and is a scalar in the case of a flow network. The vector $|S\rangle$ is defined to extract the extension of the source from the full vector of node displacements. We specify the desired extension as e_S^*. Additionally, we define the vectors $|G_i\rangle$ for $i = 1, \ldots, d$ corresponding to translations of the entire system uniformly along the ith axis. We define the Lagrangian

$$\mathcal{L} = E - \sum_{i=1}^{d} \lambda_i \langle G_i|u\rangle - \lambda_S(e_S - e_S^*) \tag{3.5.8}$$

where the parameters λ_i and λ_S are Lagrange multipliers. We include the Lagrange

multipliers as additional unknown parameters that must be determined in our calculations. We find solutions by extremizing the Lagrangian with respect to both the displacements and Lagrange multiplier. We rewrite the Lagrangian in matrix form:

$$\mathcal{L} = \frac{1}{2}\langle u|L_d|u\rangle - \langle\lambda_G|G^T|u\rangle - \lambda_S(\langle S|u\rangle - e_S^*). \tag{3.5.9}$$

The vector $|\lambda_G\rangle$ is size d with elements $\langle i|\lambda_G\rangle = \lambda_i$ and G is a size $dN \times d$ matrix with columns $G|i\rangle = |G_i\rangle$. In this context we can further condense notation, writing the Lagrangian as

$$\mathcal{L} = \frac{1}{2}\langle\overline{u}|\overline{L}_d|\overline{u}\rangle \tag{3.5.10}$$

where we define the bordered Laplacian $\overline{L}_d$ as a block matrix of second derivatives of the Lagrangian.

$$\overline{L}_d = \begin{pmatrix} L_d & -G & |S\rangle \\ -G^T & 0 & 0 \\ \langle S| & 0 & 0 \end{pmatrix}. \tag{3.5.11}$$

We also define the bordered displacement and force vectors $|\overline{u}\rangle$ and $|\overline{f}\rangle$, respectively,

each of size $dN + d + 1$ as

$$|\overline{u}\rangle = \begin{pmatrix} |u\rangle \\ |\lambda_G\rangle \\ \lambda_S \end{pmatrix}, \quad |\overline{f}\rangle = \begin{pmatrix} |f\rangle \\ 0 \\ -e_S^*. \end{pmatrix}. \tag{3.5.12}$$

As a result, the system of equations we must solve is now $\overline{L}_d\,|\overline{u}\rangle = |\overline{f}\rangle$. The bordered Laplacian is invertible due to the presence of the constraints and solving this equation is straightforward.

3.5.3 Tuning Loss Function

Framed according to (3.2.1), the problem of tuning a complex task can be viewed as a constraint-satisfaction problem. The goal is to find a set of stiffnesses (conductivities) that simultaneously satisfy each constraint in (3.2.1). To study this problem numerically, we recast it as an optimization problem in the style of Ref. [23], in which we define an objective function that penalizes deviation of the system's behavior from the desired multifunctionality. Thus, we introduce the loss function

$$\mathcal{F}[\{k_{ij}\}] = \frac{1}{2}\sum_{\alpha=1}^{N_T} r_\alpha^2 \Theta(-r_\alpha), \tag{3.5.13}$$

which is a function of the set of all the spring constants (conductivities) $\{k_{ij}\}$, and is composed of a sum over the set of N_T target edges to be tuned. For each target edge

α we define the residual

$$r_\alpha = \frac{\eta_\alpha - \eta_\alpha^{(0)}}{\eta_\alpha^{(0)}} - \Delta. \tag{3.5.14}$$

which measures how close each target is to being tuned successfully. The Heaviside function $\Theta(-r_\alpha)$ is included so that if $r_\alpha > 0$, i.e., the response ratio has increased at least by the desired proportion Δ, then the residual does not contribute to the loss function.

3.5.4 Optimization Method

Our method for tuning a network involves minimizing the loss function in (3.5.13). In the spirit of [28, 61], our optimization consists of removing or reinserting previously removed edges from the network one at a time, modifying the network topology in discrete steps. More specifically, we use a greedy algorithm in which we remove or reinsert the edge which minimizes the loss function at each step. This requires a calculation of the new response for each possible move.

Suppose we have a network whose stiffnesses at the current step are $\{k_{ij}\}$ for all valid ij where some k_{ij} might already be zero, having been removed at previous steps. Our goal is to measure the change in response when the stiffness of edge ij is changed by

an amount Δk_{ij}. We note that the Laplacian can be decomposed as

$$L_d = QKQ^T \tag{3.5.15}$$

where the equilibrium (or incidence) matrix Q of size $dN \times N_E$ defines the mapping of nodes to edges[54, 57] and K is a size $N_E \times N_E$ diagonal matrix of edge stiffnesses such that $\langle ij|K|lm\rangle = k_{ij}\delta_{ij,lm}$. We can define a bordered incidence matrix $\overline{Q}$ by appending $d+1$ rows of zeros to Q, giving us a corresponding decomposition of the bordered Laplacian $\overline{L}_d = \overline{Q}K\overline{Q}^T$. The change in response is

$$|\Delta\overline{u}\rangle = \left[\left(\overline{L}_d + \Delta\overline{L}_d\right)^{-1} - \overline{L}_d^{-1}\right]|\overline{f}\rangle \tag{3.5.16}$$

with the corresponding change in the bordered Laplacian $\Delta\overline{L}_d = \Delta k_{ij}\,|q_{ij}\rangle\langle q_{ij}|$ with the vector $|q_{ij}\rangle = \overline{Q}\,|ij\rangle$. We now need to calculate the inverse of the updated bordered Laplacian. This can be done using the Sherman-Morrison formula [70]

$$\left(\overline{L}_d + \Delta\overline{L}_d\right)^{-1} = \overline{L}_d^{-1} - \frac{\overline{L}_d^{-1}\Delta k_{ij}\,|q_{ij}\rangle\langle q_{ij}|\,\overline{L}_d^{-1}}{1 - \Delta k_{ij}\,\langle q_{ij}|\overline{L}_d^{-1}|q_{ij}\rangle} \tag{3.5.17}$$

The change in response is then

$$|\Delta\overline{u}\rangle = -\frac{\overline{L}_d^{-1}\Delta k_{ij}\,|q_{ij}\rangle\langle q_{ij}|\,\overline{L}_d^{-1}\,|\overline{f}\rangle}{1 - \Delta k_{ij}\,\langle q_{ij}|\overline{L}_d^{-1}|q_{ij}\rangle} \tag{3.5.18}$$

The new response is then used to calculate an updated loss function.

In order to reduce numerical error and maintain the numerical invertibility of the bordered Laplacian, we define the quantity

$$S_{ij}^2 \equiv 1 - \Delta k_{ij} \langle q_{ij} | \overline{L}_d^{-1} | q_{ij} \rangle \tag{3.5.19}$$

If S_{ij}^2 is less than 10^{-4}, we do not remove an edge. This quantity can be shown to be the contribution of an edge to the states-of-self-stress in mechanical systems [72, 34]. By ensuring that every removed edge has some contribution to the states-of-self-stress, then by Maxwell-Calladine counting, we are guaranteed that no zero modes are introduced [7].

We repeatedly add or remove edges until either the loss function is explicitly zero (i.e., all constraints are satisfied), or the relative change in the objective function is less than 10^{-8}.

3.6 Appendix

3.6.1 Variations of the network tuning problem

We performed many variations of the standard network tuning problem presented in the main text. The default simulation parameters we used were a pressure (flow networks) or extension (mechanical networks) source, a target relative change in response of $\Delta = 0.1$, and an average node coordination of $Z = 2N_E/N \approx 5.0$. For

both flow and mechanical networks, we studied the two cases in which the two source nodes were connected by a single edge and where the two source nodes were chosen randomly from all the nodes, giving 4 cases altogether that we discuss in the main text. Table 3.1 shows the many variations on these parameters that we explored, along with the resulting power law exponents where applicable and the corresponding figures showing the satisfiability transitions and scaling of the transition position N_T^c and width w. Each set of simulations had at least 128 simulations per data point to calculate the satisfaction probability. The first section of the table shows the data for the four cases discussed in the main text. The second and third sections show configurations for flow and mechanical networks, respectively for higher values of the target relative change Δ. The fourth and fifth sections show results for random networks with $Z \approx 4.1$ (close to isostaticity for mechanical networks) and initially perfect triangular lattices. The sixth section shows configurations for tuning the response with global strains applied to mechanical networks. The seventh section shows results for tuning a target current in response to a current source (flow networks) or target tension in response to a tension source (mechanical networks). Finally, the last two sections show results for a negative relative change in the target response for flow and mechanical networks. All variations on the tuning problem show qualitatively similar power law behavior except for tuning small changes in current or tension (see Section "Tuning target current") or negative desired relative changes in target response, $\Delta < 0.0$) (see Section "Tuning negative target change Δ").

Tuning target current

In Table 3.1, we do not list exponents for flow networks tuned for target current nor mechanical networks tuned for target tension with $\Delta = 0.1$. As seen in Figs. 3.10(A) and (B), these cases do not result in the typical power law behavior seen elsewhere. Instead we find that it is almost always possible to achieve the desired response. This stems from the fact that the current in flow networks or tension in mechanical networks can be trivially increased in magnitude by simply removing the source edge. Typically, the source edge acts as either a resistor or a spring in parallel to the rest of the network, diverting a significant fraction of all current or tension through that edge. If the source edge is removed, then the magnitude of the current or tension is increased without changing the sign. We find that this increase is always enough to satisfy at least a 10% change in magnitude ($\Delta = 0.1$), but not enough to satisfy $\Delta = 1.0$ in flow networks nor $\Delta = 10.0$ in mechanical networks. For these latter cases, the resulting transitions revert back to the typical behavior seen elsewhere.

Tuning negative target change Δ

The last two sections of Table 3.1 contain the sets of variables we tested for the alternate case of a negative relative target response, $\Delta < 0$. The resulting transitions are depicted in Figs. 3.11 and 3.12. For these cases, we flip the inequality in Eq. (1),

resulting in the constraints

$$\frac{\eta_\alpha - \eta_\alpha^{(0)}}{\eta_\alpha^{(0)}} \leq \Delta, \alpha = 1, \ldots, N_T. \tag{3.6.1}$$

Note that $\Delta > 0$ corresponds to increasing the magnitude of the response without changing the sign, $-1 < \Delta < 0$ corresponds to decreasing the magnitude of the response without changing the sign, and $\Delta < -1$ corresponds to tuning target responses of the opposite sign from the source. For $\Delta < 0$, we do not always see a simple power law behavior for reasons that are still under investigation.

Transition in the UK rail network

In order to demonstrate that real transportation networks possess properties similar to those of the jammed packing topologies considered in the main text, we analyze three networks derived from the UK rail network presented in Ref. [25]. (i) In Fig. 3.13, we measure P_{SAT} for the full network consisting of $N = 2490$ nodes and $N_E = 4377$ edges for both a node pair source and edge source depicted as blue curves with circular symbols. (ii) While the rail network comprises a single connected component, it contains several parts which are connected through bridges, edges whose removal creates two disconnected components. Because a source located in one such component does not influence any other component, we remove all bridges in the rail network graph and focus on the remaining largest connected component, which consists of $N = 2030$ nodes and $N_E = 3868$ edges. The resulting P_{SAT} curves are

shown as the green curves with square symbols in Fig. 3.13. (iii) Within the largest connected component, there are edges whose pressure difference is always zero. For example, such edges may belong to a part of the largest connected component that is connected to the source through only a single node – such a node is topologically equivalent to a bridge. Therefore, we also measure P_{SAT} for the largest connected component where these special edges are excluded from being chosen as targets. The resulting curves are shown in Fig. 3.13 in red with triangular symbols. Each case demonstrates decreasing levels of modularity in order from (i) to (iii). In all three cases, we find that the P_{SAT} curves are qualitatively similar to the results we found for networks derived from jammed packings, with increasing modularity resulting in overall lower values of P_{SAT}.

Table 3.1: Variations of tuning problem and corresponding transition exponents

Physical System	Source Properties	Target Properties	Target Change Δ	Network Properties	Transition Position Exponent ν	Figure(s)
Flow	Edge Pressure Drop	Edge Pressure Drop	0.1	Random - $Z \approx 5.0$	0.7	3.1(A), 3.2(A), 3.3, 3.4(A)
Mechanical	Edge Extension	Edge Extension	0.1	Random - $Z \approx 5.0$	0.7	3.1(B), 3.2(B), 3.3, 3.4(B)
Flow	Node Pair Pressure Drop	Edge Pressure Drop	0.1	Random - $Z \approx 5.0$	0.7	3.1(C), 3.3, 3.4(C)
Mechanical	Node Pair Extension	Edge Extension	0.1	Random - $Z \approx 5.0$	0.7	3.1(D), 3.3, 3.4(D)
Flow	Edge Pressure Drop	Edge Pressure Drop	**1.0**	Random - $Z \approx 5.0$	0.7	3.5(A)
Flow	Edge Pressure Drop	Edge Pressure Drop	**10.0**	Random - $Z \approx 5.0$	0.8	3.5(A)
Mechanical	Edge Extension	Edge Extension	**1.0**	Random - $Z \approx 5.0$	0.7	3.6(A)
Mechanical	Edge Extension	Edge Extension	**10.0**	Random - $Z \approx 5.0$	0.7	3.6(B)
Mechanical	Edge Extension	Edge Extension	**100.0**	Random - $Z \approx 5.0$	0.8	3.6(C)
Mechanical	Edge Extension	Edge Extension	**1000.0**	Random - $Z \approx 5.0$	1.0	3.6(D)
Flow	Edge Pressure Drop	Edge Pressure Drop	0.1	**Random - Z $\approx$ 4.1**	0.7	3.7(A)
Mechanical	Edge Extension	Edge Extension	0.1	**Random - Z $\approx$ 4.1**	0.7	3.7(B)
Flow	Edge Pressure Drop	Edge Pressure Drop	0.1	**Triangular Lattice**	0.8	3.8(C)
Mechanical	Edge Extension	Edge Extension	0.1	**Triangular Lattice**	0.7	3.8(D)
Mechanical	**Global Shear**	Edge Extension	0.1	Random - $Z \approx 5.0$	0.7	3.9(A)
Mechanical	**Global Expansion**	Edge Extension	0.1	Random - $Z \approx 5.0$	0.6	3.9(B)
Flow	Edge Current	**Edge Current**	0.1	Random - $Z \approx 5.0$	N/A	3.10(A)
Flow	Edge Current	**Edge Current**	**1.0**	Random - $Z \approx 5.0$	0.7	3.10(B)
Mechanical	Edge Tension	**Edge Tension**	0.1	Random - $Z \approx 5.0$	N/A	3.10(C)
Mechanical	Edge Tension	**Edge Tension**	**10.0**	Random - $Z \approx 5.0$	0.7	3.10(D)
Flow	Edge Pressure Drop	Edge Pressure Drop	**−1.5**	Random - $Z \approx 5.0$	N/A	3.11(A)
Flow	Edge Pressure Drop	Edge Pressure Drop	**−1.0**	Random - $Z \approx 5.0$	N/A	3.11(B)
Flow	Edge Pressure Drop	Edge Pressure Drop	**−0.5**	Random - $Z \approx 5.0$	N/A	3.11(C)
Mechanical	Edge Extension	Edge Extension	**−1.5**	Random - $Z \approx 5.0$	N/A	3.12(A)
Mechanical	Edge Extension	Edge Extension	**−1.0**	Random - $Z \approx 5.0$	N/A	3.12(B)
Mechanical	Edge Extension	Edge Extension	**−0.5**	Random - $Z \approx 5.0$	N/A	3.12(C)

N/A indicates power law estimates not applicable due to lack of transition, or clearly non-power-law-like behavior.
Bold text indicates changes from default parameters.

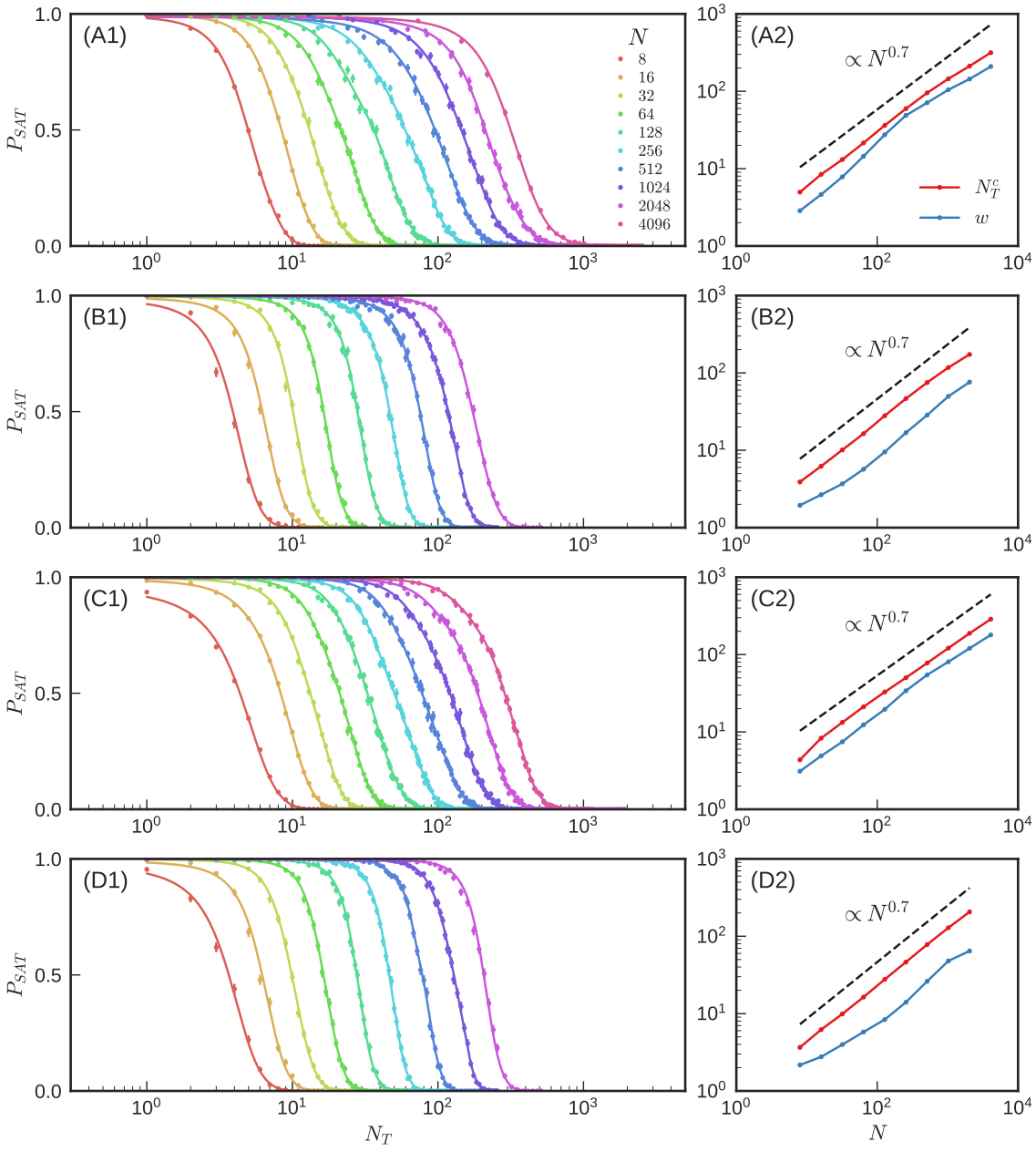

Figure 3.4: Satisfaction probability and scaling of the transition position and width for the four main cases shown in the main text: (A) flow networks and (B) mechanical networks with an edge source and (C) flow networks and (D) mechanical networks with a node pair source. See Table 3.1 for more details.

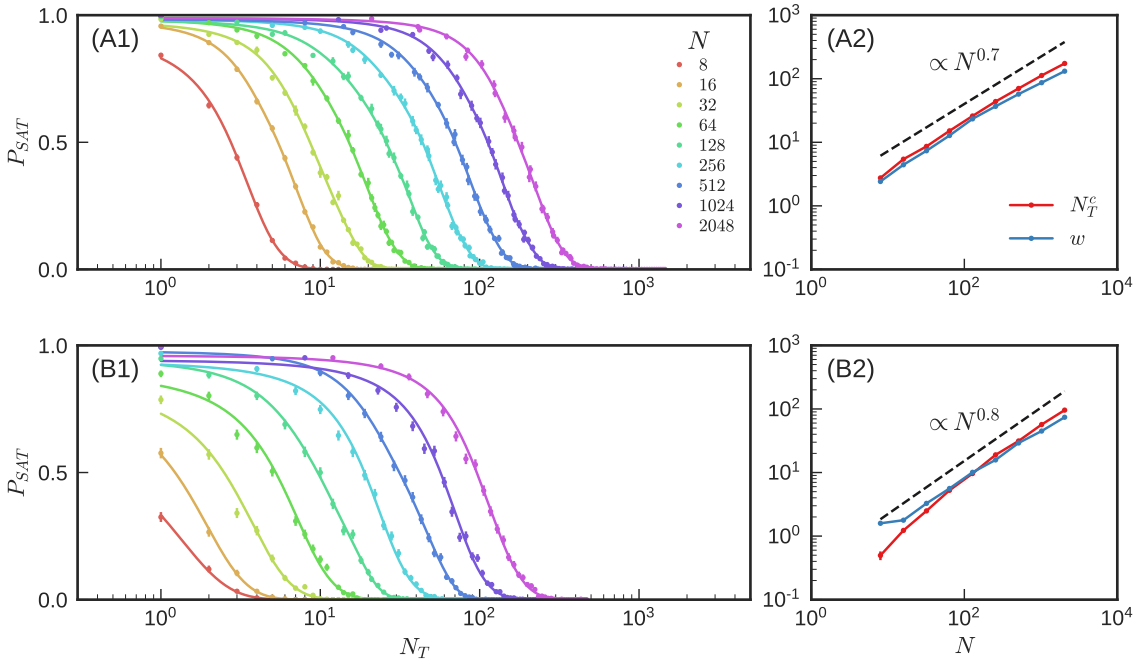

Figure 3.5: Satisfaction probability and scaling of the transition position and width for flow networks with desired relative change in target response of (A) $\Delta = 1.0$ and (B) $\Delta = 10.0$. See Table 3.1 for more details.

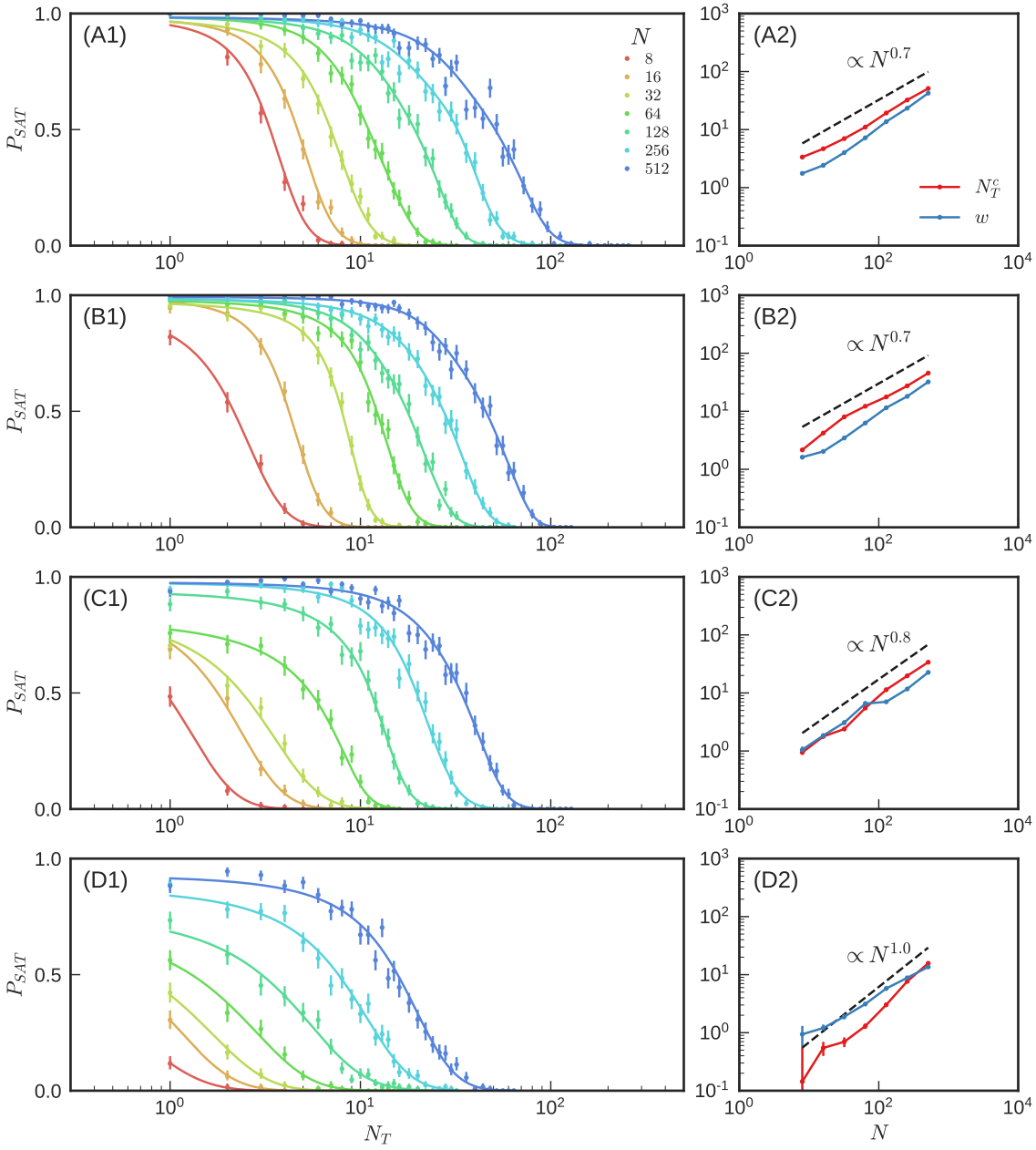

Figure 3.6: Satisfaction probability and scaling of the transition position and width for mechanical networks with desired relative change in target response of (A) $\Delta = 1.0$, (B) $\Delta = 10.0$, (C) $\Delta = 100.0$, and (D) $\Delta = 1000.0$. See Table 3.1 for more details.

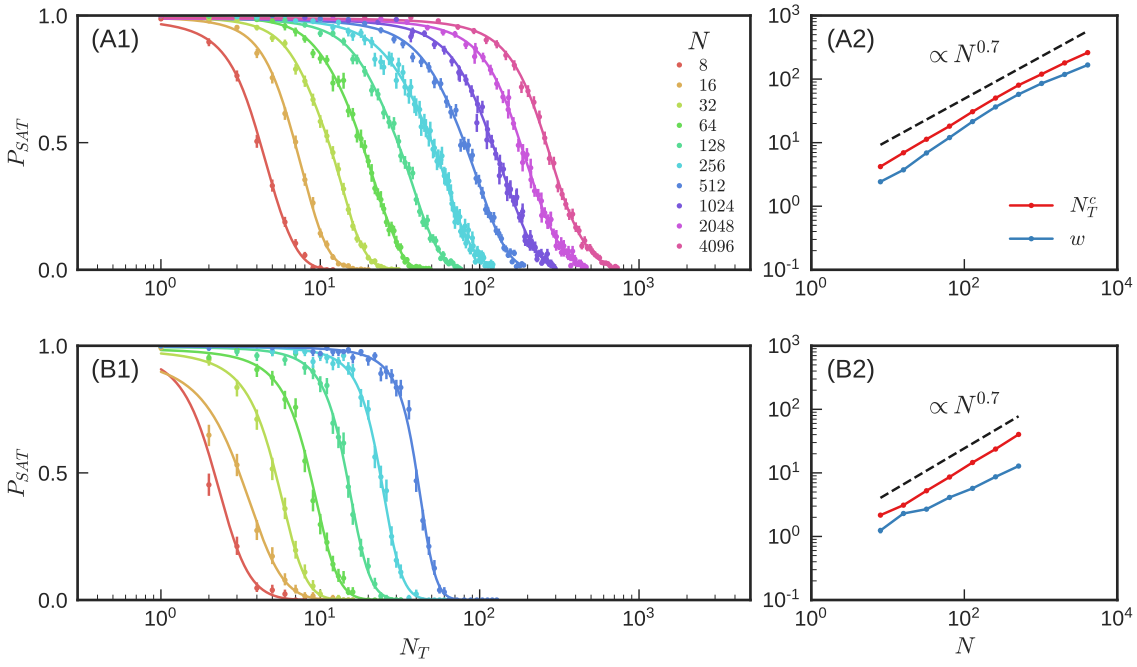

Figure 3.7: Satisfaction probability and scaling of the transition position and width for (A) flow networks and (B) mechanical networks with average connectivity of $Z \approx 4.1$, lower than the default of $Z \approx 5.0$. See Table 3.1 for more details.

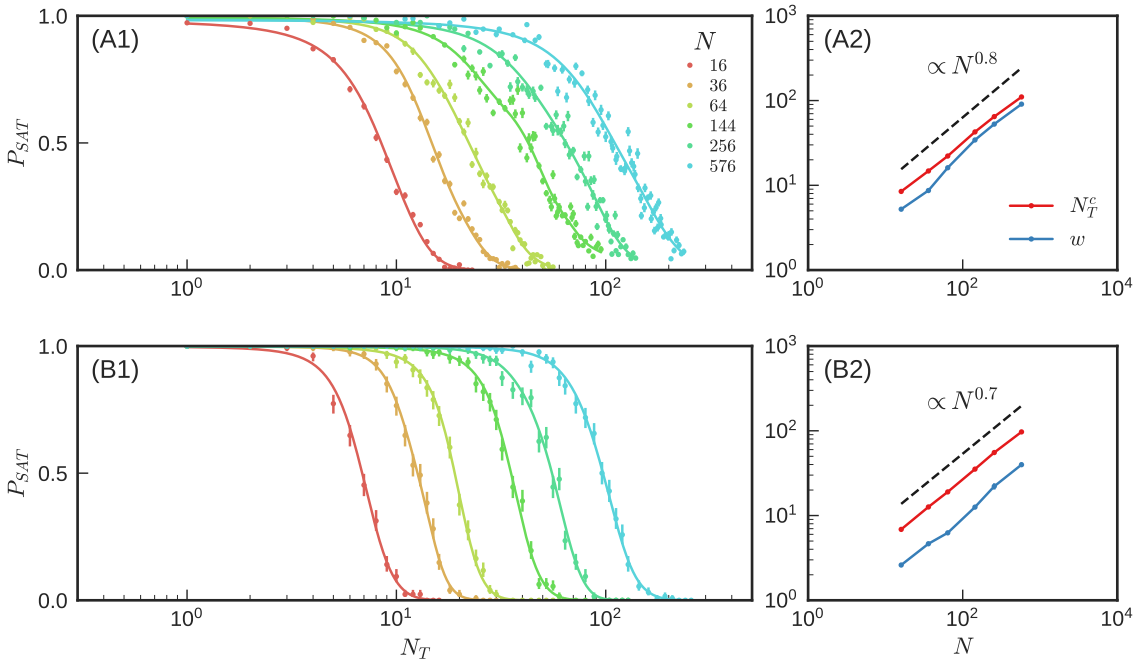

Figure 3.8: Satisfaction probability and scaling of the transition position and width for (A) flow networks and (B) mechanical networks on an ordered triangular lattice. See Table 3.1 for more details.

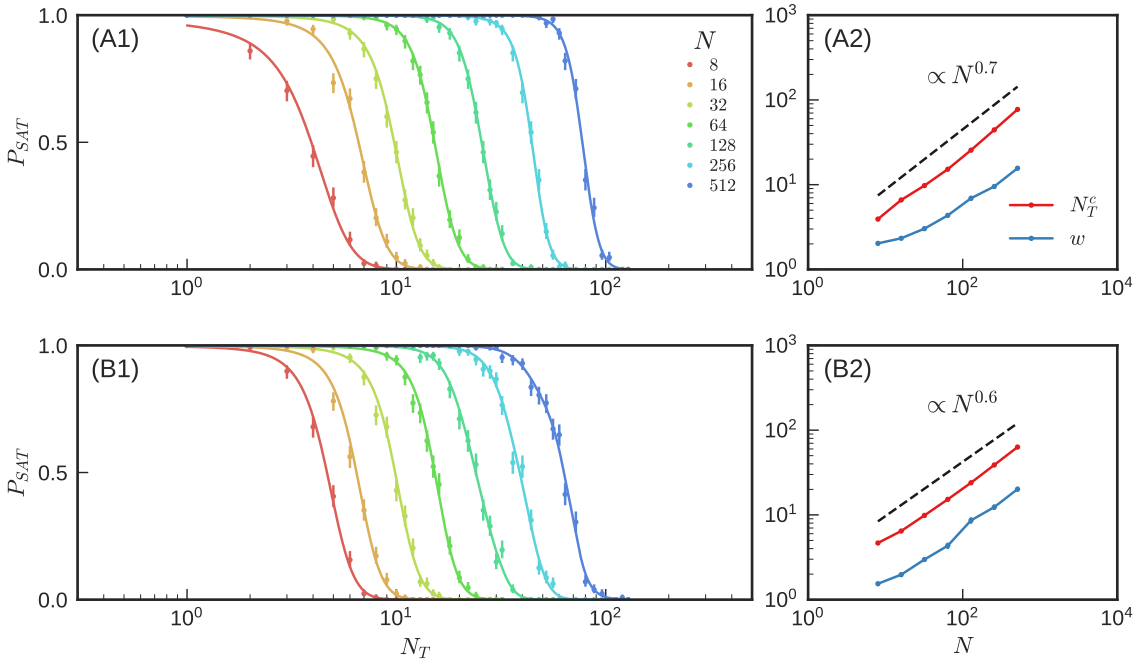

Figure 3.9: Satisfaction probability and scaling of the transition position and width for mechanical networks with global (A) shear and (B) compression sources. See Table 3.1 for more details.

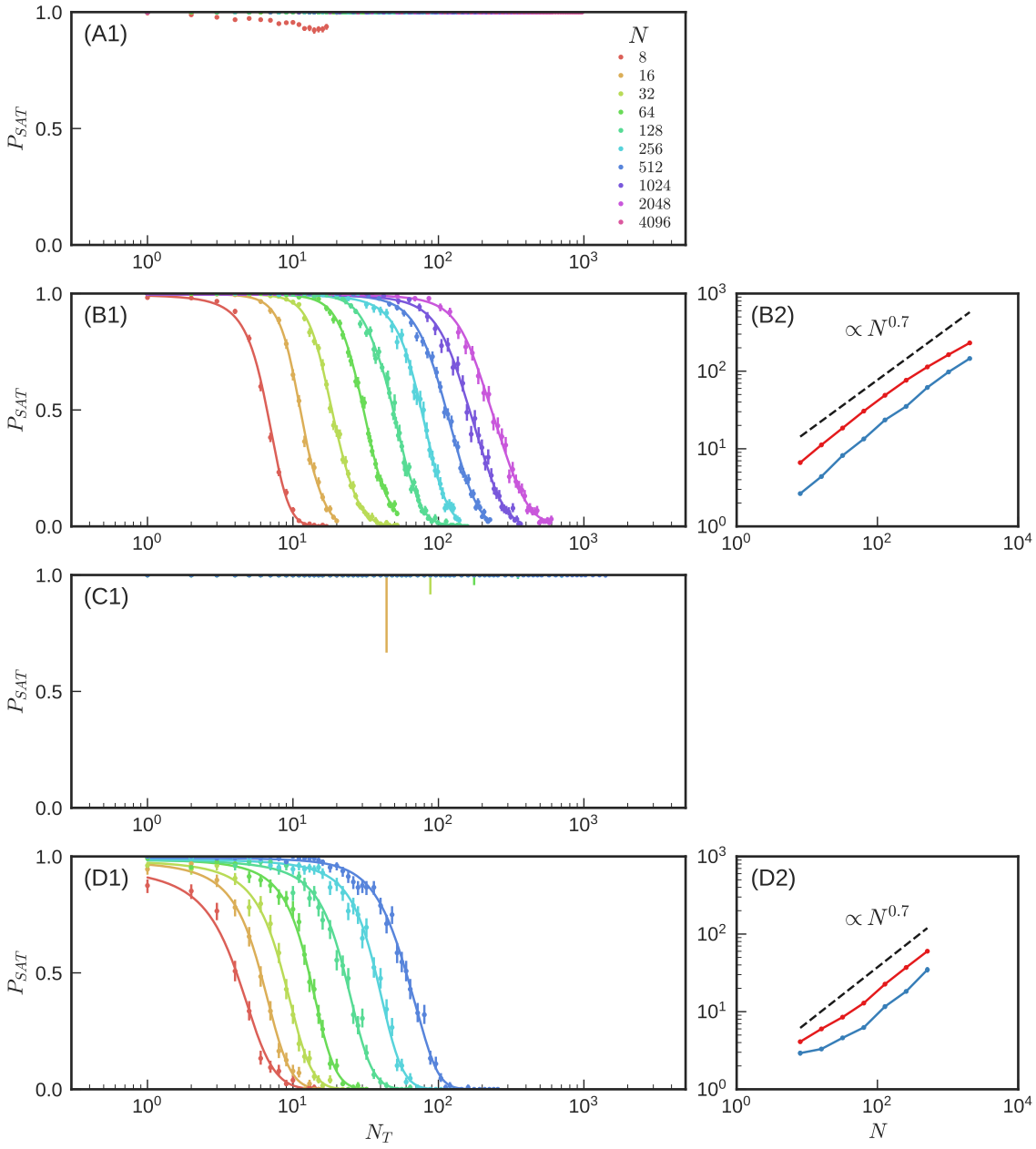

Figure 3.10: Satisfaction probability and scaling of the transition position and width for flow networks tuned for target current with (A) $\Delta = 0.1$ and $\Delta = 1.0$ and mechanical networks tuned for target tension with (C) $\Delta = 0.1$ and (D) $\Delta = 10.0$. See Table 3.1 for more details. Large error bars reflect a lack of available networks with enough edges to measure P_{SAT} for large N_T.

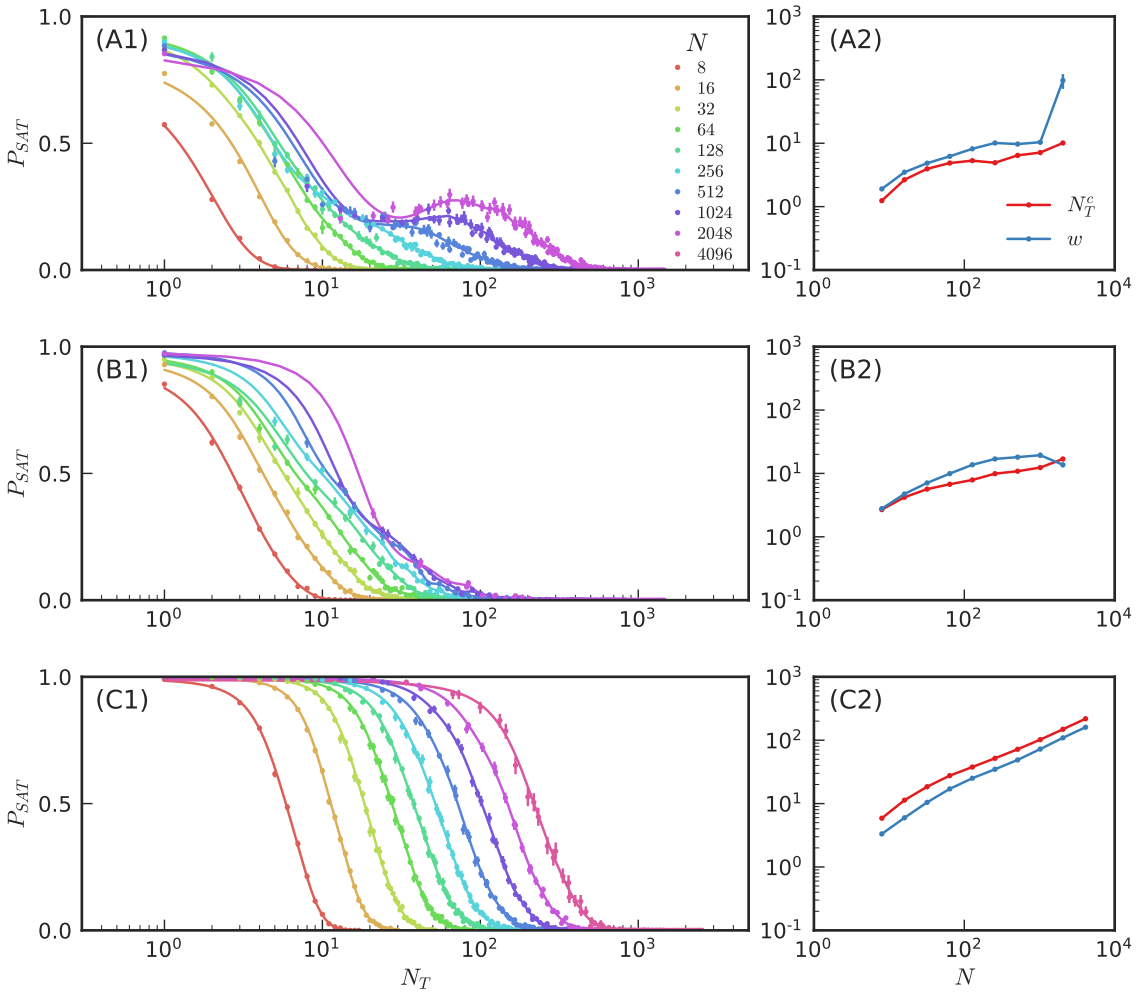

Figure 3.11: Satisfaction probability and scaling of the transition position and width for flow networks tuned for a negative relative change in target response of (A) $\Delta = -0.5$, (B) $\Delta = -1.0$, and (C) $\Delta = -1.5$. See Table 3.1 for more details.

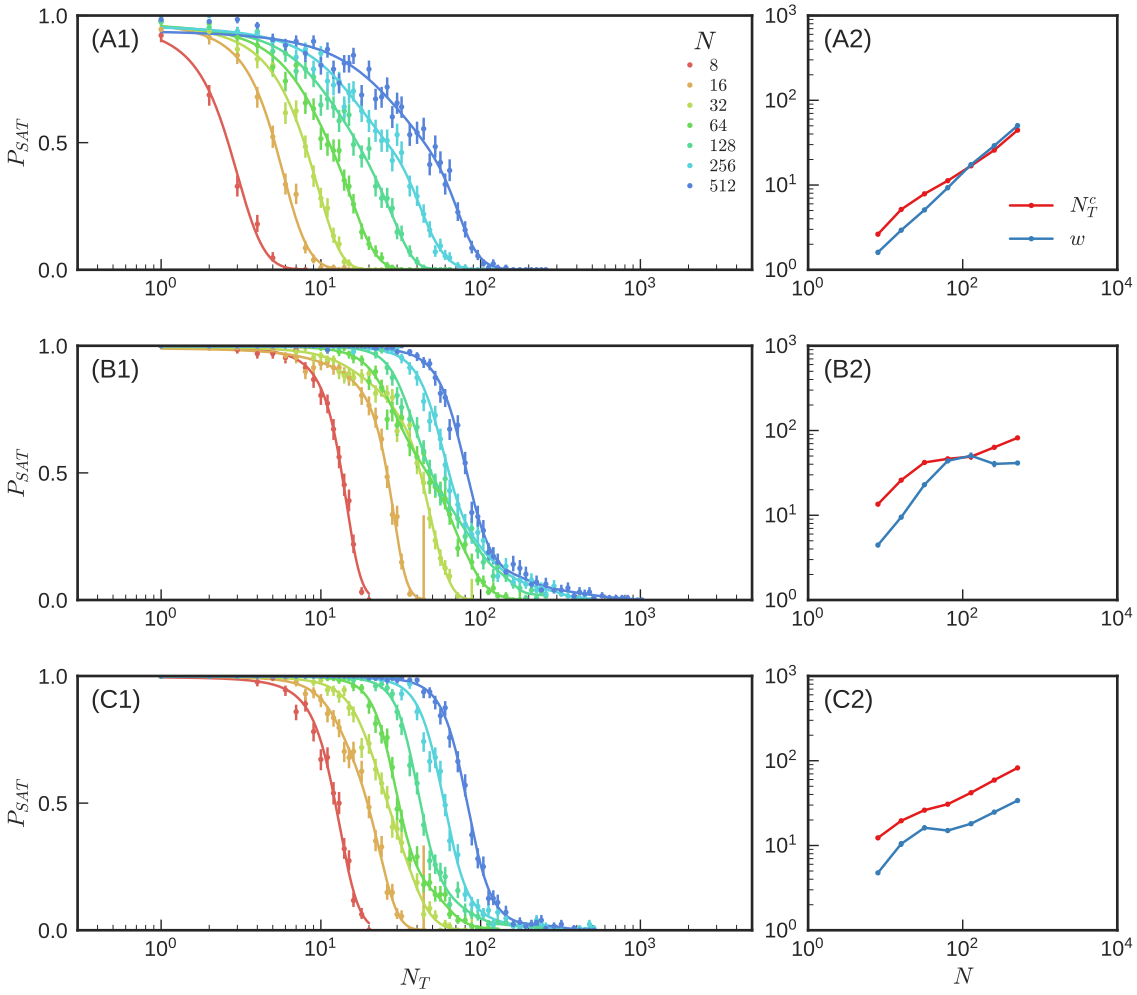

Figure 3.12: Satisfaction probability and scaling of the transition position and width for mechanical networks tuned for a negative relative change in target response of (A) $\Delta = -0.5$, (B) $\Delta = -1.0$, and (C) $\Delta = -1.5$. See Table 3.1 for more details. Large error bars reflect a lack of available networks with enough edges to measure P_{SAT} for large N_T.

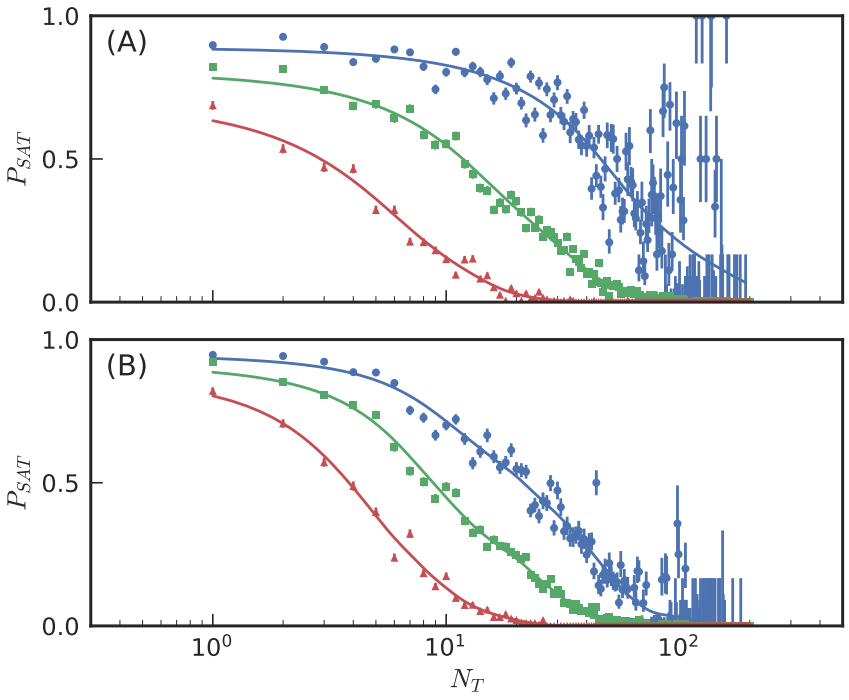

Figure 3.13: Satisfaction probability of flow networks derived from real UK railroad networks with (A) an edge source and (B) a node pair source. Three cases are shown for each source: (blue curves with circular symbols) The entire network is used. (green curves with square symbols) All bridge edges are removed and only the largest connected component is used. (red curves with triangular symbols) The largest connected component is used and edges whose pressure differences will always be zero are excluded from being chosen as targets. See Section 3.6.1 for more details.

3.6.2 Transition power law fitting and deviations

Fig. 3.14 demonstrates the deviations from power laws for the four systems displayed in Fig. 3.2. We have plotted the fractional difference of each measured point, N_T^c or w, from its fitted power law function $f(N)$ and $g(N)$, respectively, as a function of system size N. In both cases our fitted function is of the form AN^α where A and α are our fit parameters. Both the data sets for N_T^c and w are fit simultaneously with the same power α, but different coefficients A, resulting in a total of three fit parameters. Error bars have been estimated by dividing the uncertainty in N_T^c or w by the respective fit function at that point. It is apparent that the simple power law form does not perfectly match the underlying data.

3.6.3 Satisfaction probability error bars

Each data point of the various satisfaction probability plots is representative of a binomial distribution

$$p_i \sim \text{Binomial}(n_i, \hat{p}_i) \tag{3.6.2}$$

where n_i is the number samples and $\hat{p}_i$ is the fraction of successful tuning attempts. To calculate the error bars depicted in the various satisfaction probability plots, we

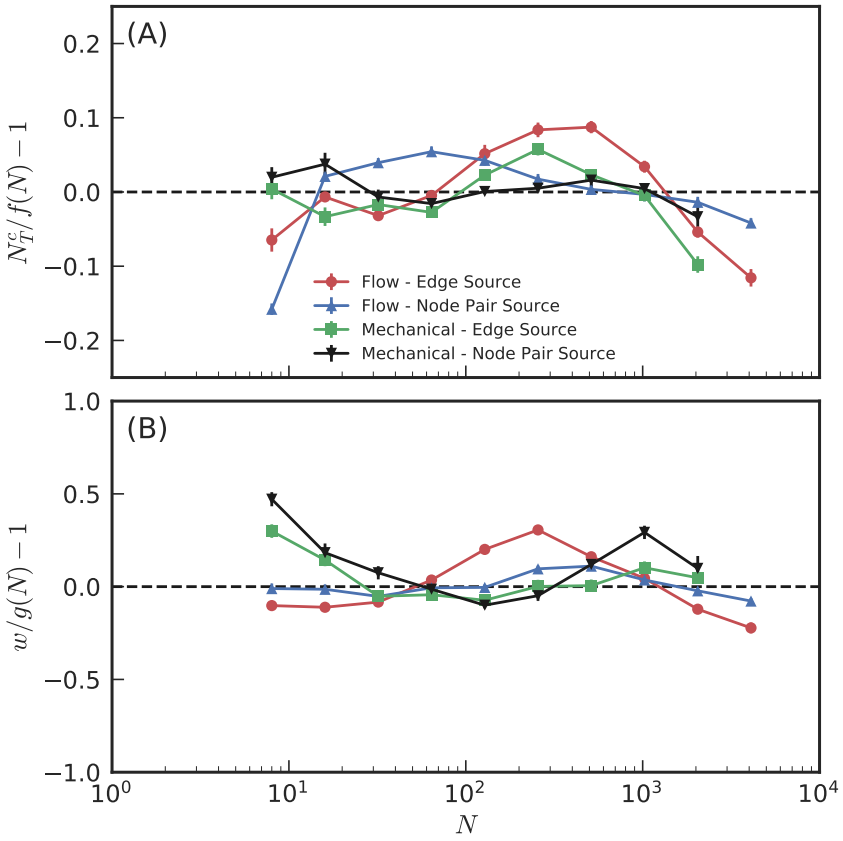

Figure 3.14: Deviations of the power laws in Fig. 3 of the main text from power laws of the form $f(N) = AN^{\alpha}$ for the transition position and $g(N) = BN^{\alpha}$ for the transition width. Error bars for the position and width have been rescaled by dividing by $f(N)$ or $g(N)$, respectively.

use the Wilson score interval [80]

$$p_i^{\pm} = \frac{1}{1+\frac{1}{n_i}z^2}\left[\hat{p}_i + \frac{1}{2n_i}z^2 \pm z\sqrt{\frac{1}{n_i}\hat{p}_i(1-\hat{p}_i) + \frac{1}{4n_i^2}z^2}\right] \tag{3.6.3}$$

with a z-score of $z = 1$. This gives us an estimate of the uncertainty for each data point which is analogous to the standard deviation for a Gaussian distribution. However, since the probability is restricted between zero and one, the error bars are not necessarily symmetric.

3.6.4 Satisfaction probability curve fitting

The satisfaction probability curves depicted in Fig. 3.2, along with many of the supplemental figures, were estimated using smoothing splines constructed from a basis of cubic B-splines. The procedure for constructing the splines and estimating the smoothing parameter were drawn with some modification from Ref. [78, Chapter 9.2].

To generate an estimate of a satisfaction probability curve, we start with a set of n satisfaction probabilities y_i each generated for a corresponding number of targets x_i where i goes from 1 to n. Each satisfaction probability counts the fraction of successfully tuned networks from a collection of n_i samples. Our goal is to find a function $p(x)$ which approximates the underlying function sampled by the data. Since we do not know what functional form we should use, we would like to approximate this function using a spline. However, the function $p(x)$ should be limited to the interval $[0, 1]$, while splines are not typically limited in this way. Therefore, we write $p(x)$ in terms of a more general function as

$$p(x) = \frac{e^{S(x)}}{1 + e^{S(x)}} \tag{3.6.4}$$

where $S(x)$ is the spline function which can take on any real value.

B-spline approximation

In terms of B-splines, the approximating spline function $S(x)$ is written

$$S(x) = \sum_{i=1}^{m} c_i B_i^k(x) \tag{3.6.5}$$

with m coefficients c_i and degree-k basis splines $B_i^k(x)$. The coefficients are the fit parameters we would like to estimate.

We must address the specific choices made in the use of B-splines. First, we choose to use cubic splines ($k = 3$). One knot is chosen for each data point plus an extra k at the lowest and highest values of x for padding. This gives us a total of $m = n + 2k$ knots,

$$t_i = \begin{cases} x_1 & \text{if} \quad 0 < i \leq k \\ x_{i-k} & \text{if} \quad k < i \leq n + k \\ x_n & \text{if} \quad n + k < i < n + 2k \end{cases} \tag{3.6.6}$$

The result is $m = n + 2k - (k + 1)$ basis splines with corresponding coefficients.

B-spline coefficient estimation

Typically, one would employ a least squares approach to calculate the spline coefficients. However, this assumes that each data point is drawn from some normal distribution, while we know in this case they are drawn from a set of binomial distri-

butions

$$y_i \sim \text{Binomial}(n_i, p(x_i)) \tag{3.6.7}$$

Carrying out a standard maximum likelihood estimation, the corresponding log-likelihood of the binomially distributed data is

$$\mathcal{L}(y) = \frac{1}{n}\sum_{i=1}^{n} n_i[y_i \log p(x_i) + (1-y_i)\log(1-p(x_i))] \tag{3.6.8}$$

In terms of $S(x)$, the log-likelihood can be written

$$\mathcal{L}(y) = \frac{1}{n}\sum_{i=1}^{n} [b(x_i) - y_i S(x_i)] \tag{3.6.9}$$

up to a constant with

$$b(x_i) = n_i \log\left(1 + e^{S(x_i)}\right) \tag{3.6.10}$$

To implement smoothing, we introduce a term with penalty parameter λ which penalizes the square of the curvature of $S(x)$. This gives us the penalized generalized linear model

$$I_\lambda(c) = \frac{1}{n}\sum_{i=0}^{n-1} \left[n_i \log\left(1 + e^{S(x_i)}\right) - y_i S(x_i)\right] + \lambda \int_{x_0}^{x_{n-1}} dx[S''(x)]^2 \tag{3.6.11}$$

Smoothing parameter

Next we must choose a good value for λ. This is accomplished using a generalized cross-validation (GCV) approach, allowing us to choose λ in an agnostic manner. Using GCV effectively chooses λ so that the approximating spline curve changes as little as possible if an arbitrary subset of data is left out of the fit. For the sake of convenience, we write

$$S(x) = \langle c|B^k(x)\rangle \tag{3.6.12}$$

where $c_i = \langle i|c\rangle$ and $B_i^k(x) = \langle i|B^k(x)\rangle$ are vectors of size m. We also write

$$\Sigma_{ij} = \int_{x_0}^{x_{n-1}} dx B_i^k(x) B_j^k(x) \tag{3.6.13}$$

Finally, we minimize the generalized cross-validation function

$$V(\lambda)_{GCV} = \frac{\sum_{i=1}^{n} \left[D_i^{-\frac{1}{2}}(y_i - \mu_i)\right]^2}{\frac{1}{n}\,\mathrm{tr}^2(I - A)} \tag{3.6.14}$$

with

$$\mu_i = b'(S(x_i)) \tag{3.6.15}$$

$$D_i = b''(S(x_i)) \tag{3.6.16}$$

and

$$A_{ij} = D_i^{\frac{1}{2}} \langle B^k(x_i)| \left[\sum_{l=1}^{n} D_l \, |B^k(x_l)\rangle\langle B^k(x_l)| + 2\lambda\Sigma \right]^{-1} |B^k(x_j)\rangle \, D_j^{\frac{1}{2}} \tag{3.6.17}$$

The size $n \times n$ matrix I is the identity. When testing a particular value of λ, the values c_i are always chosen to minimize (3.6.11) for that λ. Therefore, the spline coefficients are treated as a function of λ.

When minimizing (3.6.14), there may sometimes be extraneous minima at $\lambda = 0$ or $\lambda = \infty$. Since we would like some degree of smoothing, we never choose the minimum at zero. Also, moderate smoothing is generally preferable to infinite smoothing, so if a local minimum exists for finite λ, it is chosen even if it is not the global minimum.

3.6.5 Transition measurements

We use the spline approximations of each satisfaction probability curve in order to estimate the positions and widths of each satisfiability transition. The center of the transition is simply chosen as the number of targets N_T^c such that the probability of success is exactly 50%, $P_{SAT}(N_T^c) = 0.5$. The width of the transition w is found by first finding the number of targets corresponding to success rates of 25% and 75% and taking their differences, $w = P_{SAT}^{-1}(0.75) - P_{SAT}^{-1}(0.25)$. In order to weight each point correctly when finding the power law scaling of the transition properties, we utilized Monte Carlo resampling to estimate uncertainty [56]. To find the uncertainty values

for N_T^c and w for a particular curve, each data point for that curve is resampled from its underlying binomial distribution. The spline approximation is then recalculated for this new set of data points and new values of N_T^c and w are extracted. This process is repeated numerous times, resulting in a distribution of value of N_T^c and w. The uncertainty is then calculated by finding the standard deviation of of these distributions.

Chapter 4

The topological basis of function in flow networks

Note: The following content is reproduced with major revision from Ref. [63].

4.1 Introduction

Many biological fluid transport networks are optimized to redirect flow as dictated by the needs of the system. The cerebral vasculature provides the most striking example: by dynamically contracting and dilating blood vessels, the brain is able to actively control the propagation of blood in order to support local neuronal activity [29, 26]. More generally, the ability to locally tune the link (edge) conductances of venation networks enable animals [77], plants [55, 66], fungi [33], and slime molds [74] to control the spatial distribution of water, nutrients, oxygen, or metabolic byproducts.

Flow networks have been shown to be remarkably tunable with the ability to support highly complex, multifunctional tasks. By adding or removing a small number of edges from a network, the pressure differences of a large number of edges can be tuned simultaneously to respond in a predetermined way to a pressure difference applied elsewhere in the network [62].

While venation networks between individuals within a species – and sometimes between related species – often share common macro- and meso-scale network architectures, micro-scale network structures can often seem random with no known underlying geometric organizational principle [32]. This gives raise to a fundamental question: What is the means by which a flow network performs a given task? In other words, what is the relationship between structure and function?

Here we use persistent homology to identify the underlying basis of function in flow networks tuned to perform specific tasks. By modifying the edge conductances of a network, we tune the pressure difference of a single "target" edge to respond by a specified amount when a unit pressure difference is applied to a separate, predetermined pair of "source" nodes. We find that the structure-function relationship is topologically encoded in the response: as a network is tuned to achieve a desired target pressure difference, it separates into two sectors of relatively uniform pressure, even though the underlying network architecture remains a single connected component.

While this description is simple, it provides a unifying topological description for

all networks tuned for the same function, regardless of the underlying network architecture, along with a quantitative means to compare networks tuned for different functions. We demonstrate that it is robust even when the magnitude of the tuned response is small, and is also easily extended to analyze complex, multifunctional responses. The general approach we develop here could serve as the basis for studying the structure-function relationship for a wide variety of complex networks.

4.2 Design of Functional Flow Networks

We consider flow networks in which edges between nodes represent linear resistors. In this framework, the response of a network to external stimuli is governed by a discrete version of Laplace's equation equivalent to Kirchoff's equations. We derive our flow networks from randomly-generated two-dimensional configurations of soft spheres with periodic boundary conditions, created using standard jamming algorithms. Flow networks are extracted from these configurations by placing nodes at the centers of each sphere and edges – with associated fluid conductances (inverse resistance) – between nodes corresponding to spheres that overlap. We chose this ensemble because it provides initial networks that are reminiscent of those seen in biological. At small length-scales, many natural flow networks are disordered [32], have high numbers of closed loops [38], and are highly interconnected [5].

We tune our flow networks to perform simple functions: when a unit pressure dif-

ference is applied between a pair of source nodes, the pressure difference of a single target edge responds by at least an amount Δ (chosen to be non-negative). For each network the source nodes and target edge are chosen at random. Before tuning, the values of the edge conductances of each network are chosen randomly from the range 0.01 to 1.0 in discrete increments of 0.01. To achieve the desired target pressure difference of at least Δ across the target edge, we use a greedy algorithm: in each step we increase or decrease the conductance of a single edge by 0.01 (staying within the range 0 to 1, inclusively), modifying the edge conductance that best optimizes the response at that step (for further details, see the Appendix, along with Ref. [62] and similar work on mechanical networks in Ref. [61]).

Although we design our networks to perform elementary functions, the discrepancy between structure and function is readily apparent. Figs. 4.1(A) and (B) show examples of two different networks that have been tuned to perform the same function, namely to have similar relative positions of the source and target and the same target pressure difference of $\Delta = 0.2$ relative to the source. Clearly, the spatial distributions of edge conductances and pressures in the networks are noticeably different; it is unclear whether the underlying architectures of the two networks share anything in common. In contrast, Figs. 4.1(C) and (D) show examples of the same initial network tuned to before different functions. Both the relative positions of the source and target are different, along with the target pressure differences of $\Delta = 0.05$ and 0.5, respectively, which differ by an order of magnitude. Although the two network structures are identical before tuning and even share much in common afterwards,

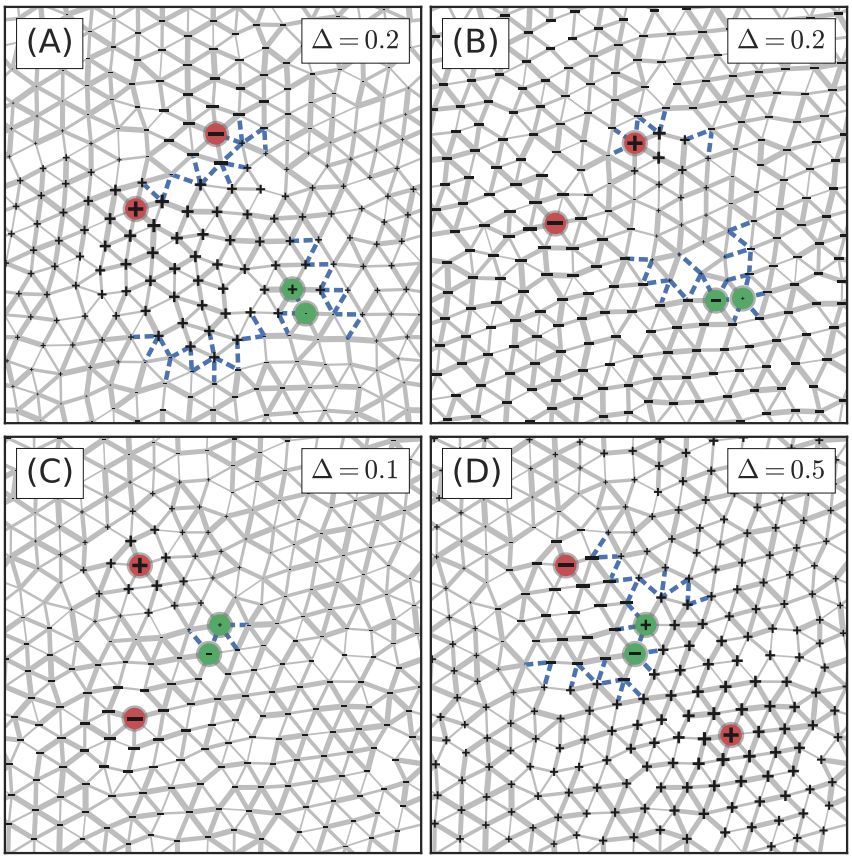

Figure 4.1: Four examples of tuned flow networks. In all examples, when a unit pressure difference is applied across the source nodes (shown in red), a single target composed of a pair of nodes (shown in green) responds with a pressure difference of Δ. The pressures on the nodes are shown in black where the symbol denotes the sign of the pressure and the size denotes the magnitude. The thickness of the edges corresponds to the conductance. Edges that are shown as thick dashed blue lines have been entirely removed (set to zero conductance) in the process of tuning. (A) and (B): Comparison of two flow networks with different initial structures tuned to perform the same function. The relative positions of the source and target are similar and the target is tuned to respond with a pressure difference of $\Delta = 0.2$. (B) and (C): Comparison of two networks with the same untuned structure tuned to perform different functions. The relative positions of the source and target are different and the tuned pressure differences differ by an order of magnitude with values of $\Delta = 0.05$ and $\Delta = 0.5$, respectively.

the networks are able to perform very different tasks.

4.3 Maximum Tuning Limit ($\Delta = 1$)

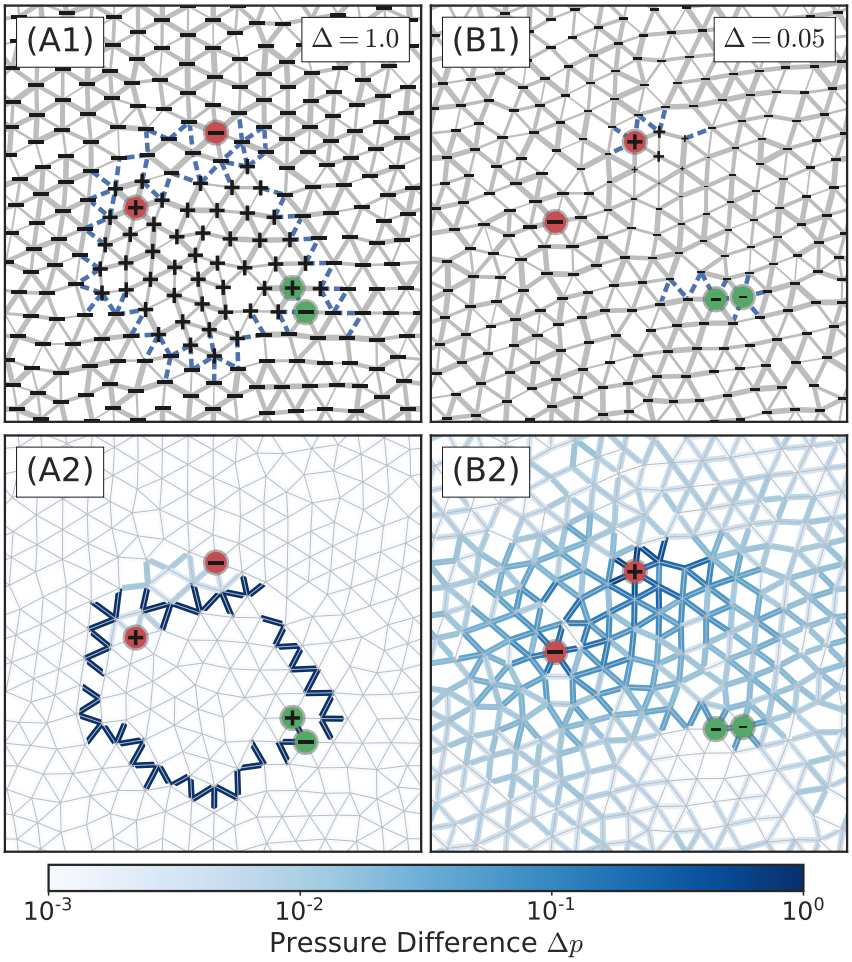

Figure 4.2: The same flow network tuned to show a pressure difference of (A) $\Delta = 1.0$ and (B) $\Delta = 0.05$. The source nodes are shown in red, while the target nodes are shown in green. (A1) and (B1): The pressures on the nodes are shown in black where the symbol denotes the sign of the pressure and the size denotes the magnitude. The thickness of the edges corresponds to the conductance. Edges that are shown as thick dashed blue lines have been removed in the process of tuning. (A2) and (B2): The absolute values of the pressure differences on the edges of the tuned networks in (A1) and (B1) shown in shades of blue. In the $\Delta = 1.0$ limit, the network clearly splits into two components of uniform node pressure, separated by a boundary of pressure difference equal to one. For smaller Δ, the network structure is not as clearly delineated.

It is illuminating to first examine the extreme limit where $\Delta = 1$, the maximum achievable pressure difference at the target edge (see Figs. 4.2(A1) and (A2)). Here the

network clearly separates into two distinct sectors of perfectly uniform node pressure, connected only by a small region between the source nodes. These two regions are separated by a crack-like structure with pressure differences of precisely 1.0 along edges that have been removed during the tuning process. The structural changes in the network architecture are purely topological: all edges connecting the two sectors are removed (excluding those connecting the source nodes, which could be removed with no change in the response), increasing the number of connected components in the network from one to two. The exact details of the local structure (which specific edges are modified) do not matter as long as this partitioning takes place. In this extreme case, the relationship between structure and function is clear: the presence of the two separate connected components, each associated with one source node and one target node, allows the desired target pressure difference to be achieved. Intuitively, this description should extend to all networks tuned to this same extreme limit, since adding any extra links between the two sectors would allow current to flow between them and necessarily decrease the pressure difference. However, when Δ is less than 1, as in Fig. 4.1(B1) and (B2), the entire network is highly connected and the important aspects of the structure are not as well-defined.

Here we show that a persistent homology analysis of the response of such networks allows us to generalize the sector description observed in the extreme $\Delta = 1.0$ case to smaller pressure differences. The analysis is able to identify two analogous sectors, even in cases such as Fig. 4.1(B1) where the target pressure difference of $\Delta = 0.05$ is too small for the components to be discerned by eye and the underlying the network

architecture is still composed of a single connected component. Consequently, this process allows us to relate the structures of different networks tuned to perform the same function.

4.4 Topological Signature of Tuning

At its core, the process of tuning networks is local; it involves modifying the conductances of individual edges. However, the extreme example of Fig. 4.2(A1) provides evidence that coordinated, large-scale topological changes in the structure and response can arise from local edge tuning. To see if remnants of these topological changes are responsible for function when $\Delta < 1$, we use persistent homology, a technique that can detect and assign significance to the topological features of geometrically and/or topologically structured data [17, 52]. In this case, our data consists of the pressure response of tuned networks, along with the connectivities of the nodes and edges. In general, the types of topological features the persistence algorithm can detect include connected components, loops, voids, etc; for flow networks, only the first two are relevant. Since the extreme case for $\Delta = 1$ suggests that the network partitions into different sectors, we focus solely on connected components. In the past, the persistence algorithm (or related techniques) has been used to study various topological aspects of flow networks [38, 45], along with their higher-dimensional analogs, mechanical networks [40, 41].

To apply the persistence algorithm, one needs an ordering of the network elements (vertices, edges) in terms of a quantity defined on the particular elements that are relevant to the tuned function. An obvious candidate is the pressures on the nodes. However, since the node pressures obey a discrete version of Laplace's equation, local minima and maxima in the node pressures can only occur at the source. As a result, there can only be a single (global) minimum on one of the source nodes, and a single (global) maximum at the other source node. Since local extrema play an important role in defining topological features, their absence means that very few interesting features would be detected by the persistence algorithm (in fact, we would only detect a single connected component corresponding to the two global extrema at the source nodes). We therefore define our ordering on the edges instead of the nodes, sorting each edge according to the absolute value of the difference in pressure between its nodes. Given a network with N_E edges, we label each edge with an integer i according to this order, with $1 \leq i \leq N_E$, as illustrated in Fig. 4.3(A), and denote its corresponding pressure difference as Δp_i.

We then proceed as follows: starting with an empty network with no edges, we add each edge to the network in order of its pressure difference, one at a time. With each step i, we obtain a larger subset of our original network, consisting of the first i edges. This sequence of subnetworks corresponds to a filtration of the pressure differences on our original network. In the "ascending filtration," we perform this process for each edge in order of the absolute value of the pressure differences from smallest to largest. Similarly, for the "descending filtration" we proceed in order of decreasing

pressure difference.

At each step in the filtration, the persistence algorithm records any changes in the topological structure, *i.e.* any changes in the number of connected components. When an edge is added, there are three possibilities: (i) the new edge is not connected to any of the pre-existing edges, increasing the number of connected components by one, (ii) the new edge is shared between two of the pre-existing components, joining them together and decreasing the number of connected components by one, or (iii) the new edge is only connected to a single pre-existing component, incurring no change in the number of connected components. For the first case, in which a new component appears, we say that it is "born" and record the pressure difference at that step, Δp_b, as its "birth pressure difference." The new edge is the "birth edge." In the second case, in which two components merge, we say that the component in the pair that was born most recently has "died," and we record the pressure difference, Δp_d, as its "death pressure difference." The new edge is the "death edge." In this way, each connected component that appears during the filtration is assigned a birth-death pair $(\Delta p_b, \Delta p_d)$. By carrying out the filtration in both ascending and descending order, we collect two sets of birth-death pairs, one for each filtration (The approach we have described here has been simplified for the sake of discussion, but is a sufficient version of the persistence algorithm. See the Appendix and Ref. [17] for a detailed explanation of the complete algorithm).

Figs. 4.3(B)-(F) illustrate this process for an example network. New components are born in Figs. 4.3(B), (C), and (D), colored green, orange, and blue, respectively, with

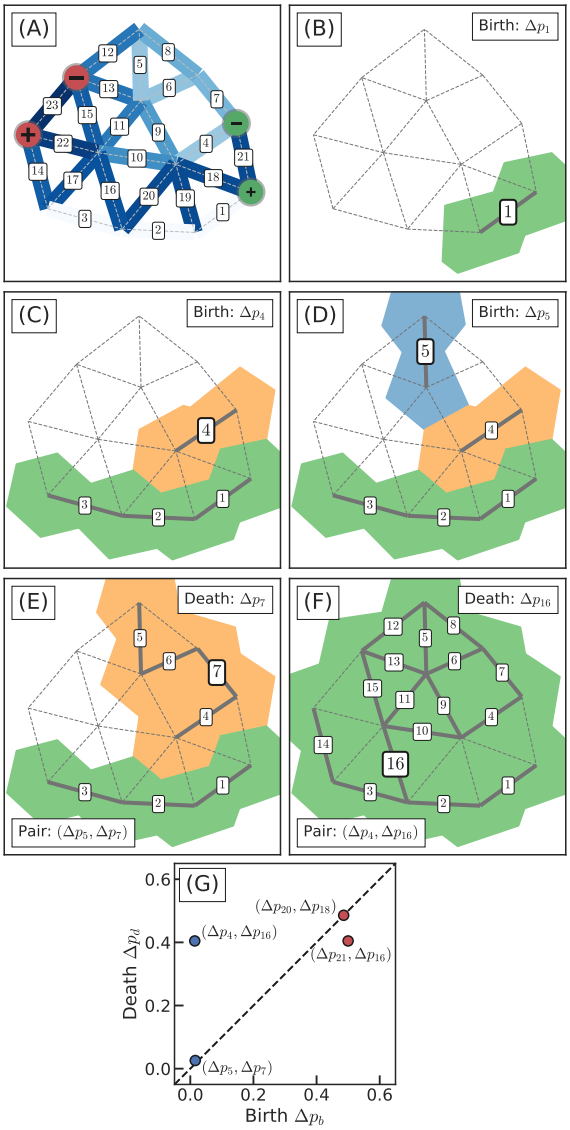

Figure 4.3: Example of the persistence algorithm carried out on a toy flow network tuned for a pressure difference of $\Delta = 0.5$. (A) Ordering indices of the edges from smallest to largest pressure difference, defining the ascending filtration. (B) - (D) Birth of three components at pressure differences Δp_1, Δp_4 and Δp_5 colored green, orange and blue, respectively. (E)-(F) Deaths of the blue and orange components at pressure differences Δp_7 and Δp_{16}, respectively. (G) The resulting persistence pairs of the ascending filtration (blue) and descending filtration (red, algorithm not shown) plotted on a persistence diagram. Points farther from the diagonal signify more important features.

corresponding birth pressures of Δp_1, Δp_4, and Δp_5. Figs. 4.3(E) and (F) show the deaths of two of the components. In Fig. 4.3(E), the blue component dies with a death

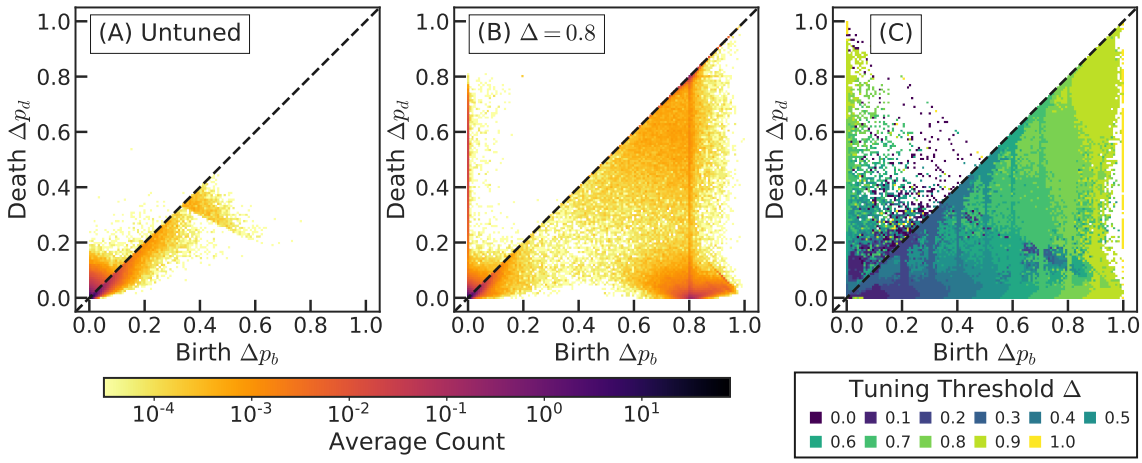

Figure 4.4: Average persistence diagram of (A) untuned flow networks and (B) networks tuned to a pressure difference of $\Delta = 0.8$. Each bin is colored according to the average number of points found in that bin in the persistence diagrams for over 30000 flow networks of 256 nodes. Points located above the diagonal correspond to the ascending filtration, while those located below the diagonal correspond to the descending filtration. Features for which the birth and death pressure differences are exactly equal are excluded from all persistence diagrams due to negligible topological significance (persistence $\tau = 0$).(C) Evolution of the average persistence diagram with tuning. The average persistence diagram is calculated for 11 values of target pressures Δ ranging from 0 to 1 in steps of 0.1. Each bin is colored according to the value of Δ whose average persistence diagram has the largest number points in that bin.

pressure of Δp_7, resulting in the birth-death pair $(\Delta p_5, \Delta p_7)$, while in Fig. 4.3(F), the orange component dies with death pressure Δp_{16}, resulting in the birth-death pair $(\Delta p_4, \Delta p_{16})$. The final component, consisting of the entire network, never dies, so we do not assign it a birth-death pair.

Once we have collected all birth-death pairs, $(\Delta p_b, \Delta p_d)$, we can construct a persistence diagram as depicted in Fig. 4.3(G). For the ascending filtration, the death pressure difference exceeds the birth pressure difference in each pair; these pairs are represented by points colored in blue. For the descending filtration, the death pressure difference is always smaller than the birth pressure difference in each pair; these pairs

are represented by points colored in red. The complete set of points characterizes the topological structure of connected components in the network. Points associated with the ascending/descending filtration represent regions of the network with relatively low/high pressure differences.

Additionally, the vertical distance of a point from the black diagonal line in Fig.4.3(G), along which $\Delta p_b = \Delta p_d$, is called the "persistence": $\tau = |\Delta p_d - \Delta p_b|$. This measures the lifetime of a feature during the filtration process, and provides a measure of its significance. Small fluctuations in pressure differences, for example, would yield birth-death pairs with low persistence. In the example of Fig. 4.3, we see that the point $(\Delta p_4, \Delta p_{16})$ has a large persistence value. This means that the corresponding orange connected component survives, or persists, for a large range of pressure differences during the persistence algorithm. This high persistence suggests that this feature is important for characterizing the structure of the network.

We have carried out the persistence analysis for ensembles of tuned and untuned networks and collected the results for each ensemble into a persistence diagram. Fig. 4.4(A) depicts a two-dimensional histogram of the average persistence diagram of over 30000 untuned networks, each composed of 256 nodes. For each network, the source and target edges are selected randomly. The histogram is calculated by dividing the persistence diagram into bins in Δp_b and Δp_d (shown as individual pixels) and counting the average number of points (birth-death pairs) that fall within each bin across all of the networks in the ensemble. We exclude any points for which τ is exactly zero, as these features can be interpreted as having no topological signif-

icance. We observe two different clusters of features for untuned networks, both of which correspond to fluctuations in the response due to the discrete nature of the initial networks. The the features clustered near the origin are typically located far from the target edge where the pressure difference scale is relatively low. The band of features below the diagonal at birth pressure differences between about $\Delta p_b = 0.35$ and 0.6 typically correspond to small numbers of isolated edges of relatively high pressure differences located near the source. In the continuum limit of Laplace's equation with infinite system size, both sets of features would collapse towards a single point at the origin.

Fig. 4.4(B) shows the equivalent histogram for an ensemble of networks tuned to a target pressure of $\Delta = 0.8$. A comparison of Figs. 4.4(A) and (B) shows that the histogram of the persistence diagrams changes drastically in two ways. First, a high concentration of features appears in the ascending diagram, located above the diagonal, concentrated in a thin vertical band at a birth pressure of $\Delta p_b = 0$, with death pressures ranging from zero to our tuned response of $\Delta = 0.8$. This indicates that tuned networks tend to develop regions of almost perfectly uniform node pressure (zero pressure difference), separated by boundaries of high pressure differences up to the tuned pressure difference. Most of these features are located far above the diagonal, indicating that they are of high significance. Similarly, for the descending diagram, a vertical band appears for the tuned networks that is absent for untuned networks. This band is concentrated at a birth pressure equal to our tuned response $\Delta = 0.8$ with a death pressure ranging from zero to 0.8. This band

corroborates our observations of the ascending filtration; it indicates that there are regions of pressure differences equal to our tuned response. These likely correspond to the boundaries between regions of uniform node pressures. Again, many of these features are of high significance because they are located far below the diagonal.

To understand how persistence diagrams evolve in more detail, we calculate the average persistence diagram for 11 target pressures ranging from $\Delta = 0.0$ to 1.0. For each bin we find the value of Δ whose average persistence diagram is most highly represented, with the largest average number of points in that bin compared to all Δ. We color each bin according to this representative value of Δ as shown in Fig.4.4(C). We see that as networks are tuned for larger and larger target pressures Δ, the average ascending persistence diagram is steadily populated with points far above the diagonal in a band at $\Delta p_b = 0$ ranging from $\Delta p_d = 0$ to Δ, while the average descending diagram develops features at the tuned target pressure, in bands located at $\Delta p_b = \Delta$. This confirms that the trends we see in Figs. 4.4(A1) to (A2) generalize to all values of Δ.

4.5 Topological Characterization

Now that we have identified persistent features that appear in the tuned network structures, namely the features in the vertical bands that appear at $\Delta p_b = 0$ in the ascending filtration and at $\Delta p_b = \Delta$ in the descending filtration, we associate these

features with their actual components in the tuned networks. The obvious approach would be simply to identify the connected components that define each point in the persistence diagrams at either their birth or directly before their death as shown in Fig. 4.3. However, components can merge multiple times, forming a binary tree of component mergers. This results in identified regions that overlap with one another, with each node belonging to a large set of different components. Instead, for simplicity we seek to divide the network into non-overlapping regions.

To accomplish this, we start by creating a skeletonized tree representation of our network, as shown in Fig. 4.5(A), which both encodes the topological changes we saw in our persistence algorithm and also allows us to uniquely divide our network in distinct components. To create this tree, we first perform the ascending filtration we defined in the previous section, keeping any edge which fits at least one of the following criteria: (i) the edge creates a new connected component (a birth edge), (ii) the edge merges two connected components (a death edge), or (iii) the edge adds a new vertex to the network. Alternatively, we could exclude any edge which creates a cycle during the filtration.

Next, we mark any edges that fit the second criterion with a dashed line. As these edges denote merging events in our filtration, they naturally separate our network into different components. Using these edges as the boundaries between regions in the skeletonized network, we partition the network into different connected components, shown as the green, orange and blue regions in Fig. 4.5(B). Each boundary edges we identify corresponds to a death event and can therefore be associated with a

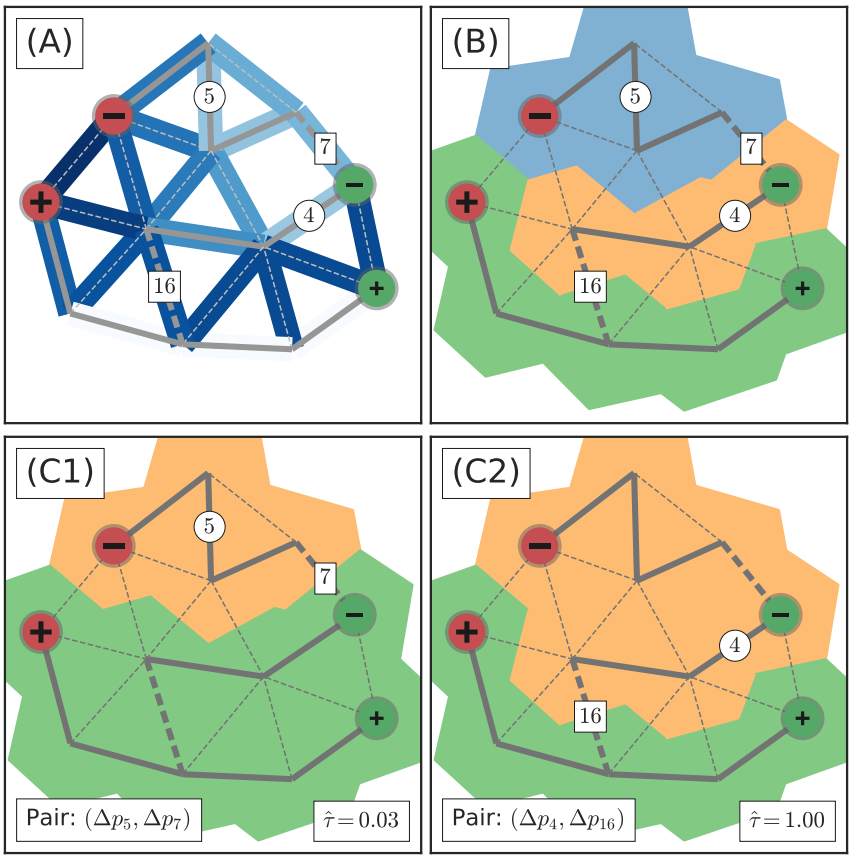

Figure 4.5: (A) Skeletonized tree of the tuned network structure shown as thick lines gray lines, with death edges shown as thick dashed lines overlayed on the absolute values of the pressure differences shown in shades of blue. This tree encodes the topology of the connected components of the network. The filtration index of birth and death edges are shown with circular and rectangular backgrounds, respectively. (B) Using the death edges as the boundaries of components, three components shown in green, orange and blue can be identified. (C1)-(C2) Each boundary (death) edge can be used to decompose the network into two unique sectors shown in green and orange. The birth-death pair associated with each boundary edge can be used to assign a normalized persistence value $\hat{t}$ to each possible pair of sectors. In (C1) $\hat{\tau} = 0.03$, while in (C2) $\hat{\tau} = 1.0$, the maximum possible value, indicating the greatest possible topological significance. The pair of sectors with the greatest value of $\hat{\tau}$ which places each target node into a separate region is chosen (in this case the sectors in (C2)).

particular birth-death pair found using the persistence algorithm. The corresponding birth edge is always the edge with minimum filtration index in one of the sectors. However, a death edge is not guaranteed to be located on the boundary of the sector

corresponding to its birth edge. In the example, the boundary edge connecting the orange and green sectors is associated with the pair $(\Delta p_4, \Delta p_{16})$, while the edge connecting the orange and blue sectors is associated with the pair $(\Delta p_5, \Delta p_7)$.

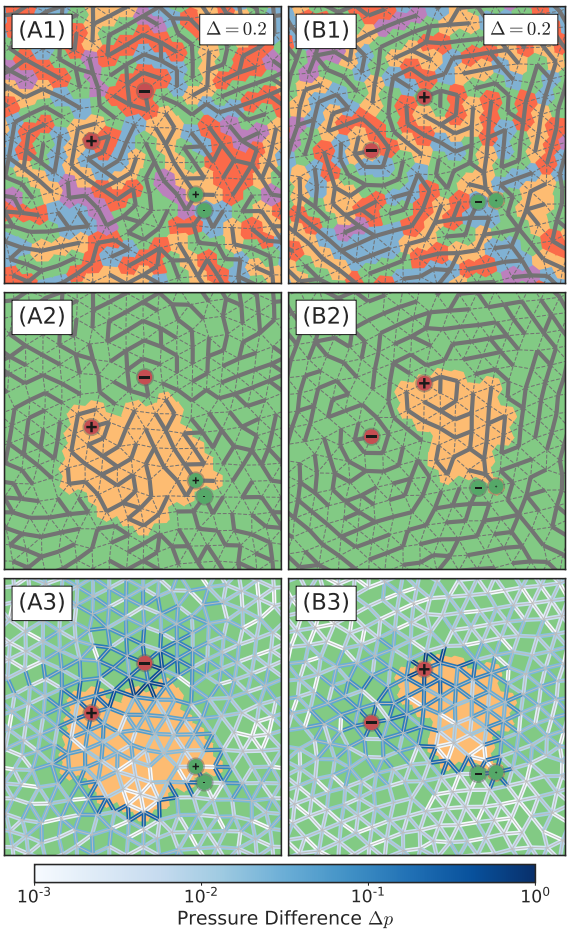

Figure 4.6: Comparison of the topological structure of the two flow networks from Fig. 4.1 with different structures tuned to perform the same function both before and after the simplification process. (A1) and (B1): Before simplification, each network shows a high degree of over-segmentation with its structure decomposing into a large number of connected components. Each component is colored arbitrarily such that no two neighbors have the same color. The skeletonized tree representing the topology of the connected components is shown with thick gray lines. Edges in the tree that overlap two separate regions correspond to boundary (death) edges. (A2) and (B2): After simplification, the number of connected components is greatly reduced. We identify the two main components of highest persistence (shown in green and orange), each associated with a single target node. (A3) and (B3): The correspondence between the resulting sectors and the pressure differences on the edges.

This process decomposing the network into sectors is analogous to the watershed transform often used in image segmentation [64]; each component we find is effectively a basin associated with a local minimum that corresponds to the component's birth edge. The main drawback to this method is that it results in rampant oversegmentation, as is often the case when performing watershed transforms on noisy data. Each of the large number of points in our persistence diagram results in a new segment, no matter how small its persistence value. Figs. 4.1(A1) and (B1) show all of the individual components corresponding to birth-death pairs for the two networks from Fig. 4.1, along with the underlying tree structure. Each component is colored arbitrarily in order to highlight individual regions. Clearly, the two networks are highly segmented, and the many individual connected components do not provide much structural intuition.

To remedy this, we draw insight from the extreme $\Delta = 1$ case and attempt to coarse-grain the network into the two most significant sectors. Since a tree by definition has no cycles, each boundary edge divides the network into exactly two sectors, as shown in Figs. 4.5(C1) and (C2). In order to choose which decomposition of the network is most relevant, we examine the value of the persistence τ for the birth-death pairs corresponding to each boundary edge. We normalize each value of τ by the maximum persistence value of all birth-death pairs for that network $\tau_{\max}$. We denote this normalized persistence $\hat{\tau} = \tau/\tau_{\max}$. This normalized persistence value ranges from zero to one, providing a measure of the topological significance of each possible pair of sectors. For example, the sectors in Fig. 4.5(C1) have a persistence of

only $\hat{\tau} = 0.03$, while those in Fig. 4.5(C2) have maximum possible value of $\hat{\tau} = 1.00$,.

Although a large value of $\hat{\tau}$ may indicate high significance, it does not guarantee relevance to the tuned response on its own. Therefore, we apply a physical criterion to choose the appropriate pair of sectors. Since we have tuned the network to have a certain pressure differential between the target nodes, we choose the boundary edge with the largest associated value of $\hat{\tau}$ which places each of the two target nodes into a different sector. In this way, we are able to uniquely decompose each of our tuned network structures into a pair of significant regions associated with each target node without choosing any arbitrary cutoffs. Furthermore, the value of $\hat{\tau}$ for the resulting sectors gives us a quantitative measure of the validity of our assumption that the two components corresponding to each target node are separate pressure sectors. If $\hat{\tau}$ is measured to be zero, then it is not possible to separate the network into two components in this way. But if $\hat{\tau}$ is equal to one, then the resulting sectors also correspond to the most topologically significant pair of connected components in the network.

Figs. 4.6(A2) and (B2) demonstrate the results of this procedure for the networks shown in Fig. 4.1. After coarse-graining via persistence, the topological structure of both networks has been greatly simplified compared to the initial components shown in Figs. 4.6(A1) and (B1), allowing us to identify two main regions (shown as green and orange), each associated with a single target node. Figs. 4.6(A3) and (B3) depict how the sectors correspond to the pressure differences on the edges of the networks. These regions allow us to directly compare the structures of the two networks that

have been tuned for the same function.

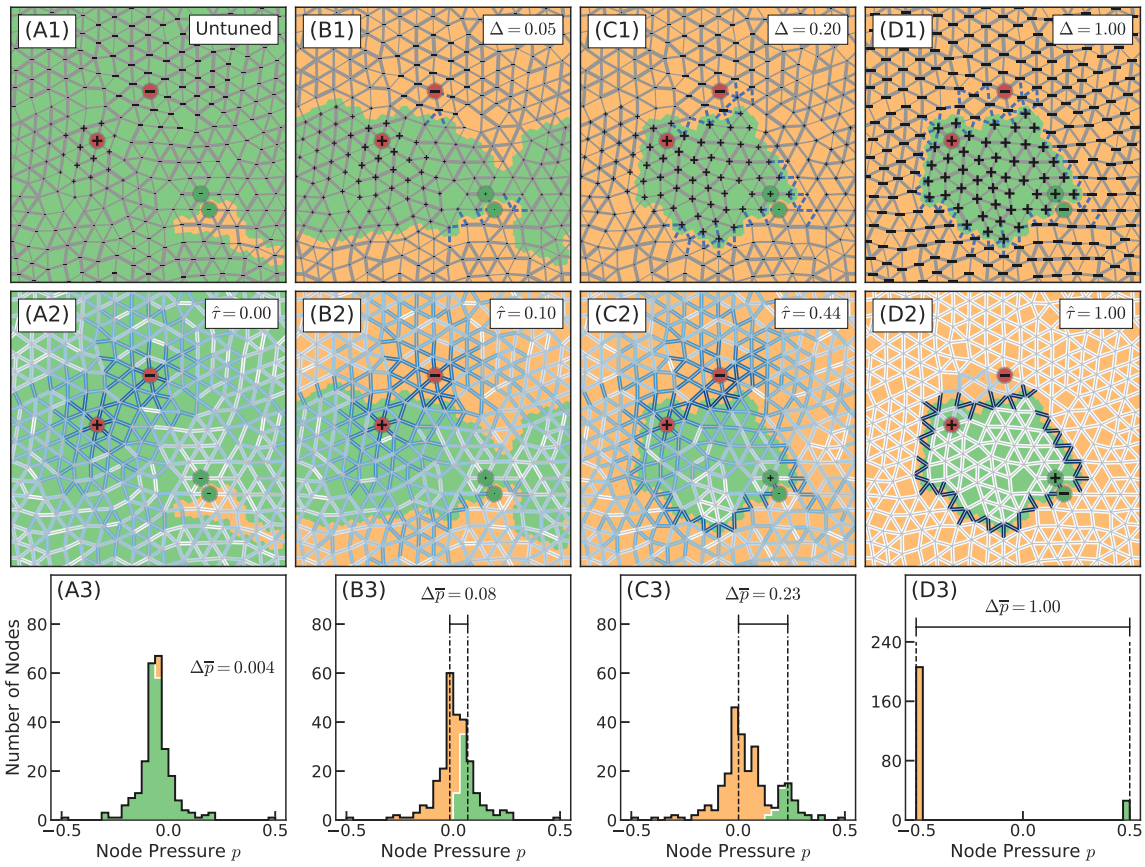

Figure 4.7: Evolution of the network structure and response with corresponding sector partitioning for (A) an untuned network and the same network tuned for target pressure differences of (B) $\Delta = 0.05$ (C) $\Delta = 0.2$, and (D) $\Delta = 1.0$. Each network is tuned directly from the same initial configuration in (A). (First Row) The simplified sectors characterizing the response are highlighted in green and orange. The source nodes are shown in red and the target nodes in green. The pressures on the nodes are shown in black where the symbol denotes the sign of the pressure and the size denotes the magnitude. The thickness of the edges corresponds to the conductance. Edges that are shown as thick dashed blue lines have been fully removed in the process of tuning. (Second Row) Correspondence of the sectors and the pressure differences on the edges. Edges are colored white-to-blue on a log-scale according to the absolute value of the pressure differences. (Third Row) The associated histogram of node pressures with green and orange portions showing the contributions of nodes in the green and orange sectors, respectively, shown in the first and second rows.

4.6 Structure-Function Relationship

Fig. 4.7 shows how the two sectors evolve with tuning. In Figs. 4.7(A1) and (A2), we see that before tuning, the sectors (highlighted as green and orange) do not have any obvious structural significance, with a small normalized persistence $\hat{\tau} = 0.04$. Fig. 4.7(A3) shows a histogram of the pressures on the nodes, highlighting the regions of the histogram associated with each sector. If we calculate the median node pressure for the nodes in the green region and separately for the nodes in the orange region, we can take the absolute value of the difference between the two median pressures, $\Delta\overline{p}$, as an effective pressure difference between the two regions. We find that the untuned network has a very small effective pressure difference of $\Delta\overline{p} = 0.001$.

After tuning to a target pressure of $\Delta = 0.05$, Figs. 4.7(B1) and (B2) show that the network response has more clearly segregated into two sectors bounded by a crack-like region of slightly larger pressure differences. These pressure differences are a result of edges that have been completely removed in that region. Examining the histogram in Fig. 4.7(B3), we see that the pressures of the nodes in the two sectors fall into different regions of the histogram with an effective pressure difference of $\Delta\overline{p} = 0.09$, relatively close to the tuned pressure difference. The persistence of the sectors is $\hat{\tau} = 0.10$, significantly larger than that of the untuned network.

Further tuning to a target pressure of $\Delta = 0.2$, we see in Figs. 4.7(C1) and (C2) that the two sectors partition the network even more clearly, even as the underlying network architecture remains connected as a single component. The areas of the

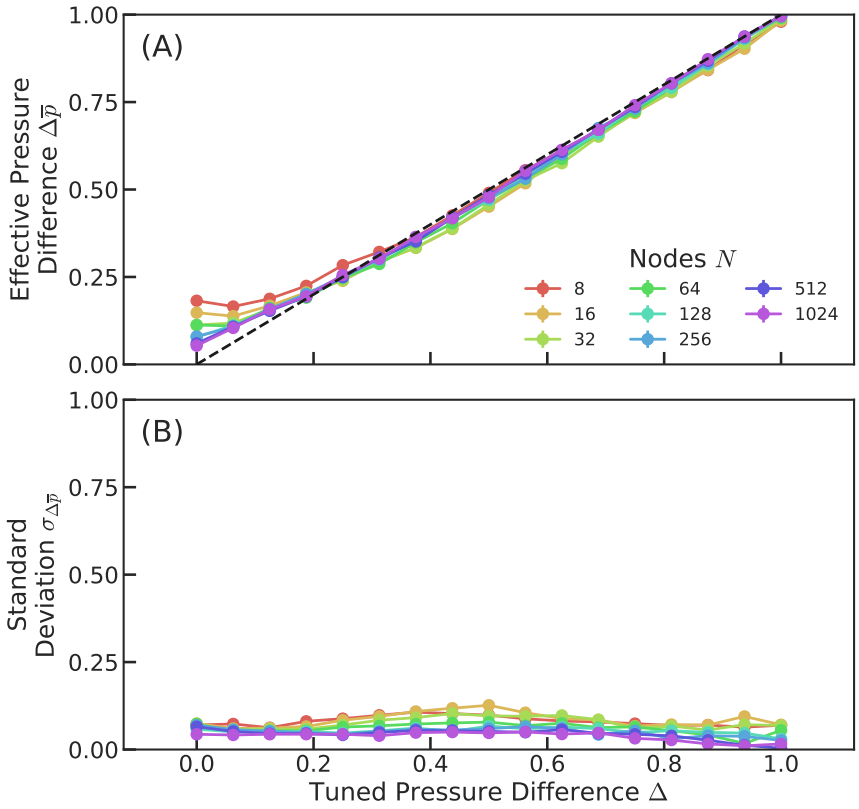

Figure 4.8: (A) Average difference in median node pressures $\Delta\overline{p}$ between the two sectors corresponding to the two target nodes for a variety of system sizes N and target pressure difference Δ. The black dashed line corresponds to $\Delta\overline{p} = \Delta$. (B) Average standard deviation of the distribution of $\Delta\overline{p}$ at each value of N and Δ.

histogram in Fig. 4.7(C3) associated with each sector now comprise separate peaks. The nodes are almost completely partitioned into the two regions with node pressures of different signs. The effective pressure difference between the two sectors is $\Delta\overline{p} = 0.21$, closely tracking the tuned pressure difference, and the persistence is $\hat{\tau} = 0.46$.

Finally, Figs. 4.7(D1) and (D2) show a complete partitioning of the network according to node pressure at a tuned pressure difference of $\Delta = 1.0$. The histogram in Fig. 4.7(D3) confirms this, as it shows two narrow peaks of node pressures with $\Delta\overline{p} = 1.0$ and a maximum possible persistence of $\hat{\tau} = 1.0$.

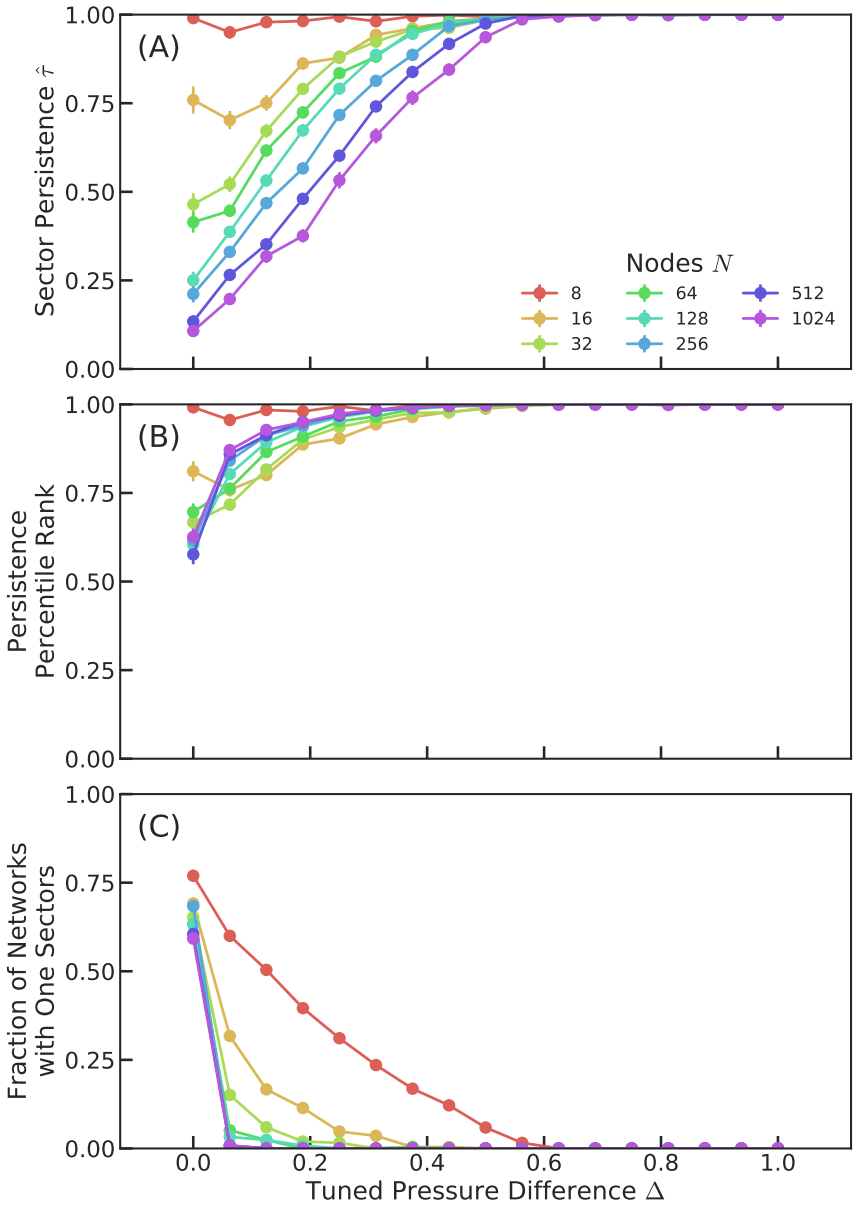

Figure 4.9: (A) Average normalized persistence $\hat{\tau} = \tau/\tau_{\max}$ of the two sectors for a variety of system sizes N and target pressure differences Δ. A maximum value of one indicates maximum topological significance. (B) Average percentile rank of $\hat{\tau}$ for the two sectors out of all possible pairs of sectors in a given network. The percentile rank is calculated independently for each network before averaging. (C) Fraction of networks where the target nodes can

In summary, Fig. 4.7 shows that as the target edge is tuned to larger and larger pressure differences, the network's response steadily partitions the nodes into two distinct sectors, even as the underlying network architecture remains a single con-

nected component. The node pressures within each sector are relatively uniform and the difference between the median pressures in the two sectors corresponds closely to the tuned target pressure difference. The separation of the two regions, as measured by the normalized persistence $\hat{\tau}$, increases as well, to a maximum value of $\hat{\tau} = 1.0$ in the limit $\Delta = 1.0$.

We have established the generality of this observation by tuning many networks to a variety of target pressure differences, obtaining the two sectors with the largest normalized persistence $\hat{\tau}$ that separate the target nodes in each case. For each network, we calculate the effective pressure difference $\Delta\overline{p}$, the difference in median node pressures between the two sectors. Fig. 4.8(A) shows the average of $\Delta\overline{p}$ for various system sizes N and target pressure differences Δ. Each point is calculated by averaging the results over an ensemble of 512 independent networks. We see that $\Delta\overline{p}$ is close to Δ for all system sizes and target pressure differences, with almost perfect agreement for larger systems. We also measure the average standard deviation $\sigma_{\Delta\overline{p}}$ of the effective pressure difference for each system size and tuning threshold in Fig. 4.8(B). We see that the spread of each distribution is very narrow, especially for large N. (Note: We choose the median, rather than the mean, to reduce the effect of the source nodes, which are typically outliers in the node pressure distributions of the two sectors. This choice only improves the results for very small system sizes tuned for small values of Δ).

The rest is completely rewritten

In Fig. 4.9(A), we measure the average normalized sector persistence taken as the persistence of the birth-death pair associated with the boundary (death) separating the two sectors, normalized by the maximum persistence of any birth-death pair for that particular network, $\hat{\tau} = \tau/\tau_{\max}$. We see that the sector persistence approaches a maximum value of one for large tuning thresholds, indicating the sectors correspond to one of the most topologically significant features for each network. To further validate this, Fig. 4.9(B) shows the average rank percentile of $\hat{\tau}$ out of all birth-death pairs with nonzero persistence within each network. We see that in all cases, the rank percentile is close to unity, indicating that even if the sectors do not correspond to the feature with highest persistence in a given network, they still correspond to one of the most topologically significant features.

Sometimes it is not possible to divide the network into two sectors either because the target nodes are not separate by a boundary edge or a lack of any birth-death pairs, indicating no topological features were found during the filtration. In these cases, we exclude the network from all of our results. Fig. 4.9(C) measures the number of networks that cannot be divided successfully into two sectors. We see that this only occurs for small system sizes or for larger systems when Δ is zero.

Since the sectors we find correspond to relatively uniform node pressures, calculate the similarity of the tuned network response with an approximate response where each sector is assigned a uniform node pressure equal to its average in the exact response. Given a network with N nodes, we represent the response with as length N vector $\vec{p}$ where the ith component is the pressure of the ith node. Similarly, we define the

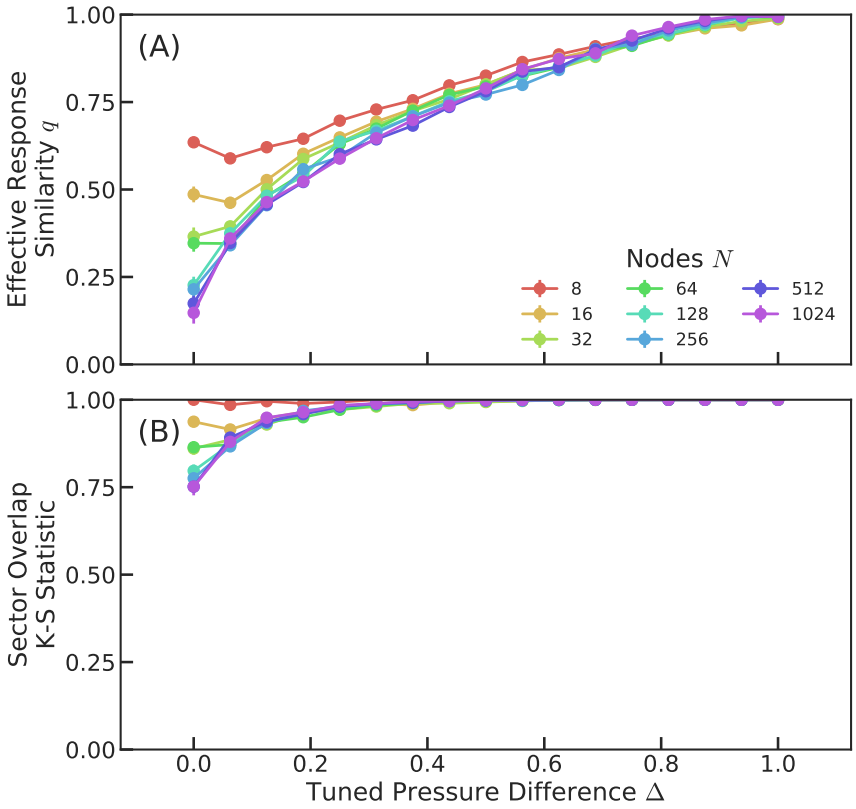

Figure 4.10: Average similarity of the effective measured response with the actual response of the network for a variety of system sizes N and target pressure differences Δ. The approximate response is calculated by assigning each node within a sector a pressure equal to the average pressure within that sector.(B) The average two-sample Kolmogorov-Smirnov statistic between the distributions of node pressures of the two sectors for each system for the actual response. This measures distance between the two distributions with zero indicating maximum overlap of the two, and one indicating no overlap.

represent the approximate response as the vector $\vec{p}'$. We measure the similarity of these two responses using the following measure of overlap:

$$q = \frac{\vec{p} \cdot \vec{p}'}{p^2 + p'^2}$$

where p and p_{eff} are the norms of the two vectors. This measure of overlap of the two vectors is zero when the vectors are orthogonal and one if both their directions

and magnitudes are identical. In Fig. 4.10(A), we see that q steadily increases to a maximum value of one for large Δ. Although, it is not perfectly one for all tuning thresholds, q is substantially greater than zero for all system sizes and tuning thresholds.

Fig. 4.10(B) shows the average two-sample Kolmogorov-Smirnov (K-S) statistic between the node pressure distribution of the two sectors (the green and orange histograms in Fig. 4.7) for each network. This quantifies the difference between the contributions to the total node pressure histograms of the two sectors, with a value of one indicating no overlap between the two sectors (as in Fig. 4.7(D3)) and zero indicating that the two sectors overlap significantly (as in Fig. 4.7(B3)). We see that the K-S statistic quickly approaches unity with increasing Δ, especially for larger N, indicating that the two sectors rapidly segregate into regions with non-overlapping distributions of node pressures.

Finally, Fig. 4.11 shows the four sectors for a multifuncitonal flow network where six separate target edges have each been tuned to $\Delta = 0.2$. In the presence of multiple targets, it is generally not possible use the skeletonized tree representation of a network to simultaneously separate each pair of targets using only two sectors. Therefore, we extend our coarse-graining procedure to account for the possibility of multiple relevant sectors. T accomplish this, we first treat each pair of target nodes separately, recording the boundary edge of highest persistence that places each node into a separate sector. The result is a list of boundary edges which is less than or equal to the number of targets. We then use these boundary edges as the

boundaries between each sector within the tree. Fig. 4.11(A) shows the structure of the network, while Figs. 4.11(B) and (C) show the pressure differences on the edges and the skeletonized tree represenation of the network. In Fig. 4.11(C), we see that each of the four sectors comprises a distinct peak in the histogram of node pressures. The separation between neighboring peaks roughly corresponds to the tuned response of $\Delta = 0.2$.

4.7 Discussion

4.7.1 Summary

In summary, we have established a quantitative characterization of function in flow networks by analyzing their responses using persistent homology. This analysis reveals the topological means by which function is tuned into these networks, providing a clear relationship between structure and function. As a network is tuned to larger and larger pressure differences at the target, it segregates into two sectors of relatively uniform pressure which characterize and predict the tuned response. These sectors are a property of the response of the network to external stimuli, rather than solely the underlying graph structure (i.e. the node connectivity and edge weights). Although the network does not physically separate into two topologically distinct components, the topology of the response robustly sorts each node into a particular sector.

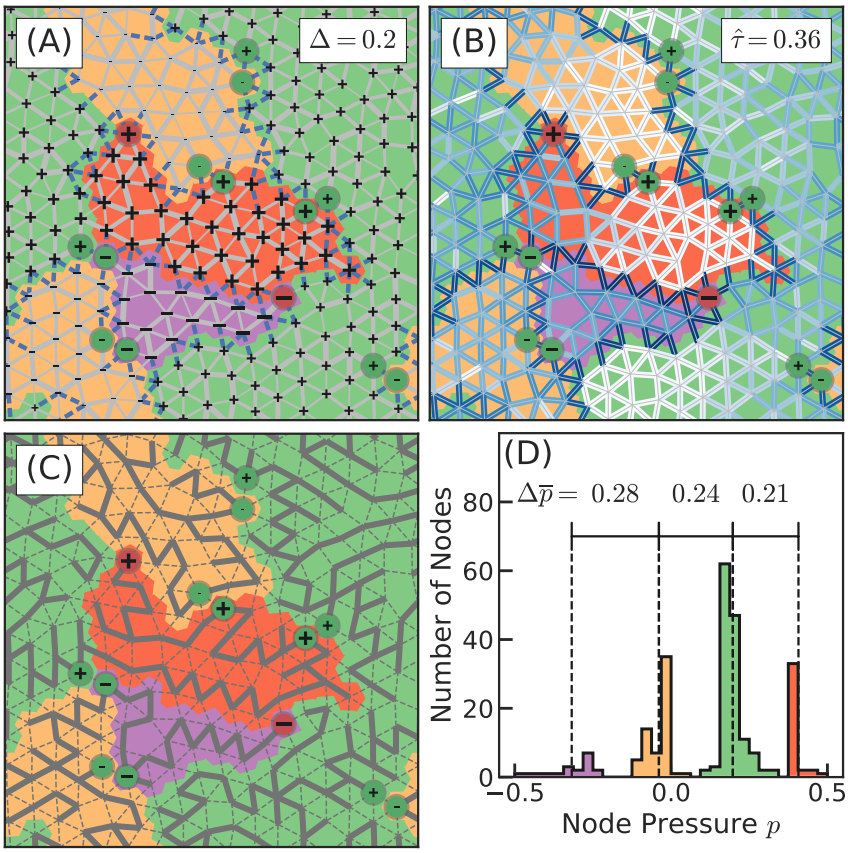

Figure 4.11: Network tuned to perform a multifunctional task: When a unit pressure difference is applied across the source nodes (shown in red) six separate pairs of target nodes (shown in green) have each been tuned to exhibit a pressure difference of at least $\Delta = 0.1$. (A-C): The network can be decomposed into four distinct sectors colored in green, orange, purple, and red. (A) The pressures on the nodes are shown in black where the symbol denotes the sign of the pressure and the size denotes the magnitude. The thickness of the edges corresponds to the conductance. Edges that are shown as thick blue dashed lines have been completely removed in the process of tuning. (B) The absolute values of the pressure differences are shown in white-to-blue on a log scale. (C) Skeletonized tree representation of the network encoding the topological structure of the network. (D) The histogram of nodes pressures with portions highlighted in different colors corresponding to the contributions of each sector. Each sector comprises a separate peak in the histogram, with the differences between neighboring peaks each approximating the tuned response of the targets.

This description provides a unifying description for all flow networks tuned to perform this type of function, including networks with different underlying network architectures tuned for the same function and networks with the same underlying network

architectures tuned for different functions. This description also extends to networks tuned to perform complex, multifunctional tasks. In analogy to the way in which genus is used to classify manifolds with different numbers of holes, independent of geometrical details (e.g. the famous equivalence between a coffee cup and a doughnut), the number of connected components (i.e. the 0th Betti number) encoded in the response allow us to classify tuned networks.

Although the local node connectivity and geometrical structure can differ between two networks tuned for the same function, the commonality in structure of the networks becomes apparent when viewed through a topological lens. This leads us to propose a refinement of the structure-function paradigm in the context of functional flow networks. Since the process of tuning is inherently topological, the aspect of structure that relates to function is also topological; it is the relationship between the *topological structure* and function that is important, not the relation between geometric structure and function. The fact that the structure-function relationship is topological contributes to the robustness of our results even in the case of small Δ, when the structures relevant to the tuned function are not discernible by eye.

We have also demonstrated that the techniques provided by persistent homology - both the persistence algorithm and our persistence-based coarse-graining procedure - are powerful tools for quantifying network structures in a unique and threshold-independent manner. The persistence algorithm allows us to identify the general physics that distinguishes between systems (*e.g.* tuned and untuned networks) by taking advantage of statistical differences in topological structure, but is unable to

uncover the precise features responsible. The coarse-graining procedure allows the topological differences revealed by the persistence algorithm to be translated into concrete and unique features (in this case two connected components), even in the case of noisy data.

4.7.2 Experimental Implications and Application

The techniques we have demonstrated, along with the resulting characterization of the tuning process, reveal a path forward for understanding biological flow networks in experiment. Obtaining an accurate and complete map of every single vessel of an entire organ or organism poses a difficult experimental challenge, as vasculature networks frequently consist of millions of nodes and span several lengthscales. In addition, it is known that small errors in the connectivity or conductances can be disastrous in determining function [10]. In spite of these obstacles, experimental researchers have directed their efforts to fully characterizing node connectivity and edge conductances (vessel diameters) [13]. Our results show that such detailed knowledge of the underlying network architecture is not necessary. Rather, we suggest taking measurements of local *pressure*, as function is encoded robustly in regions of nearly-uniform node pressure.

In its current form, our analyses does not require information about the edge weights (conductances), nor the locations of the source nodes. However, we do utilize information about the node pressures, local node connectivity, and locations of the target

nodes. In practice, perfect knowledge of these details will not always be available in an experimental setting. Here we propose several variations of our analysis which may alleviate the need for such information.

First, perfect knowledge of node pressure and connectivity is not strictly necessary. In fact, as long as pressure is measured at enough locations with small enough spacings in order to capture fluctuations at desired length scales, a best-guess reconstruction of the network in which edges are placed between nearest neighbors (e.g. a Delaunay triangulation) would suffice. This could potentially eliminate the need for any measurement of the vessel micro-structure.

Second, Figs. 4.9(A) and (B) reveal that the sectors that best separate the target nodes typically correspond to one of boundary edges with highest topological significance, that is, the largest normalized persistence $\hat{\tau}$. If the scale of the fluctuations in pressure differences relevant to network function is approximately known, then all boundary edges with persistence above some threshold could be used to define the final sectors. Not only does this eliminate the need to know the target edges, but it also loosens the restriction that the network is divided into only two sectors. We have already shown in Fig. 4.11 that developing an understanding of multifunctionality would require this generalization. (In the case of flow networks, the approach we describe should be identical to the persistence-based simplification described in Refs. [60] and [12]. Although constructing the skeletonized tree version of a network and identifying boundary edges is sufficient, we provide instructions in order to directly apply persistence-based simplification to flow networks in the Appendix.)

Alternatively, boundary edge(s) could be chosen which maximize the similarity q between the actual and approximate uniform responses. We know from Figs. 4.10(A) that q is often large for the final sectors. While coarse-graining the network to eliminate features of low persistence should eliminate noise from small fluctuations in pressure, optimizing for large q could be useful for eliminating larger-scale fluctuations, as long as they only occur at small length scales.

In summary, the alternative approaches we propose reduce experimental requirements of our analysis to only partial measurements of node pressure at relatively closely spaced intervals. It does not require, knowledge of the small-scale micro-structure of the underlying network, nor the locations of source and target nodes. It should also be robust to noise characterized by low-amplitude fluctuations in pressure or fluctuations on small length scales, depending on the specifics of the implementation. We hope that our results will inspire experimentalists to characterize network structures using a topologically-informed approach, revealing the underlying relationship between structure and function.

4.7.3 Broader Impacts

The the persistence analysis we performed allowed us to detect the topological signature of tuning using persistence diagrams, without making any assumptions about the underlying process. The persistence-based coarse-graining procedure then allowed us to identify unique regions of each network corresponding to these features. We note

that here are many procedures exist to decompose networks into local community structures and quantify modularity [36]. However, none of these procedures provide the guarantee that the resulting sectors uniquely correspond to the features (birth-death pairs) we observed in the persistence diagrams. In addition, it is only after following the persistence process we have demonstrated that it becomes obvious that these sectors encode function, as they are present in the tuned response, not the underlying network architecture.

In particular, many methods make use of tree representatations of networks, known as dendrograms, to perform divisive hierarchical clustering algorithms [65]. While we also create a skeletonized tree representation of our networks, we note that they are not dendrograms. Persistent homology provides a rigorous mathematical foundation for constructing our trees. Coarse-graining based on persistence, rather than simply looking for boundaries with large pressure differences, ensures that the sectors we find are topologically significant. This is important as edges located near the source nodes typically have very large nodes pressure, creating small sectors with large pressure difference boundaries. However, they often have small persistence values (they contain small ranges of pressure differences) and are not necessarily relevant to the tuned function. Constraining the target nodes to be located in separate sectors also helps to eliminate the influence of these small sectors, even when they have relatively large persistence values. In addition, simply choosing a cutoff in node pressure to separate the network into sectors would be difficult for smaller Δ. As seen in Figs. 4.7(B3) and (B4), the nodes do not always cleanly separate into two regions separate by a

gap in pressure.

In the past, algorithms have been proposed to take advantage of the properties of resistor networks to detect modular neighborhoods in other types of networks as well. To detect community structures, a unit resistance is assigned to each edge and a voltage is applied across a pair of source nodes. In one implementation, edges with large currents can be removed to divide the network into community structures [79]. Alternatively, if a network has a high degree of modularity, it can be divided into regions separated by large pressure differences [81]. However, if a network is not very modular, choosing an appropriate cutoff in pressure can be difficult. Both of these approaches require testing every possible pair of source nodes, or randomly sampling a sufficiently large number of possible pairs, limiting these approaches to smaller networks in practice. Our approach does not suffer from any of the these drawbacks.

Another set of related methods focuses on detecting bottlenecks, or minimum cuts, in general transportation networks [1]. In the context of network flow optimization (in which flows are more broadly construed to allow for upper and lower bounds on edge currents and unidirectional edge current constraints), an $s-t$ cut is a set of edges that when removed partitions the nodes of a flow network into two components, one containing the source node s (positive node pressure) and the other the sink node t (negative node pressure). The *max-flow min-cut* theorem states that the maximum possible value of the flow from a source node to a sink node is given by the total sum of the edge weights (conductances) defining the minimum cut, the $s-t$ cut with the minimum possible sum of edge weights. Various algorithms utilize this theorem to

calculate maximum flows and, by extension, minimum cuts [1]. While we expect that the sectors we obtain are closely related to those found by the mininum cut algorithms, we do expect some differences as these algorithms generally require an upper bound on the maximum flow (capacity) through a sufficient number of edges, while our flow networks lack these constraints. Developing a formal connection between these two methods could provide further insight into the physical interpretation of the components we detect, along with a deeper understanding of the topological properties of more general transport networks.

In our tuned flow networks, crack-like structures formed by edge removals partition the network into different sectors. These crack-like defects in resistor networks have been studied in some detail in the random resistor network literature, but not in the context of tuning [57]. By forming cracks, bottlenecks form between the sectors, inhibiting the flow of current between the source nodes. When tuning pressure difference, these bottlenecks are located far from the target edge. However, if one were to tune current through the target edge rather than the pressure difference, we expect these bottlenecks would form at the target. An analytical theory of tuning would likely require providing a relationship between these crack structures, the segregation of the network into sectors, and the tuned response. This work has provided an important step towards relating the latter two, but has not explicitly explored the role of cracks.

The analysis introduced here is general and could also be used to study the relationship between structure and function of flow networks tuned to perform other types

of tasks such as displaying a specific current response or power loss through a target edge, or networks optimized to minimize global power loss, etc. However, the problem of tuning the pressure difference through an edge provides a good starting point for our analysis that can be extended easily to networks tuned to perform more complex tasks composed of multiple targets such as those in Ref. [62].

Since these techniques do not depend on the local node connectivity, we would also expect our results to be robust to the overall network topology before tuning (e.g. non-planar, non-local edge structures or network with high degrees of modularity). As long has a function has been successfully tuned into a network, we would expect qualitatively similar results. In addition, in this work we only explored the nature of connected components (0-cycles), but the persistence algorithm can also be used to identify significant cycles of edges (1-cycles) as well. Repeating our analysis to quantify the 1-cycle topology may prove useful in understanding the effects of the untuned network properties on what types of functions a network can be tuned to perform.

Biological flow networks employ a variety of mechanisms over a wide range of time scales in order to regulate local flow. On relatively short time scales, the vasculature systems of animals – notably that of the brain – and slime molds can dynamically control local flow by constricting and dilating vessels in order to support local activity. On longer time scales, animals, fungi, and slime molds can control flow to restructure the vasculature network. All these systems also undergo evolution on generational time scales to modify their network designs depending on the needs of the system or

environmental changes. In all cases, our results suggest there may be a topological basis for function that could be uncovered by applying the analysis introduced here.

Given that flow networks are mathematically equivalent to one-dimensional mechanical networks [62], our results suggest that one could ask whether the structure-function relationship is also topological in mechanical networks that can perform mechanical functions, such as motor proteins or allosteric proteins. Mechanical networks can also be tuned to perform specific functions [61, 82, 21] and can undergo topological changes in structure, displaying responses ranging from hinge-like motions [16, 83] to more exotic "trumpet"-like responses [82]. The extreme case of a flow network segregated into two components with $\Delta = 1$ is analogous to the notion of a mechanical mechanism, or soft mode, since the response does not require any expenditure of energy (or power in the case of flow networks). The role of soft modes in function has been studied in proteins [3]. Our analysis of flow networks provides a generalization of this idea to the case where the components are still connected with $\Delta < 1$. A similar analysis is therefore likely to be useful in identifying the generalization of a mechanical mechanism to the case where the deformation involved in the function is not a soft mode.

More generally, a topological description of function may help elucidate significant structures in other types of non-conservative or nonlinear functional networks. For example, one could ask whether characteristic topological features correspond to memories encoded in neural networks trained via machine learning or in neuron networks.

Finally, we wish to emphasize that applications of persistent homology to networks, including studies of flow networks in particular, tend to focus on the underlying network structure, not the response of the network [38, 45, 40, 41](Perhaps add more examples?). By using flow networks as a model system, in this work we established that the topology of the response encodes the function of a network, not just the topology of the underlying graph structure. It is the topology of the response that provides the bridge between structure and function.

4.8 Appendix

4.8.1 Network Tuning Protocol

For this work, we follow the tuning procedure detailed in Ref. [62] with a small modification. Rather than tuning the relative change in the response of the target, here we tune the value of the target pressure difference directly. In addition, the pressure difference on a given edge is the difference between the pressures of the two nodes connected by that edge, with a sign that is arbitrary because the nodes are not ordered. This means that the sign of the target pressure difference before tuning can be negative. In such a case, a small amount of tuning is necessary even when Δ is zero.

4.8.2 Persistence Algorithm Details

In the main text, we describe simplified versions of the persistence and simplification algorithms. Here we provide the additional details that in conjunction with Refs. [17], [60], and [12], comprise the full versions of the algorithms used here. We will use the language of the aforementioned references to facilitate the merging of our approach with theirs.

We represent a network as a graph $\mathcal{G} = (\mathcal{V}, \mathcal{E})$ which is a tuple composed of a set of N vertices (nodes) $\mathcal{V} = \{v_1, \ldots, v_N\}$ and a set of N_E edges $\mathcal{E} = \{e_1, \ldots, e_{N_E}\}$. On each edge i we define a function $g(e_i) = |\Delta p_i|$ which is the absolute value of the pressure difference on that edge.

We model a graph $\mathcal{G}$ as a cell complex $\mathcal{K}(\mathcal{G})$ composed of the collection of both the vertices (0-dimensional cells) and edges (1-dimensional cells). When necessary, we denote the dimension of a p-dimensional cell (or p-cell for short) by a superscript $\alpha^{(p)}$. We say a cell $\alpha^{(p)}$ is the face of another cell $\beta^{(q)}$ if $p \leq q$ and the vertices of $\alpha^{(p)}$ are a subset of the vertices of $\beta^{(q)}$. If p is strictly less than q, we write this relationship as $\alpha^{(p)} < \beta^{(q)}$, while if $p \leq q$, we write $\alpha^{(p)} \leq \beta^{(q)}$.

Network Filtration

To perform both the persistence algorithm, we need to formally define a filtration on our cell complex $\mathcal{K}(\mathcal{G})$. This requires prescribing an ordering on all cells, including

both edges and vertices, with the requirement that a cell must always be ordered after its faces. In analogy to Ref. [60], we define the upper costar of an edge x as the set of cells it introduces into the cell complex,

$$U(x) = \{\alpha \in \mathcal{K} \mid x \geq \alpha \quad \text{and} \quad g(x) = \min_{y \geq \alpha} g(y)\} \tag{4.8.1}$$

These sets provide a unique non-overlapping partitioning of $\mathcal{K}(\mathcal{G})$. Since we only have vertices and edges, these sets can only be composed of (i) a single edge, (ii) an edge and one of its vertices, or (iii) an edge and both of its vertices (In Ref. [60], function values are defined on the vertices, resulting in the use of lower stars. However, here we have function values that are defined on the edges, resulting in the use of upper costars). Now we can define level cuts of our cell complex, composed of all cells in upper costars whose defining edge has a function value less than t,

$$\begin{aligned} \mathcal{K}_t(\mathcal{G}) = \{\alpha \in \mathcal{K}(\mathcal{G}) \mid \alpha \in U(x) \\ \text{and} \quad g(x) \leq t, \quad \forall x \in \mathcal{E}\} \end{aligned} \tag{4.8.2}$$

The resulting sequence of level cuts $\mathcal{K}_t(\mathcal{G})$ for increasing values of t define the ascending filtration of $g(x)$ on $\mathcal{K}(\mathcal{G})$ used to perform the standard persistence algorithm, which is described in detail in Ref. [17].

The result of using this filtration to perform the persistence algorithm would be to assign a birth-death pair to every edge that does not create a 1-dimensional cycle. Each of these edges join together a pair of vertices comprising separate components

and would therefore constitute a death edge. In case (i), as long as the edge does not create a 1-cycle, it would combine two connected components and be assigned a nonzero persistence. In case (ii), a new component would be born with the introduction of a vertex, but immediately die with the corresponding edge. In case (iii), two new components would be born with the two new vertices, but one would immediately die with the introduction of the edge. Therefore, edges associated with cases (ii) and (iii) would be assigned a persistence of $\tau = 0$ and be skipped when finding a pair of sectors. However, edges from all three cases that do not create 1-dimensional cycles would be included in the skeletonized tree representation of the network.

Persistence-based Simplification

In the main text, we outline a simplified version of a persistence-based simplification algorithm for finding sectors with large associated persistence values, inspired by the procedure described in Refs. [60] and [12]. While the algorithm we provide is sufficient, here we describe the modifications one would make in order to directly adapt the full version from the provided references. The first step in the simplification process is to compute a discrete gradient vector field, V, composed of a collection of pairs of cells $(\alpha^{(p)} < \beta^{(p+1)})$ in $\mathcal{K}_t(\mathcal{G})$ such that each cell is in at most one pair. Unpaired cells are called "critical cells" and represent essential topological features (analogous to critical points on a manifold). This vector field encodes the topological structure and is later used to determine which topological features to eliminate. In Ref. [60], constructing V makes use of a lower star filtration which requires function values

defined on the vertices. However, we define our function values on the edges and use an upper costar filtration. To accommodate this difference, we provide a new algorithm *ProcessUpperCostars* which is essentially the dual version of Algorithm 1. *ProcessLowerStars* in Ref. [60].

Similar to its counterpart, *ProcessUpperCostars* requires an ordering of all cells within each upper costar. Given a cell $\alpha \in U(x)$ with coface edges $\{x, y_{i_1}, \ldots, y_{i_k}\}$ (for a vertex, this list is composed of all adjacent edges, while for an edge it simply contains itself), define

$$\begin{aligned} G(\alpha) &= (g(x), g(y_{i_1}), \ldots, g(y_{i_k})) \\ &\text{where} \quad g(x) < g(y_{i_1}) < \cdots < g(y_{i_k}) \end{aligned} \tag{4.8.3}$$

Each cell is then ordered according to two criteria: (i) cell dimension ordered from smallest to largest (the faces of a cell must always appear before that cell) and (ii) the lexicographic ordering of these sequences from largest to smallest. All other functions or objects in *ProcessUpperCostars* that we do not explicitly define are identical to those in Ref. [60] (or can be transparently inferred).

Algorithm 1 ProcessUpperCostars($\mathcal{E}, g$)
Input $\mathcal{E}$ set of edges in network
Input g values on edges
Output C critical cells
Output V discrete vector field $V[\alpha^{(p)}] = \beta^{(p+1)}$

```
1: for x ∈ E do
2:     add all α ∈ U(x) to PQzero such that
       num_unpaired_cofaces(α) = 0
3:     add all α ∈ U(x) to PQone such that
       num_unpaired_cofaces(α) = 1
4:     while PQone ≠ ∅ or PQzero ≠ ∅ do
5:         while PQone ≠ ∅ do
6:             α := PQone.pop_front
7:             if num_unpaired_cofaces(α) = 0 then
8:                 add α to PQzero
9:             else
10:                V[pair(α)] = α
11:                remove pair(α) from PQzero
12:                add all cells β ∈ U(x) to QPone such that
                   (β < α or β < pair(α)) and
                   num_unpaired_cofaces(β) = 1
13:            end if
14:        end while
15:        if PQzero ≠ ∅ then
16:            γ := PQzero.pop_front
17:            add γ to C
18:            add all cells α ∈ U(x) to PQone such that
               α < γ and num_unpaired_cofaces(α) = 1
19:        end if
20:    end while
21: end for
```

Chapter 5

Conclusions and Future Directions

By approaching allostery as a problem in matematerials design, this dissertation provides an alternative framework in which to understand this type of functionality in both flow and mechanical networks. Chapter 2 demonstrated that very little is necessary to create mechanical networks with allosteric behavior, providing insight into why allosteric proteins are common in nature. Chapter 3 extended this description to flow networks, unifying both systems into a single mathematical framework. It also showed that the limits of multifuncionality in both systems are governed by the same constraint satisfaction phase transition. Finally, Chapter 4 revealed the underlying basis of function in flow networks, showing that the relationship between structure and function is topological in nature as it does not depend on the precise details of the local network architecture, instead being topologically encoded in the response.

The results presented in this dissertation provide the blueprint for the next steps

in developing a complete quantitative understanding of allostery. The topological analysis of flow networks in Chapter 4 provides a unified description of function that applies to networks with different underlying architectures tuned for the same function, as well as networks with the same underlying architecture tuned for different functions. As a flow network is tuned to display larger and larger responses, its response topologically separates the network into two sectors which correlate strongly with tuned function. This result suggests that a similar description could be developed for allosteric mechanical networks as well. The fact that many allosteric proteins exhibit hinge-like motions suggests that this should be possible, as a hinge is the mechanical analog to the sectors seen in flow networks. Once such a description is developed, an analysis of real protein structures would be possible, providing a robust quantitative characterization of allostery in real systems. Such a characterization would provide insight to enable the development of a general topological theory of allostery which clearly relates atomic structure to biological function, as it would be robust to the complexity and variety of protein structures. The structural order parameters revealed by topological data analysis provide a strong starting point for developing a general analytical theory.

Finally, it would be very interesting to follow the route we have provided to investigate functionality in other types of networks. In principle, any system which can be described as a network which takes in a limited number of local inputs and propagates the response to another set of localized outputs could be approached in a similar manner. In particular, identifying the underlying structural mechanisms responsible

for function in neural networks used in machine learning remains a critical area of study. One could also imagine extending our topological approach to take into account the dynamical aspects of complex networks such as those present in proteins or neuron networks in the brain. By combining insights from a wide variety of fields ranging from structural biology to mechanical matematerials to applied topology, making sense of allostery in proteins, and complex networks in general, should become an achievable goal in the foreseeable future.

Bibliography

[1] Ahuja, R. K., Magnanti, T. L., and Orlin, J. B. 2014. *Network flows : theory, algorithms, and applications*. Prentice-Hall, Upper Saddle River, New Jersey, 1st edition.

[2] Atilgan, C., Gerek, Z. N., Ozkan, S. B., and Atilgan, A. R. 2010. Manipulation of conformational change in proteins by single-residue perturbations. *Biophysical Journal*, 99(3): 933–943.

[3] Bahar, I., Lezon, T. R., Bakan, A., and Shrivastava, I. H. 2010. Normal mode analysis of biomolecular structures: Functional mechanisms of membrane proteins. *Chemical Reviews*, 110(3): 1463–1497.

[4] Berthier, L. and Biroli, G. 2011. Theoretical perspective on the glass transition and amorphous materials. *Reviews of Modern Physics*, 83(2): 587–645.

[5] Blinder, P., Tsai, P. S., Kaufhold, J. P., *et al.* 2013. The cortical angiome: An interconnected vascular network with noncolumnar patterns of blood flow. *Nature Neuroscience*, 16(7): 889–897.

[6] Bussolino, F., Arese, M., Audero, E., *et al.* 2010. Biological Aspects of Tumour Angiogenesis. In L. Preziosi, editor, *Cancer Modeling and Simulation*, chapter 1, pages 1–22. Chapman & Hall/CRC.

[7] Calladine, C. R. 1978. Buckminster Fuller's "Tensegrity" structures and Clerk Maxwell's rules for the construction of stiff frames. *International Journal of Solids and Structures*, 14(2): 161–172.

[8] Changeux, J. P. 2011. 50th anniversary of the word "allosteric". *Protein Science*, 20(7): 1119–1124.

[6] Chiou, K. K., Rocks, J. W., Chen, C. Y., *et al.* 2016. Mechanical signaling coordinates the embryonic heartbeat. *Proceedings of the National Academy of Sciences*, 113(32): 8939–8944.

[10] Crucitti, P., Latora, V., Marchiori, M., and Rapisarda, A. 2004. Error and attack tolerance of complex networks. *Physica A: Statistical Mechanics and its Applications*, 340(1-3): 388–394.

[11] Daily, M. D. and Gray, J. J. 2007. Local motions in a benchmark of allosteric proteins. *Proteins: Structure, Function and Genetics*, 67(2): 385–399.

[12] Delgado-Friedrichs, O., Robins, V., and Sheppard, A. 2015. Skeletonization and partitioning of digital images using discrete morse theory. *IEEE Transactions on Pattern Analysis and Machine Intelligence*, 37(3): 654–666.

[13] Di Giovanna, A. P., Tibo, A., Silvestri, L., *et al.* 2018. Whole-Brain Vasculature Reconstruction at the Single Capillary Level. *Scientific Reports*, 8(1): 12573.

[14] Dokholyan, N. V. 2016. Controlling Allosteric Networks in Proteins. *Chemical Reviews*, 116(11): 6463–6487.

[15] Driscoll, M. M., Chen, B. G.-g., Beuman, T. H., *et al.* 2015. Tunable failure: control of rupture through rigidity. *Proceedings of the National Academy of Sciences*, 113(39): 201501169.

[16] Dutta, S., Eckmann, J.-P., Libchaber, A., and Tlusty, T. 2018. Green function of correlated genes in a minimal mechanical model of protein evolution. *Proceedings of the National Academy of Sciences*, 115(20): E4559–E4568.

[17] Edelsbrunner, H. and Harer, J. L. 2010. *Computational topology : an introduction*. American Mathematical Society.

[18] Edwards, S. A., Wagner, J., and Gräter, F. 2012. Dynamic prestress in a globular protein. *PLoS Computational Biology*, 8(5): e1002509.

[19] Ellenbroek, W. G., Zeravcic, Z., Van Saarloos, W., and Van Hecke, M. 2009. Non-affine response: Jammed packings vs. spring networks. *Europhysics Letters*, 87(3): 34004.

[20] Ellenbroek, W. G., Hagh, V. F., Kumar, A., Thorpe, M. F., and Van Hecke, M. 2015. Rigidity loss in disordered systems: Three scenarios. *Physical Review Letters*, 114(13): 135501.

[21] Flechsig, H. 2017. Design of Elastic Networks with Evolutionary Optimized Long-Range Communication as Mechanical Models of Allosteric Proteins. *Biophysical Journal*, 113(3): 558–571.

[22] Folli, V., Leonetti, M., and Ruocco, G. 2017. On the Maximum Storage Capacity of the Hopfield Model. *Frontiers in Computational Neuroscience*, 10: 144.

[23] Franz, S., Parisi, G., Sevelev, M., Urbani, P., and Zamponi, F. 2017. Universality of the SAT-UNSAT (jamming) threshold in non-convex continuous constraint satisfaction problems. *SciPost Physics*, 2(3): 019.

[24] Fuchi, K., Buskohl, P. R., Bazzan, G., *et al.* 2015. Origami Actuator Design and Networking Through Crease Topology Optimization. *Journal of Mechanical Design*, 137(9): 091401.

[25] Gallotti, R. and Barthelemy, M. 2015. The multilayer temporal network of public transport in Great Britain. *Scientific Data*, 2: 1–8.

[26] Gao, Y. R., Greene, S. E., and Drew, P. J. 2015. Mechanical restriction of intracortical vessel dilation by brain tissue sculpts the hemodynamic response. *NeuroImage*, 115: 162–176.

[27] Goodrich, C. P., Liu, A. J., and Nagel, S. R. 2012. Finite-size scaling at the jamming transition. *Physical Review Letters*, 109(9): 095704.

[28] Goodrich, C. P., Liu, A. J., and Nagel, S. R. 2015. The Principle of Independent Bond-Level Response: Tuning by Pruning to Exploit Disorder for Global Behavior. *Physical Review Letters*, 114(22): 225501.

[29] Granger, J. and Cipolla, M. J. 2016. *The Cerebral Circulation*. Morgan & Claypool Publishers, 2nd edition.

[30] Guarnera, E. and Berezovsky, I. N. 2016. Allosteric sites: Remote control in regulation of protein activity. *Current Opinion in Structural Biology*, 37: 1–8.

[31] Gunasekaran, K., Ma, B., and Nussinov, R. 2004. Is allostery an intrinsic property of all dynamic proteins? *Proteins: Structure, Function and Genetics*, 57(3): 433–443.

[32] Hadjistassou, C., Bejan, A., and Ventikos, Y. 2015. Cerebral oxygenation and optimal vascular brain organization. *Journal of the Royal Society Interface*, 12(107): 20150245–20150245.

[33] Heaton, L., Obara, B., Grau, V., *et al.* 2012. Analysis of fungal networks. *Fungal Biology Reviews*, 26(1): 12–29.

[34] Hexner, D., Liu, A. J., and Nagel, S. R. 2018. Role of local response in manipulating the elastic properties of disordered solids by bond removal. *Soft Matter*, 14(2): 312–318.

[35] Ivet Bahar, Timothy R. Lezon, Lee-Wei Yang, E. E. 2010. Global Dynamics of Proteins: Bridging Between Structure and Function. *Annual Review of Biophysics and Biomolecular Structure*, 9(39): 23–42.

[36] Javed, M. A., Younis, M. S., Latif, S., Qadir, J., and Baig, A. 2018. Community detection in networks: A multidisciplinary review. *Journal of Network and Computer Applications*, 108: 87–111.

[37] Jeffery, C. J. 2016. Protein species and moonlighting proteins: Very small changes in a protein's covalent structure can change its biochemical function. *Journal of Proteomics*, 134: 19–24.

[38] Katifori, E. and Magnasco, M. O. 2012. Quantifying loopy network architectures. *PLoS ONE*, 7(6): e37994.

[39] Katifori, E., Szöllosi, G. J., and Magnasco, M. O. 2010. Damage and fluctuations induce loops in optimal transport networks. *Physical Review Letters*, 104(4): 048704.

[40] Kramar, M., Goullet, A., Kondic, L., and Mischaikow, K. 2013. Persistence of force networks in compressed granular media. *Physical Review E - Statistical, Nonlinear, and Soft Matter Physics*, 87(4): 042207.

[41] Kramár, M., Goullet, A., Kondic, L., and Mischaikow, K. 2014. Quantifying force networks in particulate systems. *Physica D: Nonlinear Phenomena*, 283: 37–55.

[42] Light, S. H. and Anderson, W. F. 2013. The diversity of allosteric controls at the gateway to aromatic amino acid biosynthesis. *Protein Science*, 22(4): 395–404.

[43] Liu, A. J. and Nagel, S. R. 2010. The Jamming Transition and the Marginally Jammed Solid. *Annual Review of Condensed Matter Physics*, 1(1): 347–369.

[44] Mézard, M., Parisi, G., and Zecchina, R. 2002. Analytic and algorithmic solution of random satisfiability problems. *Science*, 297(5582): 812–815.

[45] Mileyko, Y., Edelsbrunner, H., Price, C. A., and Weitz, J. S. 2012. Hierarchical ordering of reticular networks. *PLoS ONE*, 7(6): e36715.

[46] Monod, J. and Jacob, F. 1961. Teleonomic mechanisms in cellular metabolism, growth, and differentiation. *Cold Spring Harbor symposia on quantitative biology*, 26: 389–401.

[47] Motlagh, H. N., Wrabl, J. O., Li, J., and Hilser, V. J. 2014. The ensemble nature of allostery. *Nature*, 508(7496): 331–339.

[48] Nickell, A. D., Wilcox, J. R., Lorenzen, L. L., *et al.* 2017. The Fap2 Locus in Soybean Maps to Linkage Group D. *Journal of Heredity*, 85(2): 160–162.

[49] Nobeli, I., Favia, A. D., and Thornton, J. M. 2009. Protein promiscuity and its implications for biotechnology. *Nature Biotechnology*, 27(2): 157–167.

[50] Nussinov, R. and Tsai, C. J. 2013. Allostery in disease and in drug discovery. *Cell*, 153(2): 293–305.

[51] O'Hern, C. S., Silbert, L. E., Liu, A. J., and Nagel, S. R. 2003. Jamming at zero temperature and zero applied stress: The epitome of disorder. *Physical Review E*, 68(1): 011306.

[52] Otter, N., Porter, M. A., Tillmann, U., Grindrod, P., and Harrington, H. A. 2017. A roadmap for the computation of persistent homology. *EPJ Data Science*, 6(1): 17.

[53] Pagani, G. A. and Aiello, M. 2013. The Power Grid as a complex network: A survey. *Physica A: Statistical Mechanics and its Applications*, 392(11): 2688–2700.

[54] Pellegrino, S. 1993. Structural computations with the singular value decomposition of the equilibrium matrix. *International Journal of Solids and Structures*, 30(21): 3025–3035.

[55] Pittermann, J. 2010. The evolution of water transport in plants: An integrated approach. *Geobiology*, 8(2): 112–139.

[56] Press, W. H., Teukolsky, S. A., Vetterling, W. T., and Flannery, B. P. 2007. *Numerical recipes: The art of scientific computing*. Cambridge University Press, 3rd edition.

[57] Redner, S. 2011. Fractal and Multifractal Scaling of Electrical Conduction in Random Resistor Networks. In R. A. Meyers, editor, *Mathematics of Complexity and Dynamical Systems*, pages 446–462. Springer, New York, New York, NY.

[58] Reid, D. R., Pashine, N., Wozniak, J. M., *et al.* 2017. Auxetic metamaterials from disordered networks. *Proceedings of the National Academy of Sciences of the United States of America*, 115(7): E1384–E1390.

[59] Ribeiro, A. A. and Ortiz, V. 2016. A Chemical Perspective on Allostery. *Chemical Reviews*, 116(11): 6488–6502.

[60] Robins, V., Wood, P. J., and Sheppard, A. P. 2011. Theory and algorithms for constructing discrete morse complexes from grayscale digital images. *IEEE Transactions on Pattern Analysis and Machine Intelligence*, 33(8): 1646–1658.

[61] Rocks, J. W., Pashine, N., Bischofberger, I., *et al.* 2016. Designing allostery-inspired response in mechanical networks. *Proc Natl Acad Sci*, 114(10): 2520–2525.

[62] Rocks, J. W., Ronellenfitsch, H., Liu, A. J., Nagel, S. R., and Katifori, E. 2019a. Limits of multifunctionality in tunable networks. *Proceedings of the National Academy of Sciences*.

[63] Rocks, J. W., Liu, A. J., and Katifori, E. 2019b. The topological basis of function in flow networks. *arXiv:1901.00822*.

[64] Roerdink, J. B. and Meijster, A. 2001. The Watershed Transform: Definitions, Algorithms and Parallelization Strategies. *Fundamenta Informaticae*, 41(8): 187–228.

[65] Roux, M. 2018. A Comparative Study of Divisive and Agglomerative Hierarchical Clustering Algorithms. *Journal of Classification*, 35(2): 345–366.

[66] Sack, L. and Scoffoni, C. 2013. Leaf venation: Structure, function, development, evolution, ecology and applications in the past, present and future. *New Phytologist*, 198(4): 983–1000.

[67] Schenk, M. and Guest, S. D. 2011. Origami Folding: A Structural Engineering Approach. In *Origami 5: Fifth International Meeting of Origami Science Mathematics and Education*, pages 291—-304, Boca Raton, FL. CRC Press.

[68] Schlessinger, J. 1986. Allosteric regulation of the epidermal growth factor receptor kinase. *Journal of Cell Biology*, 103(6): 2067–2072.

[69] Schwarz, J. M., Liu, A. J., and Chayes, L. Q. 2006. The onset of jamming as the sudden emergence of an infinite k-core cluster. *Europhysics Letters*, 73(4): 560–566.

[70] Sherman, J. and Morrison, W. J. 2007. Adjustment of an Inverse Matrix Corresponding to a Change in One Element of a Given Matrix. *The Annals of Mathematical Statistics*, 21(1): 124–127.

[71] Srivastava, A., Halevi, R. B., Veksler, A., and Granek, R. 2012. Tensorial elastic network model for protein dynamics: Integration of the anisotropic network model with bond-bending and twist elasticities. *Proteins: Structure, Function and Bioinformatics*, 80(12): 2692–2700.

[72] Sussman, D. M., Goodrich, C. P., and Liu, A. J. 2016. Spatial structure of states of self stress in jammed systems. *Soft Matter*, 12(17): 3982–3990.

[73] Tang, W. and Thorpe, M. F. 1987. Mapping between random central-force networks and random resistor networks. *Physical Review B*, 36(7): 3798–3804.

[74] Tero, A., Yumiki, K., Kobayashi, R., Saigusa, T., and Nakagaki, T. 2008. Flow-network adaptation in Physarum amoebae. *Theory in Biosciences*, 127(2): 89–94.

[75] Thorpe, M. F., Lei, M., Rader, A. J., Jacobs, D. J., and Kuhn, L. A. 2001. Protein flexibility and dynamics using constraint theory. *Journal of Molecular Graphics and Modelling*, 19(1): 60–69.

[76] Tsai, C.-J., del Sol, A., and Nussinov, R. 2008. Allostery: Absence of a Change in Shape Does Not Imply that Allostery Is Not at Play. *Journal of Molecular Biology*, 378(1): 1–11.

[77] Tuma, R. F., Durán, W. N., and Ley, K. 2008. *Handbook of Physiology: Microcirculation*. Academic Press, San Diego.

[78] Wahba, G. 1990. *Spline Models for Observational Data*. Society for Industrial and Applied Mathematics.

[79] Wan, L., Liao, J., and Zhu, X. 2008. CDPM: Finding and evaluating community structure in social networks. In *Lecture Notes in Computer Science (including subseries Lecture Notes in Artificial Intelligence and Lecture Notes in Bioinformatics)*, volume 5139 LNAI, pages 620–627. American Physical Society.

[80] Wilson, E. B. 1927. Probable Inference, the Law of Succession, and Statistical Inference. *Journal of the American Statistical Association*, 22(158): 209–212.

[81] Wu, F. and Huberman, B. A. 2004. Finding communities in linear time: A physics approach. In *European Physical Journal B*, volume 38, pages 331–338. Springer Berlin Heidelberg.

[82] Yan, L., Ravasio, R., Brito, C., and Wyart, M. 2016. Architecture and Co-Evolution of Allosteric Materials. *Proc Natl Acad Sci*.

[83] Yan, L., Ravasio, R., Brito, C., and Wyart, M. 2018. Principles for Optimal Cooperativity in Allosteric Materials. *Biophysical Journal*, 114(12): 2787–2798.

[84] Yuan, Y., Tam, M. F., Simplaceanu, V., and Ho, C. 2015. New Look at Hemoglobin Allostery. *Chemical Reviews*, 115(4): 1702–1724.

Appendix A

Mechanical signaling coordinates the embryonic heartbeat

Note: The following content is reproduced with minor revision from Ref. [6].

A.1 Introduction

The heart is a prime example of an active system with mechanical behavior – the heartbeat – that is robust and remarkably well coordinated. The fundamental contractile units of the heart are muscle cells called cardiac myocytes (CMs). Individual CMs coordinate their contractions through intercellular signaling, generating contractile wavefronts that propagate through the tissue to pump macroscopic volumes of fluid. When this organization breaks down, tissue-scale contractions cease and blood circulation stops. It has long been understood that this signal is electrical [24]: ions

pass from one cell to another through gap junctions [23], depolarizing the cell membrane and initiating a process that ultimately releases Ca^{2+} from intracellular stores, driving CM contraction. The potential difference between CMs drives ion transport through gap junctions into the next cell, thus propagating the signal. This electrical signaling cascade is responsible for the contractile wavefronts of the heartbeat in adults and has been assumed to regulate the heartbeat at all stages of development. Here we propose that the early embryonic heart does not follow this established electrical signaling mechanism, but may instead use mechanical signaling to coordinate and propagate its beat. In our picture, embryonic CMs are mechanically excitable: we postulate that sufficiently high strains trigger intracellular release of Ca^{2+} ions through a molecular mechanism that is not yet determined, leading to contraction. We denote this mechanically-driven release of Ca^{2+} ions and subsequent contraction as mechanical activation. This in turn strains neighboring CMs and induces additional contraction, resulting in a coordinating signal that is propagated mechanically rather than electrically.

Although embryonic CMs beat spontaneously [38, 36], they would contract with random phases in the absence of a coordinating signal. A number of studies have shown that embryonic, neonatal, and adult CMs are sensitive to mechanical cues [22, 13, 2, 18, 35]. Recently the role of mechanics was explored at the tissue scale through extracellular matrix (ECM) stiffening and softening of isolated avian embryonic hearts [26]. The speed and strain of the contractile wavefront were found to be strongly dependent upon the tissue stiffness, suggesting that the electrical signaling

picture is insufficient for the embryonic heart and that the stiffness of the matrix must be taken into account.

Here we show that mechanical signaling between CMs can explain stiffness-dependent contractile wavefront speed and strain via a nonlinear mechanical "reaction-diffusion" mechanism, in which sufficient strain on a CM causes it to "react" by triggering contraction and stress "diffuses" through the tissue. Few models of CM signaling in the heart include mechanics; of these, most assume instantaneous mechanical signal propagation [32, 34] and therefore do not exhibit strong stiffness dependence. Our model is related to a mechanical version [26, 20] of the fire-diffuse-fire model [9], which also fails to capture key stiffness-dependent features. We model the heart as tissue composed of active and passive components. We treat the active CMs as mechanically-excitable inclusions that contract when the local strain exceeds a threshold value. The surrounding ECM is treated as a passive elastic-fluid biphasic material. This simple mechanical signaling model quantitatively captures the stiffness dependence of contractile wavefront velocity and strain, as well as the strain of CMs cultured on hydrogels observed in Ref. [26].

We challenge the hypothesis underlying our model–that mechanical signaling coordinates the embryonic heart– by blocking gap junctions with 18-β-glycyrrhetinic acid (BGA). We find that embryonic hearts continue to beat, even at BGA concentrations 10-fold higher than those sufficient to stop the adult heartbeat in minutes, confirming our hypothesis. Finally, our model predicts a minimum matrix modulus necessary to support a steady-state mechanical wavefront. We show experimentally that this

value is consistent with the heart's stiffness when it first starts to beat. Thus the heart, the first functional organ in the embryo, begins to beat as soon as mechanical signaling can support propagating wavefronts.

Production of CMs from pluripotent stem cells has generated considerable interest in the factors that govern maturation of these cells to heart tissue [5] particularly for repair of adult heart damage. Mechanical determinants in this process remain poorly understood, although the role of mechanical cues is increasingly recognized in cell differentiation, proliferation, and morphogenesis [46, 50, 48, 12]. Our results here indicate that mechanics in the developing heart may be necessary to tissue-scale function during stem cell maturation and may have application to heart damage repair.

A.2 Physical model of cardiac mechanical signaling

The myocardium of the embryonic heart is composed primarily of mechanically-excitable CMs (that contract when activated) and the surrounding ECM. We treat CMs as elastic inclusions embedded in the ECM, in accord with recent experiments of CMs embedded in three dimensional hydrogels [40]. We ignore direct cell-cell mechanical coupling; experimental evidence indicates that stresses are transmitted primarily through cell-matrix adhesions rather than cell-cell contacts during development [27], likely due to the prevalence of cell-junction remodeling. In addition, collagenase treat-

ment indicates that ECM is the primary component of tissue structural integrity [26]. We find that a good approximation (see Fig. A.6) is to consider CMs as infinitesimal and arranged in a cubic array, spaced by $\Delta x = 10\mu$m (see Table A.1). We consider a three dimensional mechanical version of fire-diffuse-fire signaling. This requires capturing the physics of 1) activated CMs creating mechanical stress; 2) stress propagation between CMs; and 3) activation of quiescent CMs in response to mechanical stress in the ECM.

How activated CMs create stress. We use two models to characterize the eigenstrain, i.e. the strain of an active inclusion (CM) in the absence of external stresses. In the constant eigenstrain (CE) model, we assume that CMs contract with a fixed eigenstrain independent of ECM stiffness. In the saturating eigenstrain (SE) model, the eigenstrain increases linearly with Young's modulus E up to a stall stiffness E_s, and is independent of E for $E > E_s$ (see Fig. A.1A inset). This behavior is observed for embryonic and neonatal CMs cultured on hydrogels[22, 2, 18, 17] and has been studied theoretically [7].

The two models for the strain exerted by a CM when it contracts are

$$\begin{aligned} \epsilon^*_{ij} &= \epsilon^* f(E/E_s) Q_{ij}, \\ f_{\mathrm{CE}}(E/E_s) &= 1 \quad \forall E \\ f_{\mathrm{SE}}(E/E_s) &= \begin{cases} E/E_s & E < E_s \\ 1 & E \geq E_s \end{cases} \end{aligned} \tag{A.2.1}$$

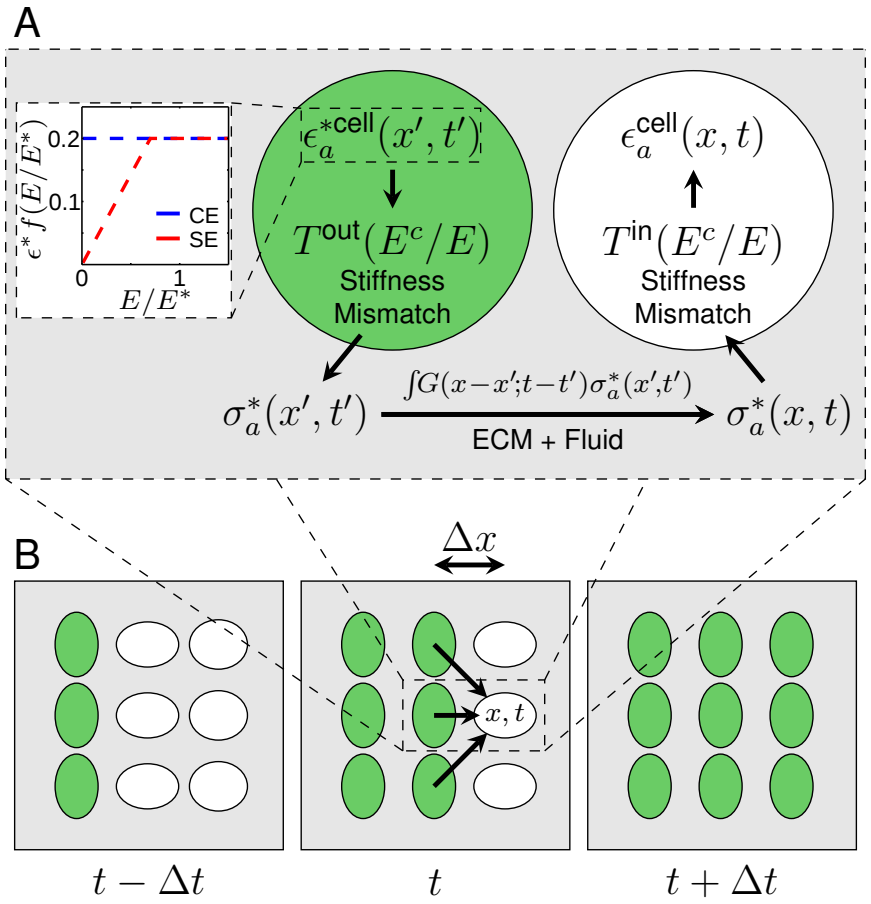

Figure A.1: Model for stress propagation in the myocardium. **(A)** Inset: CE and SE models as a function of ECM Young's modulus, which determines the strength of contraction (Eq. (A.2.1)). Main: The contracting CM (green) acts as a stress source for a quiescent CM (white). An activated cell a contracts with an eigenstrain $\epsilon^{*\text{cell}}_{a,ij}(x',t')$, locally inducing a stress $\sigma^*_{a,ij}(x',t')$ in the ECM that depends on the relative stiffness between the ECM and CMs. We capture these physics via the tensor T^{out}_{ijkl} in accordance with the Eshelby theory of elastic inclusions (see Supporting Information). This stress propagates according to the ECM response function $G_{ijkl}(x-x',t-t')$ (see Supporting Information). The matrix stress at (x,t) due to cell a is $\sigma_{a,ij}(x,t) = \int d^3x'dt'G_{ijkl}(x-x',t-t')\sigma^*_{a,kl}(x',t')$. This creates $\epsilon^{\text{cell}}_{a,ij}(x,t)$, the strain induced in the quiescent CM due to the contraction of a (modified by T^{in}_{ijkl}). **(B)** Sketch depicting quiescent (white) and activated (green) CMs in a traveling mechanical wavefront at subsequent activation times separated by Δt. Arrows represent stresses propagated through the ECM (not all shown) to a quiescent CM, which activates when $\epsilon^{\text{cell}}_{ii}(x,t) \geq \alpha$.

where Q_{ij} is the strain tensor representation of a uniaxial contraction in the x direction (see Supporting Information) and ϵ^* is the magnitude of the eigenstrain in the CE model or of the eigenstrain for $E > E_s$ in the SE model. See Fig. A.1A inset.

The eigenstrain ϵ^*_{kl} from the activated CM induces a stress in the matrix. In order to properly capture the physical effects of differences in stiffness between CMs and their surrounding ECM, we use Eshelby's theory of elastic inclusions [31**?**]. We compute the tensor $T^{\text{out}}_{ijkl}(E)$ which relates the CM eigenstrain to the stress it induces in the ECM, shown schematically in Fig. A.1A (see Supporing Information for detailed calculations). The resulting ECM stress source due to an activated CM takes the form

$$\sigma^*_{a,ij}(x,t) = T^{\text{out}}_{ijkl}\epsilon^*_{kl}\Theta(t-t_a)\Theta(\tau+t_a-t)\delta^3(x-x_a), \tag{A.2.2}$$

where $\Theta(t)$ is the Heaviside function.

How stress propagates between CMs. At the cellular length scale and CM contraction velocity scale, the Reynolds number is small ($\sim 10^{-5}$). We therefore model the ECM as an overdamped, incompressible biphasic material. See Table A.1 for parameter values. It is composed of a linear elastic mesh (with Young's modulus E and Poisson ratio $\nu = 0.4$ [19, 26]) and interstitial fluid (of viscosity η similar to water). The fluid and elastic components are coupled through incompressibility and a drag term Γ, an effect of matrix permeability to fluid. Similar approaches were used to model collagenous tissue [30] and active gels [1]. Using this model, we calculate the response function $G_{ijkl}(x,t)$ to describe propagation of mechanical stress within

the ECM (see Supporing Information).

How quiescent CMs are activated mechanically. We assume that when the strain on a quiescent CM exceeds threshold α ($\epsilon^{\text{cell}}_{kk}(x_q, t) \geq \alpha$), the CM is activated (it contracts). To describe this mathematically, we index noncontracting (quiescent) cells with q and contracting (active) cells with a. Each activated CM contracts for a physiologically relevant amount of time τ before deactivating and becoming refractory. We assume that the refractory timescale is longer than mechanical relaxation, allowing us to ignore back-propagation. Let us consider a CM at x_a which activated at time t_a. Then t_a is the moment when this CM's strain trace first crossed the strain activation threshold $\epsilon^{\text{cell}}_{kk}(x_a, t_a) = \alpha$, transforming the originally quiescent CM into an active one. The active CM contracts, creating an eigenstrain ϵ^*_{kl} (see Eq. (A.2.1)) for time $t_a < t < t_a + \tau$ which can be represented as a product of Heaviside functions.

To relate the strain on an embedded quiescent CM q at (x_q, t) due to local mechanical stress within the ECM, we compute the tensor $T^{\text{in}}_{ijkl}(E)$ (also shown schematically in Fig. A.1A) using elastic inclusion theory (see Supporting Information). The strain contribution on q from an activated CM a is then

$$\epsilon^{\text{cell}}_{a,ij}(x_q, t) = T^{\text{in}}_{ijkl} \int G_{klmn}(x_q - x'; t - t') \sigma^*_{a,mn}(x', t') \tag{A.2.3}$$

with $\sigma^*_{a,mn}(x', t')$ from Eq. (A.2.2). The total strain induced in q is the sum over the contribution from all activated cells $\epsilon^{\text{cell}}_{ij}(x_q, t) = \sum_a \epsilon^{\text{cell}}_{a,ij}(x_q, t)$.

Table A.1: Parameter symbols, references, and values

Parameter	Symbol	Value [fit/ref]
Mesh/fluid drag	Γ	0.4 mPa s / μm^2 [fit]
E4 myocardium modulus	E^*	1.6 kPa [26]
ECM Poisson ratio	ν	0.4 [19]
Fluid fraction (average)	ϕ	0.8 [45, 47]
Fluid viscosity (water 25°C)	η	0.89 mPa s
CM spacing	Δx	10 μm [26]
CM modulus	E^c	0.75 kPa [fit]
CM eigenstrain magnitude	ϵ^*	0.2 [13]
CM strain threshold	α	0.11 [fit]
CM Poisson ratio	ν^c	0.4 [19]
Contraction time (AP duration)	τ	250 ms

A.3 Results

A.3.1 Mechanical signaling model yields contractile wavefronts

From the model, we calculate the velocity of the propagating contractile wavefront as a function of matrix stiffness as follows. When a CM contracts, it creates a stress field $\sigma^*_{a,ij}$ in the ECM which can induce further contraction by activating quiescent CMs. If the activation process cascades through the tissue, the resulting contraction wavefront can attain a co-moving steady state $\epsilon_{ij}(x,t) = \epsilon_{ij}(x - vt)$ with velocity v. This is unsurprising since the model is a mechanical analog of nonlinear reaction-diffusion; such systems are well-known to exhibit propagating wavefront solutions. The activation condition $\epsilon^{\text{cell}}_{kk}(x,t) = \alpha$ with a co-moving steady state relates the wavefront velocity v to the model parameters through an algebraic relation (see Supporting Information). Once v is determined, we compute the maximal tissue strain

by coarse-grained solution of the waveform (see Supporting Information).

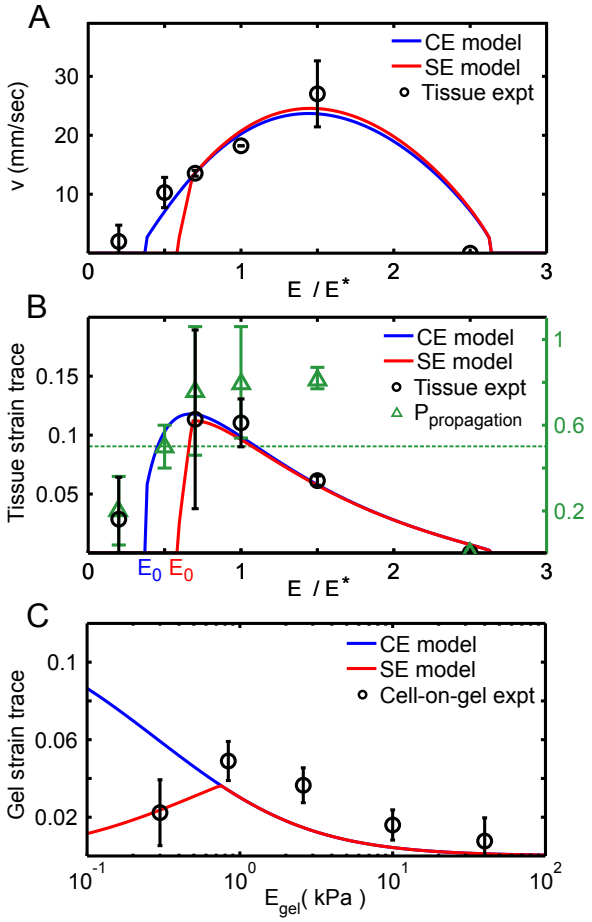

Figure A.2: Results from CE (blue) and SE (red) models (Eq. (A.2.1)) compared to experimental measurements (black) from Ref. [26]. **(A)** Best fits (Table A.1) of model contractile wavefront velocities to experimental data from the embryonic ventricle. **(B)**Maximal tissue strain as a function of E calculated with no additional fit parameters vs. experimental data (black circles). Green triangles denote likelihood that wavefront propagated across the entire ventricle in experiment; for the two lowest E/E^* data points, the likelihood falls below 50% (green dotted line), consistent with our models, which predict no stationary solutions below E_0. **(C)** Predicted induced strain trace for a single cell adhered to gel surface (see Supporting Information) compared to cell-on-gel data (black circles).

A.3.2 Mechanical signaling model fits experimental wavefront velocities with physiologically relevant parameters

We obtain most of the physiological parameter values from the literature (Table A.1). We treat CMs as elastic inclusions with Young's modulus E^c and with the same Poisson ratio as the surrounding tissue [19] and estimate CM eigenstrain magnitude to be $\epsilon^* = 0.2$ from intracellular embryonic CM principal strain measurements [13]. Stress saturation stiffness is estimated to be the cell modulus $E_s = E^c$ [22, 13]. Three model parameters could not be identified from the literature and are fit via nonlinear regression to wavefront velocity data from Ref. [26]. These three parameters are the mesh-fluid drag Γ, the CM activation threshold α, and the effective CM Young's modulus E^c. All three fit values (Table A.1) fall within physiologically sensible ranges. The resulting velocity is plotted against ventricle contraction velocity data (black circles, from Ref. [26]) of stiffness-modified E4 hearts in Fig. A.2A. No steady-state solution exists below stiffness E_0 (which differs between CE and SE models). Physically, E_0 arises because when the tissue is too soft, contracting CMs cannot provide enough strain to trigger additional contraction in quiescent CMs. This is consistent with a significantly reduced likelihood of wavefront propagation observed in experiment (green triangles in Fig. A.2B). Likewise, the wavefront velocity vanishes at high tissue stiffness, where the stiffness mismatch between CMs and the surrounding ECM prevents contracting CMs from exerting sufficient strain on the ECM to trigger contraction of quiescent cells.

A.3.3 Calculated wavefront strain agrees with experimental observations with no additional fitting parameters

Using the three parameters (Γ, α, E^c) fit from wavefront velocity data, we independently calculate the tissue strain of the contractile wavefront and compare to the measured maximal ventricular strain from Ref. [26] (Fig. A.2B). Both the CE (blue) and SE (red) models are in excellent quantitative agreement with the observed behavior (black circles) as a function of tissue stiffness, providing strong evidence in favor of our model. Note that the correct optimum stiffness naturally emerges from our model by treating CMs as elastic inclusions (see Supporting Information) embedded within a surrounding matrix of variable stiffness. This quantitative agreement is significant and nontrivial, as we can observe from the different values of E corresponding to optimum velocity and optimum strain in experiment and model. Note also that no purely electrochemical model can correctly predict strain as a function of stiffness.

A.3.4 Saturating eigenstrain (SE) model is consistent with cell-on-gel measurements with no additional fitting parameters

We further test our model by comparing to data for beating E4 CMs cultured on PAG where gel strain at cell edges was measured for varying gel stiffness [26]. We calculate the trace of the 2d projected strain by finite-element simulation (see Materials and Methods and Fig. A.5) using the fit E^c value and comparing to experiment in Fig. A.2C. The failure of the CE model on soft gels is expected from cultured CM

experiments [17, 2, 18]. Remarkably, we find agreement between the SE model with cell-on-gel measurements, demonstrating that we can deduce this single CM behavior as a function of E quantitatively from collective behavior in tissue.

A.3.5 Mechanical signaling model correctly predicts appearance of first heartbeats

The developing heart stiffens with age due to increased collagen in the ECM [26]. CMs begin periodic contractions at about 1.5 days after fertilization (E1.5). At that point, the heart does not beat but "shivers;" this shivering is similar to behavior observed in strain-activated contractile cell aggregates [16], which lack a signaling mechanism to coordinate the phases of the periodically-contracting cells. The first fully-coordinated beats do not occur until hours after CMs start contracting. Our model predicts that coordinated beats cannot appear until the matrix reaches the minimum stiffness E_0 (see Fig. A.2A). Here we ask whether the predicted value of E_0 coincides with heart stiffness at the onset of beating.

We measure embryonic chick hearts stiffnesses at Hamburger-Hamilton (HH) stages 10 and 11 (E1.5-2) via micropipette aspiration (see Materials and Methods). Early Stage 10 does not exhibit fully coordinated beats while Stage 11 exhibits full-tissue contraction (see Video A.12). At the strains applied, the tissue behaves as a standard linear solid (see Fig. A.7).

We sort the measured stiffnesses depending on whether or not the hearts exhibit

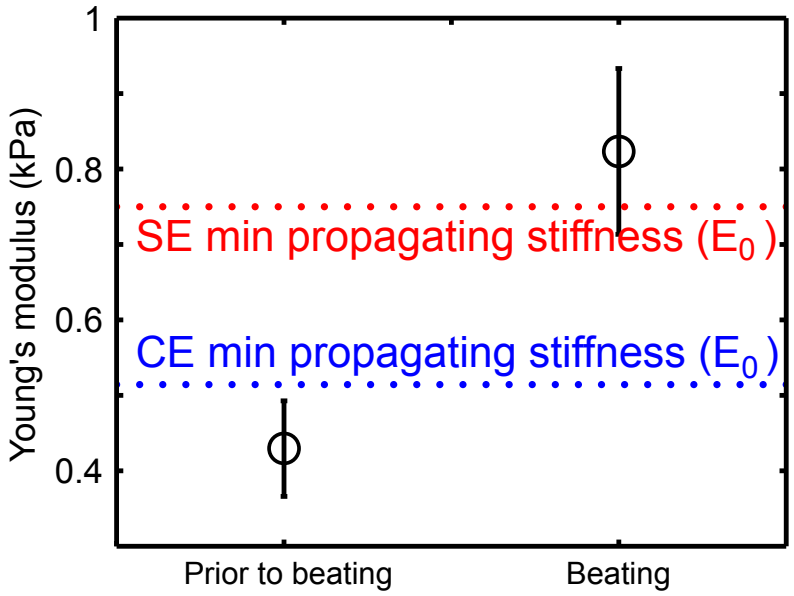

Figure A.3: Measurements of heart stiffness before and after the appearance of heartbeats, compared to minimum stiffness necessary to support a mechanically-coordinated contraction in our model. Stiffness is measured via micropipette aspiration for six Hamburger-Hamilton (HH) stage 10 and five HH stage 11 hearts, corresponding to embryonic days E1.5-2 (see Materials and Methods). Dashed lines indicate predicted E_0 values for the CE (blue) and SE (red) models, corresponding to the lower-stiffness cutoffs shown in Fig. A.2A.

coordinated contractions (black circles in Fig. A.3). The pre-beating stiffness is just above that of the undifferentiated embryonic disc [26], suggesting that the first stage of heart development involves some differentiation with little stiffening. The minimum stiffnesses E_0 for the CE (blue) and SE (red) models both fall between the measured pre- and post- beating values. These measurements are consistent with our model prediction and suggest that heartbeats may initially emerge once the tissue becomes stiff enough to support mechanically-activated wavefronts.

A.3.6 Conduction interference experiments are consistent with mechanically-coordinated heartbeats

Gap junctions are critical for electrical coordination of adult heartbeats. Our mechanical signaling hypothesis implies that blocking electrical signaling should not impede the embryonic heartbeat. We therefore test our hypothesis by blocking electrical signaling through pharmacological interference of gap junctions.

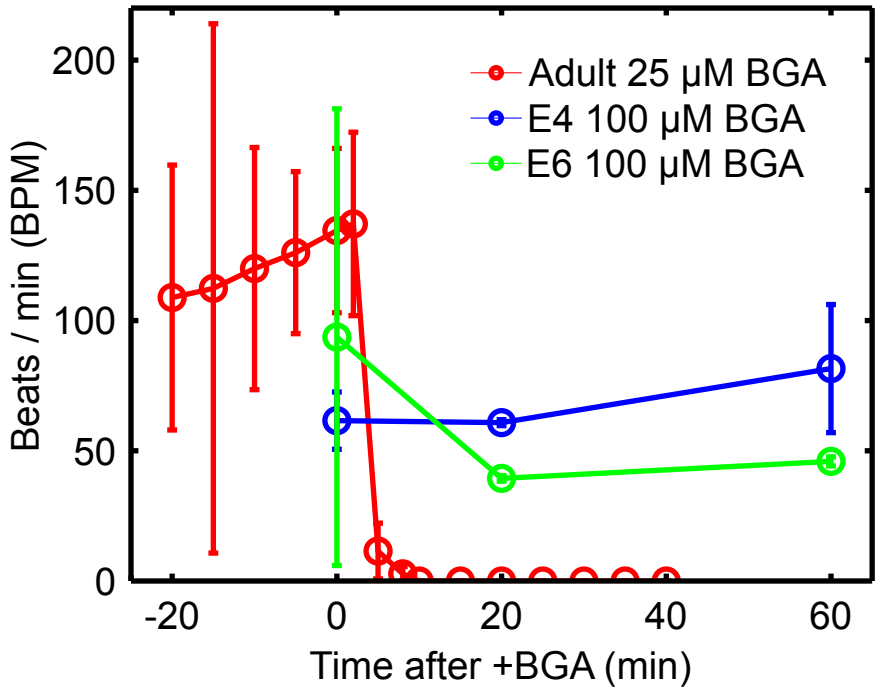

Figure A.4: Conduction interference results for isolated hearts from 3 murine adults and 4 chick embryos. Gap junctions are disrupted by perfusing intact adult (red) and embryonic E4 and E6 (blue and green respectively) hearts with β-glycyrrhetinic acid (BGA). Heart functionality is quantified by beats per minute (BPM). Adult hearts stop beating after $\sim$10 minutes at 25μM BGA (see Video A.13). Embryonic hearts perfused at higher 100 μM show little to no effect after an hour. See Fig. A.8 for adult heart BPM controls and Fig. A.9 for control experiments on embryonic heart BGA perfusion.

We perfuse isolated adult and embryonic hearts with BGA, a non-specific gap junc-

tion blocker known to inhibit inter-cellular ion transport between embryonic chick epithelial cells at 10 μM [25] and in rat, frog, mouse and human systems [4, 39, 51, 8]. We also validated its effect in embryonic hearts via fluorescence recovery after photobleaching (FRAP) experiments and found that BGA treatment reduced intercellular diffusion (see Supporting Information and Fig. A.9). Adult hearts stopped beating within 10 min post-treatment at 25μM BGA. However, the embryonic heartbeat was unaffected for 1 hr even at 100 μM BGA (Fig. A.4), and was robust even when subjected to 250μM for an additional hour. This experiment demonstrates that embryonic CMs can coordinate their contractions without functional gap junctions needed to support electrical signaling, supporting our hypothesis of mechanically coordinated CMs in the early heart. See Materials and Methods.

A.4 Discussion

A.4.1 Mechanical signaling robustly explains strong dependence of wavefront velocity and strain on stiffness

Tissue stiffness is a mechanical property that cells can sense. A strong dependence on tissue stiffness is an indicator of cell response to mechanical cues. Our model combines elasticity with simple mechanical activation of cardiac myocytes, using a minimum of assumptions and adjustable parameters, and yet captures multiple observed cell- and tissue-scale phenomena quantitatively.

Our model is robust to noise: the predicted strain threshold α requires several nearest neighbor contractions in order to trigger activation. As a result, a rogue contraction cannot set off a wavefront. Our results are also robust to how we incorporate mechanosensitivity. We considered a model variant in which the CM contracts with a probability $p(\epsilon_{kk})$ that increases with strain, and found similar stiffness dependence of the contractile wavefront. This stochastic activation model corresponds mathematically to stochastic pulse-coupled oscillator (SPCO) models of neural networks [11], but with an additional spatially-dependent phase set by mechanical reaction-diffusion. Synchronized states in SPCO models map onto steady-state wavefronts of our stochastic model.

We note that embryonic CMs spontaneously contract in periodic manner [38, 36]. In the beating embryonic heart, the wavefront is initiated at the atrial end of the heart tube by CMs which contract at a higher frequency. Our model describes the nonlinear propagating wavefront emanating from each contraction of these atrial CMs which activates other CMs. An alternate but equivalent description is to consider the coordination of CMs as non-linear oscillators coupled through the ECM. Because the ECM has a viscous fluid component as well as an elastic component, this coupling does not lead to synchronization, as typical for phase-coupled biological oscillators [29], but to a propagating wavefront.

A.4.2 Mechanical signaling is consistent with known mechanosensitivity of cardiac myocytes

There is solid evidence that stretch can trigger contraction of CMs. External tissue-scale stretch of the heart triggers arrhythmic beats [41]. Healthy adult rat CMs exhibit increased intracellular calcium release events under 8% strain [21], while diseased adult myocytes demonstrate direct mechano-chemotransduction through full intracellular calcium release [35]. Mechanical stimulation of the substrate in cultured embryonic chick CMs with 6% stretch excites quiescent myocytes [42]. Mechanical stress exerted by fibroblasts affects the wavefront velocity of neonatal rat CMs [43, 44], and neonatal and adult rat CMs cultured in similar conditions exhibit mechanical stimulation and entrainment [33]. In some of these experiments, it is known that stretch-induced activation involves cardiac ryanodine receptors [35].

A.4.3 Mechanical vs. electrical signaling in the developing heart

There is evidence in the literature that electrical conduction may not be fully functional in the early heart. When whole-tissue contractions first appear, the cardiac conduction system is not yet identifiable [28]. Embryonic chick hearts exhibit low levels of the primary cardiovascular gap junction protein, Connexin43 (Cx43), and the small amounts present are distributed uniformly through the cytosol until trabeculation occurs [10, 49]. Other studies find that in post-hatch and adult chick, the primary

ventricle myocardial gap junction is Cx42. However Cx42 appears to be absent in working myocytes and cardiac conduction tissues until E9-11, leading to speculation that CMs may not be electrically coupled by gap junctions during embryogenesis [14]. Primary markers of the conduction system do not appear definitively until E9-E15 [15].

In conjunction with our results, such observations suggest that the heart may switch from mechanical to electrical signaling as it matures. We speculate that mechanically-coordinated heartbeats may assist in organizing the heart: myocytes seeking to maximize contractile activity will align with each other [3] and cyclic stretch of neonatal rat ventricular myocytes was found to polarize gap junction localization [37]. Perhaps current limitations in producing fully mature CMs from stem cells [5] reflect an incomplete understanding of the role of mechanics in heart development.

It is possible that mechanical signaling prevails in early development because it is robust. Electrical coupling requires gap junctions, which may be difficult to maintain as CMs proliferate and rearrange in the rapidly growing heart. Mechanical signals, on the other hand, are inevitably present because CMs must exert stresses on their surroundings when they contract. However, electrical signaling is easier to regulate when the heart develops more complicated structure.

In summary, the highly sophisticated electrical conduction system that precisely regulates the adult heart has been assumed to coordinate every heartbeat, from the first to the last. Here we employ a biophysical theory, bolstered by experiment, to pro-

pose that mechanical—not electrical—signaling is responsible for coordinating early heartbeats. If further verified, this idea could transform the way we think about how the heart develops and functions.

A.5 Materials and Methods

Model details We solve the matrix response function in three dimensions. We assume a stationary constant-velocity wavefront ($\epsilon_{ij}(x,t) = \epsilon_{ij}(x - vt)$) within a cubic array of active sites. Self-consistency of the activation condition with the time between activation events relates v to model parameters. See Supporting Information.

Numerical computations and data analysis Numerical computations were performed in C/C++ and MATLAB. Data analysis and nonlinear least-squares parameter fitting was done in MATLAB with custom subroutines.

Finite element simulation Linear elastic finite element simulations were performed in MATLAB and COMSOL. Cell-on-gel culture was modeled as a hemisphere adhered to a substrate. See Supporting Information.

Myocardium stiffness measurements Embryonic hearts were isolated as described in [26]. Aspiration was performed at room temperature. See Supporting Information.

Conduction interference: embryonic hearts Embryonic chick hearts were isolated as in [26] and incubated in heart medium at 37 (alpha-MEM supplemented with 10% FBS and 1% penn-strep, Gibco, 12571?063) for at least 2 hrs before drug treatment. Desired concentrations of 18-β-glycyrrhetinic acid (Cayman Chemical, 11845)

and blebbistatin (EMD Millipore, 203390) were prepared by diluting in heart culture medium (with or without 105 FBS) and DMSO, respectively. Isolated hearts were then treated with BGA or blebbistatin by aspirating out the medium and perfusing the hearts in the prepared drug solutions. E4 hearts were imaged using an Olympus I81 microscope and recorded for a minimum of 15 seconds using a CCD camera at 21 frames/sec. E6 hearts were imaged using a Nikon SMZ1500 microscope. Analysis was performed in ImageJ by tracking morphological parameters over 10-15 sec intervals.

Conduction interference: adult hearts Adult (8-12 week) C57/BL6 mice were anesthetized by induction in an isofluorane chamber, followed by thoracotomy and excision of the heart. Isolated hearts were suspended from a Langendorff perfusion column via cannulation of the aorta and perfused with an oxygenated heart medium at 37C. Under control conditions, hearts cannulated via this method generate intrinsic rhythm and maintain rhythmic beating for over 3 hours. BGA solution was prepared by dilution in medium and DMSO. After ensuring 20 minutes of rhythmic beating, the medium was exchanged for BGA-prepped solution. 20-second video acquisitions were acquired every 3-5 minutes to analyze changes in heart rate over time. Experiments were terminated if the heart stopped beating for more than 10 minutes. Video segments from different time points were randomized and analyzed blindly to determine BPM from 20-second intervals.

A.6 Supporting Information

Abbreviations: CM, cardiomyocytes; ECM, extracellular matrix; BGA, 18-β-glycyrrhetinic acid; CE, constant eigenstrain; SE, saturating eigenstrain

A.6.1 Linearized biphasic model

In the linearized biphasic model composed of fluid and elastic mesh, we assume that the fluid and elastic components mutually exclude each other and that the total volume is fixed. Then for a infinitesimal volume element at x, if the fluid volume fraction is ϕ the elastic mesh must occupy $1-\phi$. As a result, within the volume element at x neither fluid nor mesh network satisfy the regular incompressible condition, since fluid and mesh mutually displace each other. In our model, we take into account the fluid dynamic viscosity, mesh elasticity, fluid-mesh drag coupling, and the total volume (fluid + mesh) constraint to linear order in the dynamic variables:

$$\begin{aligned}
\Gamma\left(\dot{u}_i - v_i\right) &= \frac{E}{2(1+\nu)}\left[\partial^2 u_i + \frac{1}{1-2\nu}\partial_i\partial_j u_j\right] - (1-\phi)\partial_i p \\
\Gamma\left(v_i - \dot{u}_i\right) &= \eta\left[\partial^2 v_i + \frac{1}{3}\partial_i\partial_j v_j\right] - \phi\partial_i p \\
0 &= (1-\phi)\partial_i\dot{u}_i + \phi\partial_i v_i.
\end{aligned} \tag{A.6.1}$$

Since we are interested primarily in comparing to experimental wavefront speeds and tissue strain trace, for brevity we detail only the strain trace and strain rate trace equations here. The fluid and solid (traces of) strain rates and strain are $\dot{\epsilon}_{f,ii} = \partial_i v_i$,

$\dot{\epsilon}_{s,ii} = \partial_i \dot{u}_i$, and $\epsilon_{s,ii} = \partial_i u_i$. For physiological values of $\phi \approx 0.8$ in muscle tissue (Table 1), we solve the equations:

$$\begin{aligned} \Gamma\left(\dot{\epsilon}_s - \dot{\epsilon}_f\right) &= \frac{E(1-\nu)}{(1+\nu)(1-2\nu)}\partial^2\epsilon_s - (1-\phi)\partial^2 p \\ \Gamma\left(\dot{\epsilon}_f - \dot{\epsilon}_s\right) &= \frac{4}{3}\eta\partial^2\dot{\epsilon}_f - \phi\partial^2 p \\ \dot{\epsilon}_f &= -\dot{\epsilon}_s\frac{1-\phi}{\phi}. \end{aligned} \tag{A.6.2}$$

Then solving in terms of ϵ_s, we obtain the equation of motion

$$\left[\dot{\epsilon}_s - \frac{4(1-\phi)^2\eta}{3\Gamma}\partial^2\dot{\epsilon}_s\right] = D\partial^2\epsilon_s \tag{A.6.3}$$

where $D = \phi^2 E(1-\nu)/(\Gamma(1+\nu)(1-2\nu))$. We assume that the interstitial fluid viscosity is approximately the viscosity of water at body temperature. Best fits (see Results) then indicate that $\Gamma \approx 45\frac{\eta}{\Delta x^2}$ where Δx the spacing between myocytes. As a result, the fluid-mesh drag Γ is dominant over fluid viscosity at physical length scales of interest, and the second term on the left hand side in Eq. (A.6.3) can be dropped. This result is used throughout the text. For our parameter values, the linearized equations are stable to perturbations at the onset of propagation. In contrast to standard reaction-diffusion models, but consistent with fire-diffuse-fire [9] models, the nonlinear character of transitions between the non-propagating and propagating phases is a result of threshold activation and as a result is not captured by linear stability analysis.

A.6.2 Induced strain of Eshelby inclusions

Here we detail the stresses induced by CMs, which are treated as spherical Eshelby inclusions (elastic inclusions with elastic constants that may be different from the surrounding matrix). We compute two tensors, T^{out}_{ijkl} and T^{in}_{ijkl} which correspond (respectively) to strain induced in the matrix due to an active inclusion, and the strain felt by a passive inclusion due to strain in the matrix (see Fig. A.1A). Since we model CM sources as infinitesimal, incoming stresses are treated as far-field. Note that we have checked this approximation using finite-element calculations (see Supplemental Methods, CMs-in-matrix FEM simulations and Fig. A.6), and find that it is quantitatively quite accurate. We also assume that near an excited inclusion the matrix responds quickly; this allows us to make use of the static Eshelby tensor.

Suppose a cell, represented as an ellipsoidal inclusion with stiffness tensor C_{ijkl}, is embedded in an infinite bulk medium (i.e. the tissue) with the same stiffness tensor. Although we use the general form, in the isotropic case this tensor is determined by just two independent parameters, which we call the Young's modulus E and Poisson ratio ν in the main text. Suppose the cell contracts uniformly throughout its volume with an eigenstress $\sigma^{*\text{cell}}_{ij}$. We equivalently represent this contraction strength as an eigenstrain $\epsilon^{*\text{cell}}_{ij}$, related to the stress by $\sigma^{*cell}_{ij} = C_{ijkl}\epsilon^{*\text{cell}}_{kl}$. This eigenstrain can be thought of as how much the cell would strain if the surroundings exerted no stress on the cell. By Eshelby inclusion theory, the observed strain of an embedded inclusion

is related to the eigenstrain by

$$\epsilon^*_{ij} = S_{ijkl}\epsilon^{*\text{cell}}_{kl} \tag{A.6.4}$$

where S_{ijkl} is the Eshelby tensor [31]. For a spherical inclusion, this tensor is uniform and given by

$$S_{ijkl} = \frac{1+\nu}{3(1-\nu)}|v^1\rangle_{ijkl} + \frac{2(4-5\nu)}{15(1-\nu)}|v^2\rangle_{ijkl} \tag{A.6.5}$$

where $|v^1\rangle_{ijkl}$ and $|v^2\rangle_{ijkl}$ are defined for convenience as

$$\begin{aligned} |v^1\rangle_{ijkl} &= \frac{1}{3}\delta_{ij}\delta_{kl} \\ |v^2\rangle_{ijkl} &= \frac{1}{2}\left[\delta_{ik}\delta_{jl} + \delta_{il}\delta_{jk} - \frac{2}{3}\delta_{ij}\delta_{kl}\right] \end{aligned} \tag{A.6.6}$$

Stress locally induced in matrix by Eshelby inclusion

Now suppose the cell and tissue have different stiffness tensors C^c_{ijkl} and C_{ijkl} respectively. As before, an isotropic medium reduces the independent parameters to E and ν. Assume the cell contracts with a stress $\sigma^{*cell}_{ij} = C^c_{ijkl}\epsilon^{*\text{cell}}_{kl}$. The total stress inside the cell embedded in the tissue is related to the strain by

$$\sigma^T_{ij} = C^{\text{c}}_{ijkl}(\epsilon^*_{kl} - \epsilon^{*\text{cell}}_{kl}) \tag{A.6.7}$$

By superposition, we can map this to a problem to the Eshelby tensor for a homogeneous material with an additional strain source [31]. This is done by imposing an effective strain source in the cell $\epsilon_{ij}^{*\text{eff}}$ such that we get identical stresses and strains as the inhomogeneous problem. The stress-strain relation then becomes

$$\sigma_{ij}^{T} = C_{ijkl}(\epsilon_{kl}^{*} - \epsilon_{kl}^{*\text{eff}}) \tag{A.6.8}$$

Note that the effective strain source $\epsilon_{ij}^{*\text{eff}}$ does not actually exist, but is just a mathematical trick to reduce the inhomogeneous inclusion problem to the previously solved homogeneous inclusion problem. Eshelby's solution now tells us that the strain experienced in the cell embedded in the tissue is

$$\epsilon_{ij}^{*} = S_{ijkl}\epsilon_{kl}^{*\text{eff}} \tag{A.6.9}$$

with the Eshelby tensor calculated using C_{ijkl}. Now we calculate the effective source $\epsilon_{ij}^{*\text{eff}}$ by equating Eqs. (A.6.7) and (A.6.8), to identify the (actual) inhomogeneous case with the (constructed) homogeneous problem.

$$C_{ijkl}^{c}(\epsilon_{kl}^{*} - \epsilon_{kl}^{*\text{cell}}) = C_{ijkl}(\epsilon_{kl}^{*} - \epsilon_{kl}^{*\text{eff}}) \tag{A.6.10}$$

Substituting in Eq. (A.6.9), we get an equation for $\epsilon_{ij}^{*\text{eff}}$,

$$\left[\left(C_{ijkl}^{c} - C_{ijkl}\right)S_{klmn} + C_{ijmn}\right]\epsilon_{mn}^{*\text{eff}} = C_{ijkl}^{c}\epsilon_{kl}^{*\text{cell}} \tag{A.6.11}$$

Solving for $\epsilon_{ij}^{*\text{eff}}$ in terms of $\epsilon_{ij}^{*\text{cell}}$, we find ϵ_{ij}^{*} (via Eq. (A.6.9)). We can now calculate the stress source in the homogeneous case $\sigma_{ij}^{*} = C_{ijkl}\epsilon_{kl}^{*}$. We define the tensor T_{ijkl}^{out} to relate this stress to our cell strain source,

$$\sigma_{ij}^{*} = T_{ijkl}^{\text{out}}\epsilon_{kl}^{*\text{cell}} \tag{A.6.12}$$

as in Fig. 1A. For a spherical inclusion and isotropic matrix with Young's moduli E^c and E and Poisson ratios ν^c and ν respectively,

$$\begin{aligned} T_{ijkl}^{\text{out}} &= \left[\frac{\frac{E}{(1-2\nu)}\frac{(1-\nu)}{(1+\nu)}}{1+2\frac{(1-2\nu^c)}{(1+\nu)}\frac{E}{E^c}}\right]|v^1\rangle_{ijkl} + \left[\frac{\frac{15E}{4(1+\nu)}\frac{(1-\nu)}{(4-5\nu)}}{1+\frac{1}{2}\frac{(7-5\nu)}{(4-5\nu)}\frac{(1+\nu^c)}{(1+\nu)}\frac{E}{E^c}}\right]|v^2\rangle_{ijkl} \\ &= \frac{E}{3(1-2\nu)}T_1^{\text{out}}|v^1\rangle_{ijkl} + \frac{E}{2(1+\nu)}T_2^{\text{out}}|v^2\rangle_{ijkl} \end{aligned} \tag{A.6.13}$$

where T_1^{out} and T_2^{out} are dimensionless quantities, with pre-factors of the tissue bulk and shear moduli.

Stress induced in Eshelby inclusion by uniform stress in matrix

As in the previous section, we can likewise compute the strain in a cell given some homogeneous stress $\sigma_{ij} = C_{ijkl}\epsilon_{kl}$ throughout the neighborhood of tissue surrounding the inclusion. The primary difference is that this system now exists under a pre-stress condition without a cell source. As before, cell and tissue stiffness tensors are C_{ijkl}^{c}

and C_{ijkl}. The total stress inside the cell is given by

$$\sigma_{ij}^T = C_{ijkl}^c \epsilon_{kl}^{\text{cell}} \tag{A.6.14}$$

By linearity, the strain in the cell can be broken up into two components: the homogeneous strain in the surrounding tissue ϵ_{ij}, and the effects of the inclusion's stiffness mismatch with the tissue ϵ_{ij}^I,

$$\epsilon_{ij}^{\text{cell}} = \epsilon_{ij} + \epsilon_{ij}^I \tag{A.6.15}$$

As in the previous section, we map this inhomogeneous problem to a homogeneous one with additional cell strain source $\epsilon_{ij}^{*\text{eff}}$, but the same total stress and strain

$$\sigma_{ij}^T = C_{ijkl}(\epsilon_{kl}^{\text{cell}} - \epsilon_{kl}^{*\text{eff}}). \tag{A.6.16}$$

Eshelby's solution now tells us that the contribution to the strain from the inclusion is

$$\epsilon_{ij}^I = S_{ijkl}\epsilon_{kl}^{*\text{eff}}. \tag{A.6.17}$$

Equating Eqs. (A.6.14) and (A.6.16) and using the relation from Eq. (A.6.15),

$$C_{ijkl}^c(\epsilon_{kl} + \epsilon_{kl}^I) = C_{ijkl}(\epsilon_{kl} + \epsilon_{kl}^I - \epsilon_{kl}^{*\text{eff}}). \tag{A.6.18}$$

Substituting in Eq. (A.6.17), we get an equation for $\epsilon_{ij}^{*\text{eff}}$,

$$\left[\left(C_{ijkl}^{c} - C_{ijkl}\right)S_{klmn} + C_{ijmn}\right]\epsilon_{mn}^{*\text{eff}} = \left(C_{ijkl} - C_{ijkl}^{c}\right)\epsilon_{kl} \tag{A.6.19}$$

Solving for $\epsilon_{ij}^{*\text{eff}}$ in terms of ϵ_{ij}, we find ϵ_{ij}^{I} via Eq. (A.6.17). This gives the cell strain $\epsilon_{ij}^{\text{cell}}$. Using the relation $\sigma_{ij} = C_{ijkl}\epsilon_{kl}$ for the homogeneous case, we express $\epsilon_{ij}^{\text{cell}}$ in terms of σ_{ij}. We define T_{ijkl}^{in} to relate this stress to the strain in the cell

$$\epsilon_{ij}^{\text{cell}} = T_{ijkl}^{\text{in}}\sigma_{kl} \tag{A.6.20}$$

as in Fig. 1A. For a spherical inclusion and isotropic matrix with Young's moduli E^c and E and Poisson ratios ν^c and ν,

$$\begin{aligned} T_{ijkl}^{\text{in}} &= \frac{3(1-2\nu)}{E}\left[1 + \frac{\frac{(1-2\nu^c)}{(1-2\nu)}\frac{E}{E^c} - 1}{1 + 2\frac{(1-2\nu^c)}{(1+\nu)}\frac{E}{E^c}}\right]|v^1\rangle_{ijkl} + \frac{2(1+\nu)}{E}\left[1 + \frac{\frac{(1+\nu^c)}{(1-\nu)}\frac{E}{E^c} - 1}{1 + \frac{1}{2}\frac{(7-5\nu)}{(4-5\nu)}\frac{(1+\nu^c)}{(1+\nu)}\frac{E}{E^c}}\right]|v^2\rangle_{ijkl} \\ &= \frac{3(1-2\nu)}{E}T_1^{\text{in}}|v^1\rangle_{ijkl} + \frac{2(1+\nu)}{E}T_2^{\text{in}}|v^2\rangle_{ijkl} \end{aligned} \tag{A.6.21}$$

where T_1^{in} and T_2^{in} are dimensionless quantities, with pre-factors of the inverse tissue bulk and shear moduli.

A.6.3 Activation condition

In our model, when CMs contract they generate an eigenstress corresponding to a negative force-dipole in the x direction. This assumption is based on the observation that E4 cardiac myocytes exhibit striations, which polarize contraction, and serves to simplify analysis. An activated CM in our model has an eigenstrain ϵ^*_{kl} and induces a matrix stress σ^*_{ij}:

$$\epsilon^*_{kl} = \epsilon^* \begin{pmatrix} -1 & 0 & 0 \\ 0 & \nu^c & 0 \\ 0 & 0 & \nu^c \end{pmatrix}, \sigma^*_{ij} = T^{\text{out}}_{ijkl}\epsilon^*_{kl}. \tag{A.6.22}$$

Given a stress source $\sigma^*_{a,kl}(r',t')$ indexed by a in the biphasic medium, the strain trace induced in an included cell at (r,t) is

$$\epsilon^{\text{cell}}_{a,ii}(r,t) = \frac{1-2\nu}{E} T_1^{\text{in}} \int dt' d^3r' G_{iikl}(r-r';t-t')\sigma^*_{a,kl}(r',t') \tag{A.6.23}$$

for the Green's function G_{ijkl}. Combining Eqs. (A.6.12) and (A.2.2),

$$\sigma^*_{a,ij}(r',t') = T^{\text{out}}_{ijkl}\epsilon^{*\text{cell}}_{a,kl}(r',t') = T^{\text{out}}_{ijkl}\epsilon^*_{kl}\Theta(t-t_a)\Theta(\tau+t_a-t)\delta^3(x-x_a). \tag{A.6.24}$$

For a quiescent cell at (r,t) to reach the activation threshold α, we consider all activated CMs (indexed here by a) as contributing to the local strain. This requires

$$\epsilon_{ii}^{\text{cell}}(r,t) = \sum_a \epsilon_{a,ii}^{\text{cell}}(r,t) = \alpha. \tag{A.6.25}$$

Consider a steady-state wavefront traveling in the x direction through a cubic array of CMs spaced by Δx as in Fig. A.1. We label each CM with lattice indices $[n^x, n^y, n^z]$. Steady state assumes CMs with the same x coordinate activate simultaneously with a constant (but unknown) time interval Δt between activations at neighboring sites (x,y,z) and $(x+\Delta x, y, z)$.

We express the activation positions and times as $r_a = [n_a^x, n_a^y, n_a^z]^T \Delta x$ and $t_a = n_a^x \Delta t$ where the index n^x is in the propagation direction x. In conjunction with the activation condition (Eq. (A.2.3)),

$$\begin{aligned}\frac{E\sum_a \epsilon_{a,ii}^{\text{cell}}}{(1-2\nu)T_1^{\text{in}}} &= \sum_a \int dt' d^3r' G_{iikl}(r-r';t-t')\sigma_{a,kl}^*(r',t') \\ &= \sum_{n^x,n^y,n^z} \int dt' G_{iikl}(r - \begin{bmatrix} n^x \\ n^y \\ n^z \end{bmatrix} \Delta x; t-t') \left[\Theta(t'-n^x\Delta t) - \Theta(t'-n^x\Delta t-\tau)\right] T_{klmn}^{\text{out}} \epsilon_{mn}^*\end{aligned} \tag{A.6.26}$$

for $n^x \in \{1,2,\ldots,\infty\}$ and $n^y, n^z \in \{-\infty,\ldots,-1,0,1,\ldots,\infty\}$ and the activation eigenstrain ϵ_{mn}^* as defined in main text Eq. (A.2.1). Using the Green's function

$G_{ijkl}(r,t)$ for Eq. (A.6.3), we find that the response to a Heaviside point force dipole $\sim \delta^3(r)\Theta(t)$ is

$$
\begin{aligned}
H_{iikl}(r,t) &= \int dt' G_{iikl}(r,t-t')\Theta(t') = \frac{1}{4\pi\Gamma D r^3}\left[H_1(r,t)\delta_{kl} + H_2(r,t)\frac{r_k r_l}{r^2}\right]\Theta(t), \\
H_1 &= \mathrm{erfc}\left(\frac{\mathrm{r}}{\sqrt{4\mathrm{Dt}}}\right) + \frac{2r}{\sqrt{4\pi D t}} e^{-\frac{r^2}{4Dt}} \\
H_2 &= -3\mathrm{erfc}\left(\frac{\mathrm{r}}{\sqrt{4\mathrm{Dt}}}\right) - \left(\frac{6r}{\sqrt{4\pi D t}} + \frac{4r^2}{4\pi D t}\right) e^{-\frac{r^2}{4Dt}}
\end{aligned}
\tag{A.6.27}
$$

in the limit where $\Gamma \gg \eta q^2$. Here $D = \phi^2 E(1-\nu)/(\Gamma(1+\nu)(1-2\nu))$ as before. Combining equations (A.6.25) - (A.6.27), we find a transcendental relation for Δt in terms of CM and ECM parameters:

$$
\frac{E\alpha}{1-2\nu} = T_1^{\mathrm{in}} \sum_a (H_{iikl}(r-r_a; t-t_a) - H_{iikl}(r-r_a; t-t_a-\tau) T^{\mathrm{out}}_{klmn} \epsilon^*_{mn}. \tag{A.6.28}
$$

We truncate the sum when the estimated relative error $\delta < 10^{-4}$ which corresponds to $|m|, |n|, |o| < 20$ for physiological parameters. We use Newton-Raphson to solve numerically for Δt to obtain the steady-state wave-front velocity, $v = \Delta x/\Delta t$. The cubic lattice approximation was chosen due to its simple analytic solution. We found that the steady-state wavefront behavior depends primarily on average spacing between active sites and not the chosen lattice.

A.6.4 Tissue strain calculation

We calculate the wavefront strain trace with a coarse-grained, stationary wave-back solution. Consider Eq. (A.6.3) in the limit $\eta/(\Gamma\Delta x^2) \ll 1$. We assume a steady state traveling wavefront $\epsilon(x,y,z,t) = \epsilon(x-vt,y,z)$ with a co-moving excitation front with velocity v driven by the activation condition solved above. Since the sites behind the wavefront are refractory, there are no other stress sources other than the activation front. The equations of motion then become

$$-v\partial_x\epsilon_{kk}(x-vt,y,z) = D\partial^2\epsilon_{kk}(x-vt,y,z) - \frac{\sigma^*_{ij}}{\Gamma}\partial_i\partial_j\sum_a \delta^3(x-x_a-vt,y-y_a,z-z_a). \tag{A.6.29}$$

where $D = \frac{\phi^2 E(1-\nu)}{\Gamma(1+\nu)(1-2\nu)}$, $\sigma^*_{ij} = T^{\text{out}}_{ijkl}\epsilon^*_{kl}$ the stress generated in the matrix by each contracting myocyte, and a the activated sites. Assuming a cubic lattice in the co-moving frame, the number of activated sites N in x corresponds to the width of the activated front, $N = v\tau/\Delta x$. So we take

$$\sum_a = \sum_{n^x,n^y,n^z} \tag{A.6.30}$$

where $n^x \in \{1,\ldots,N\}, n^y, n^z \in \{-\infty,\ldots,\infty\}$. In co-moving Fourier space, we find that the strain trace becomes

$$\tilde{\epsilon}_{kk} = \left(-ivk_x - k^2D\right)^{-1}\frac{\sigma^*_{ij}k_ik_j}{\Gamma}\sum_{n^x,n^y,n^z} e^{-i\Delta x(k_xn^x+k_yn^y+k_zn^z)}. \tag{A.6.31}$$

To compute the tissue-scale limit, we coarse-grain the system and consider length scales $1/|k| \gg \Delta x$. We can then express the sum over all activated sites as

$$\sum_{n^x,n^y,n^z} e^{-i\Delta x(k_x n^x + k_y n^y + k_z n^z)} = \frac{1}{(\Delta x)^3}\left(\sum_{n^x=0}^{N} \Delta x e^{-in^x k_x \Delta x}\right)\left(\sum_{n^y,n^z=-\infty}^{\infty} (\Delta x)^2 e^{-i(n^y k_y + n^z k_z)\Delta x}\right). \tag{A.6.32}$$

We then replace the sums with integrals. Let us call $x' = n^x \Delta x, y' = n^y \Delta x, z' = n^z \Delta x$, Δx the spacing between myocytes. In the continuum limit:

$$\frac{1}{(\Delta x)^3}\int_{-v\tau}^{0} dx' e^{-ik_x x'} \int_{-\infty}^{\infty} dy' dz' e^{-i(k_y y' + k_z z')} = \frac{(2\pi)^2}{ik_x(\Delta x)^3}\left[1 - e^{ik_x v\tau}\right]\delta(k_y)\delta(k_z). \tag{A.6.33}$$

Substituting this into (A.6.31), we observe that the infinite number of excitations in y and z only contribute in the infinite wavelength limit $k_y, k_z \to 0$ and these components are trivially integrated out. The inverse transform in k_x is a simple contour integral with poles no higher than second-order. Computing this gives the tissue scale response in terms of the individual CM excitation strength

$$\epsilon_{kk} = \frac{\sigma^*_{xx}}{D\Gamma(\Delta x)^3} \times \begin{cases} \exp\left(\frac{v}{D}(x - vt + v\tau)\right) & x < v(t-\tau) \\ 1 & v(t-\tau) < x < vt \end{cases} \tag{A.6.34}$$

where $\sigma^*_{xx}/(\Delta x)^3$ is associated with the microscopic stress exerted by each CM. The coefficient in Eq. (A.6.34) is the maximal tissue strain of the contracting wavefront. We note that this solution fails for $x > vt$ since for those positions the tissue is not

passive: CMs are primed for activation.

A.6.5 BGA obstructs intercellular transport in embryonic cardiac tissue

To verify that BGA properly interferes with gap junctions in embryonic CMs, we performed fluorescence recovery after photobleaching (FRAP) experiments to verify reduced intercellular transport between myocytes. Through α-actinin staining, we first verified that the cells of interest exhibited characteristic striations found in myocytes and myocyte precursors (Fig. A.9A). E4 chick hearts were loaded with calcein red-orange AM, a cell tracer. This compound is cleaved as it enters cells, rendering it membrane impermeable. Myocytes are selected within the tissue and bleached down to 20% of the initial intensity. Fluorescence recovery was recorded and analyzed via (software) and ImageJ (see Video A.14). Quantitative FRAP results are shown in Fig. A.9B-C. BGA-treated hearts systematically exhibited CMs (N=49) with significantly reduced fluorescence recovery in rate and intensity when compared to control (N=73), demonstrating that BGA does indeed interfere with gap junctions in E4 avian heart tissue. See Supplemental Methods.

A.6.6 Small-molecule drugs perfuse embryonic hearts

Treating embryonic hearts with blebbistatin, a drug that blocks myosin-II activity, disrupts the heartbeat (see Fig. A.10); the heartbeat is then rescued by mecarbil,

a cardiac-myosin force-enhancing drug (see Fig. A.11). This further indicates that many small-molecule drugs indeed perfuse the tissue given our experimental protocols and serves as a control for pharmacologically disrupted (and rescued) beating.

A.6.7 Supplemental Methods

Cell-on-gel FEM simulations

Finite element simulations were performed using the Structural Mechanics Module in COMSOL. An isolated hydrogel cultured cell was modeled as a hemisphere resting with its flat side fully in contact with a substrate. The substrate was also modeled as a hemisphere with the cell placed in the center of its flat surface (see Fig. A.5). The substrate radius was $10\Delta x$, large enough such that substrate boundary effects are negligible on cell strain. Both components were modeled as static linear elastic materials. Under cell contraction, the partial strain trace ($\epsilon_{2d} = \epsilon_{xx} + \epsilon_{yy}$) in the plane of the substrate surface was calculated and averaged over the cell's contact surface. This procedure was repeated for a range of values for the substrate Young's modulus. Both the saturating and constant eigenstrain models were used for the contraction strength of the cell. The "fine" option was used for the element mesh size to ensure convergence. See Table A.2 for a list of input parameters.

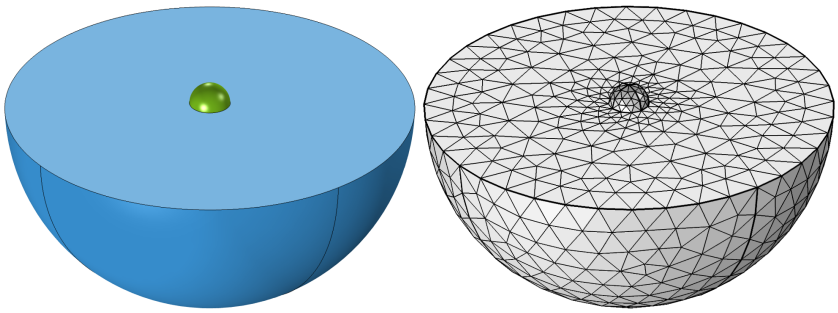

Figure A.5: Illustration and meshing of COMSOL finite element simulated "cell-on-gel" contraction. Active CM (green) contracts while adhered to matrices (blue) of variable stiffness. Chosen mesh is shown in gray. Maximal matrix strain trace is averaged over CM-matrix contact surface and shown in Fig. A.2A

Table A.2: FEM simulation parameter descriptions, symbols, and values

Description	Parameter	Value
Hemispherical cell radius	Δx	5μm
Hemispherical substrate radius	R	$10\Delta x$
Cell Young's modulus	E_c	0.75 kPa
Force saturation Young's modulus	E_s	E_c
Substrate Young's modulus	E	$[0.1 - 100]$ kPa
Poisson ratio	ν	0.4
Cell strain amplitude	ϵ^*	0.2

CMs-in-matrix FEM simulations

Finite element simulations were performed using the Structural Mechanics Module in COMSOL. Thirty six CMs were modeled as linear elastic spherical inclusions arranged in a cubic array and embedded within a surrounding elastic matrix of $30 \times 30 \times 40\mu m^3$ (see Fig. A.6), with all model parameters corresponding to Table A.2, except that the CM radius is set to $4.6\mu m < 5.0\mu m$ to prevent issues with meshing in the simulation. We then excited one of the centrally located CMs by inducing a contractile eigenstrain and com"cell-on-gel"puted the volume-averaged maximal strain induced

in the neighboring central CM as a function of effective tissue Young's modulus. The effective modulus was determined by simulated uniaxial tensile testing on the composite system. The "fine" element mesh size was used to ensure convergence. Note the excellent quantitative agreement between our analytical calculation and the finite-element calculations for finite-sized inclusions; this agreement justifies our approximation of CMs as point-like elastic inclusions.

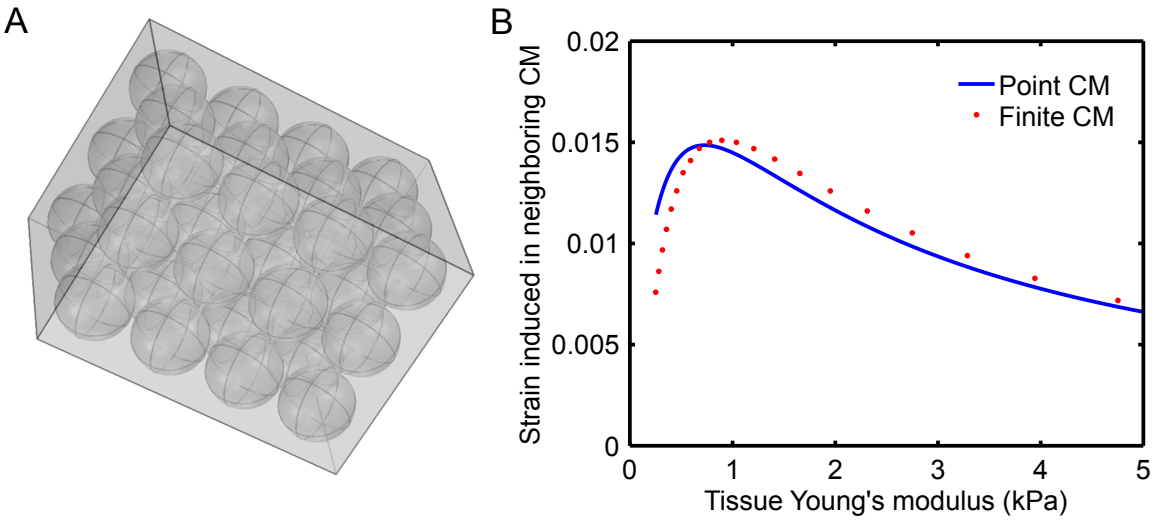

Figure A.6: Comparison of mechanical response between point-like and finite-sized CMs. We perform finite element simulations in COMSOL. We embed 36 elastic inclusions (CMs) within a surrounding elastic matrix, as shown in panel **A**. We impose a contractile eigenstrain in one of the centrally-located CMs. We plot (panel **B**) the maximum strain induced in the neighboring centrally-located CM against our analytic result for point-like CMs as a function of effective tissue Young's modulus. We observe good quantitative agreement between the two models, justifying our approximation of CMs as point-like elastic inclusions.

Myocardial stiffness measurements

White Leghorn chicken eggs (Charles River Laboratories) were incubated at 37C until the desired developmental stage was reached and isolated as described in [26].

Embryos were extracted at room temperature and placed into a Petri dish. The thick albumen was removed using blunt forceps and KimWipes. The embryos were adhered to a Whatman #2 filter paper with an elliptical hole of approximately 1 by 2 cm cut in it. The embryos were rinsed in PBS and placed ventral side up. Pre-warmed chick heart media (alpha-MEM supplemented with 10% FBS and 1% penn-strep, Gibco, 12571-063) was added at this point.

The heart was extracted with fine forceps severing above the atrium and below the outflow tract and transferred into a six-well plate. Micropipettes were pulled from glass capillaries (World Precision Instruments, Sarasota, FL) and broken to final inner diameters of 30-100 μm. Pipettes were filled with PBS and attached to water-filled reservoir. Aspiration was performed at room temperature in either PBS supplemented with 3% BSA or heart culture media. Before each experiment, pipette tips were placed in the solution for $\leq$ 20 min to prevent sticking. During aspiration, several pressures were applied in the range of 0 - 0.8 kPa. Imaging was done using a Nikon TE300 microscope with a 20x air objective and recorded using a Cascade Photometric CCD camera. Image analysis was performed in ImageJ.

Beta-glycyrrhetinic acid (BGA) fluorescence recovery after bleaching (FRAP)

Isolated day 4 embryonic hearts (E4) were stained with 0.5 μM CellTrace Calcein Red-Orange, AM (ThermoFisher Scientific #C34851) and Hoechst 33342 in HEPES buffered alpha-MEM culture media (Gibco #12571-063, supplemented with 10% FBS

and 1% penn-strep) for 15 minutes at RT with gentle rocking. Cytochalasin D (Cayman Chemical Company #11330, 25μM) was added to minimize contractions and drift during imaging. Calcein and Hoechst 33342 were then washed out three times with culture media supplemented with cytochalasin D. For BGA treatment, embryonic hearts preloaded with calcein were perfused in 100 μM 18-β-glycyrrhetinic acid (BGA, Cayman Chemical, 11845) for 1hr at RT, with gentle rocking. BGA-treated and untreated control hearts were placed on 35 mm glass bottom dishes (MatTek #P35G-1.5-10-C, Ashland, MA) with media filling up the center well and capped with a coverslip for FRAP imaging.

Confocal time-lapse images were acquired using a Zeiss 880 laser scanning confocal microscope equipped with a 40X oil 1.4NA objective. Zeiss ZEN Black software was configured to acquire images every 2 seconds for 6 min and photobleaching started after acquiring 8 frames and stopped until the intensity dropped to 20% of the original. Average intensity in each bleached region and a non-bleached region were measured by using ImageJ (`http://rsb.info.nih.gov/ij/download.html`) with the time series analyzer plugin (`http://rsb.info.nih.gov/ij/plugins/time-series.html`). Intensity of the bleached region was normalized to that of the non-bleached region in the same time series to correct overall photobleaching during imaging. Data was analyzed with a custom C++ code and graphs were plotted in GraphPad Prism version 6.0d (`http://www.graphpad.com`).

Immunostaining of embryonic hearts

Isolated day 4 embryonic hearts (E4) were fixed in 4% paraformaldehyde for 15 min at RT on a rocker. Fixed E4 hearts were then washed with PBS three times for 5 min each and permeabilized with 0.1% Triton-X in PBS for 30 min. Blocking was performed in 5% BSA and 0.1% Triton-X in PBS for 1.5 hrs at RT. Hearts were immunostained for α-actinin-2 (Abcam EA-53 mouse monoclonal Ab, 1:200 dilution in blocking solution) and DNA (Hoechst 33342, 1:1000) for 3 hours at RT with gentle shaking. Primary antibodies were washed out with PBS X3 for 15 min each. Secondary antibody (Goat anti-mouse IgG Atto565, Hypermol #2107, 1:500) staining was performed for 1.5 hours at RT and the hearts were washed with PBS X3 before confocal imaging. Images were acquired using a Zeiss 880 Airyscan confocal with a 40X oil 1.4NA objective. Image analysis was performed using ZEN Black software for Airyscan processing.

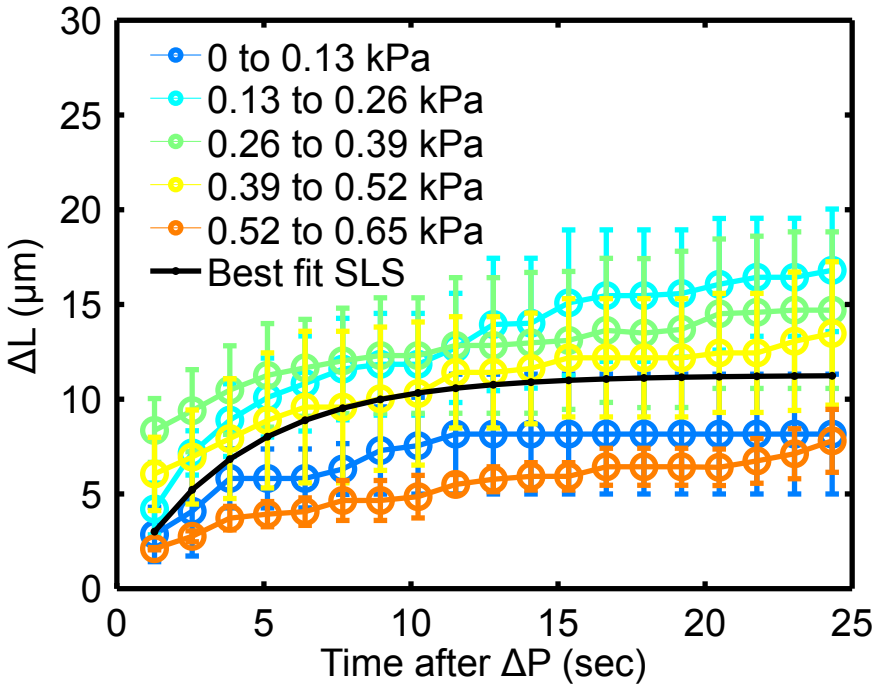

Figure A.7: Results from ramp-hold experiments performed on explanted HH stage 10-11 avian hearts. Pressure of micropipette applied to the tissue increases with increments of 0.13 kPa every 46 seconds. Excursion length differences as a function of pressure (indicated colors) and time after a pressure ramp (axis) are plotted. The best-fit standard linear solid (SLS) model is shown in black. For the majority of pressures applied, the heart behaves quantitatively as a linear viscoelastic material.

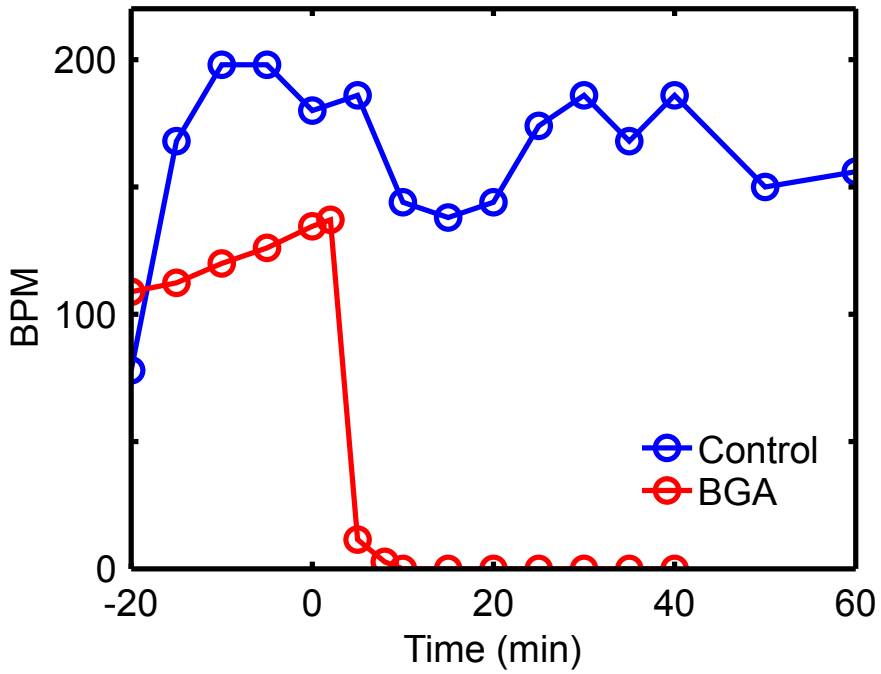

Figure A.8: BPM from isolated Langendorff perfused adult mouse heart control experiment shown with mean BPM from 3 adult hearts treated with 25 μM BGA (from Fig. A.4 in main text). BPM data was extracted from 20-second intervals of acquired video. This demonstrates the effectiveness of BGA on adult heartbeat disruption.

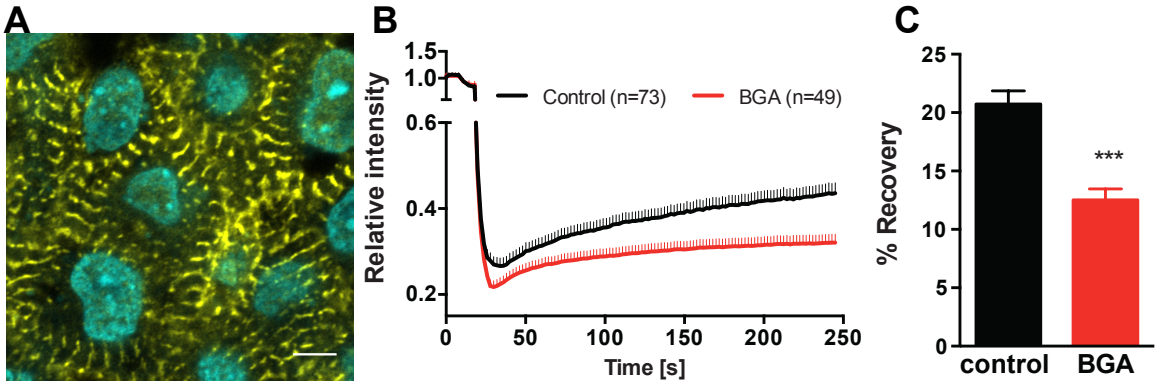

Figure A.9: Panel **A** displays a representative image of E4 chick embryonic CMs stained for α-actinin and DNA. Image was taken 4 μm below the surface in the outflow tract of the looping heart. Scale bar is 5 μm. As exampled here, CMs in the E4 heart exhibit premature periodic striations, suggesting myofibrillogenesis of cardiac myocytes. These cells were subjected to testing for effective gap junction interference via FRAP. Panel **B** shows aggregated results from calcein red-orange FRAP experiments in control and BGA-treated E4 avian hearts. Individual CMs within the tissue were selected and photobleached (see example Video A.14). Fluorescent intensity recovery was tracked over at four minutes in 49 +BGA CMs and 73 -BGA CMs. Rapid early recovery is likely due to intracellular diffusion and is unaffected by BGA treatment. In contrast, BGA treatment disrupts prolonged recovery, which is likely mediated by intercellular transport through gap junctions. Panel **C** demonstrates the significantly higher fluorescence recovery after four minutes in control hearts, demonstrating BGA efficacy in disrupting E4 avian heart gap junctions.

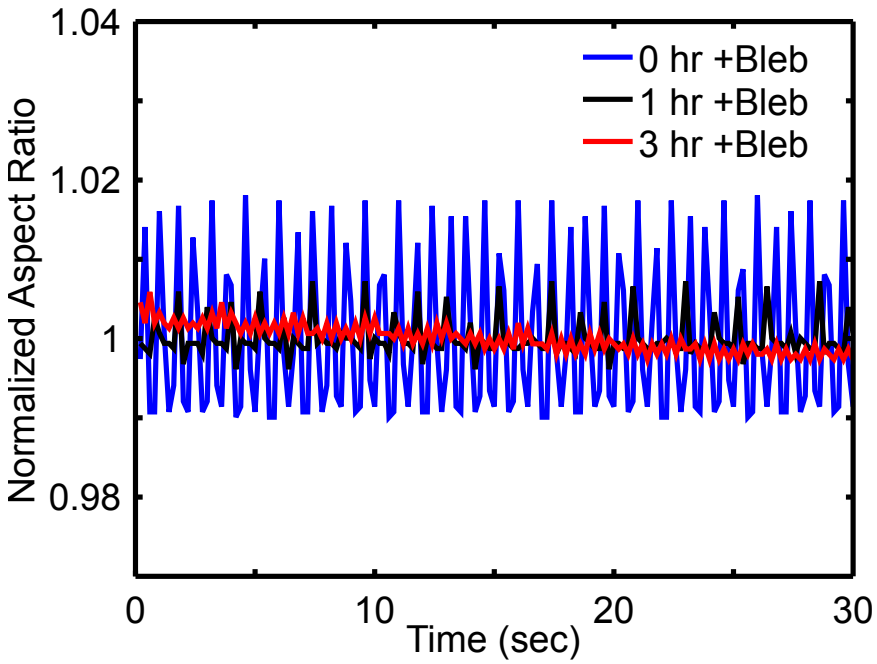

Figure A.10: Results from blebbistatin disruption on E4 chick heart. Mean-normalized aspect ratio is recorded over time intervals of 30s at time points 0hrs, 1hrs, and 3hrs after treatment of 20μM blebbistatin. Significant decreases in beating amplitude and BPM are observed.

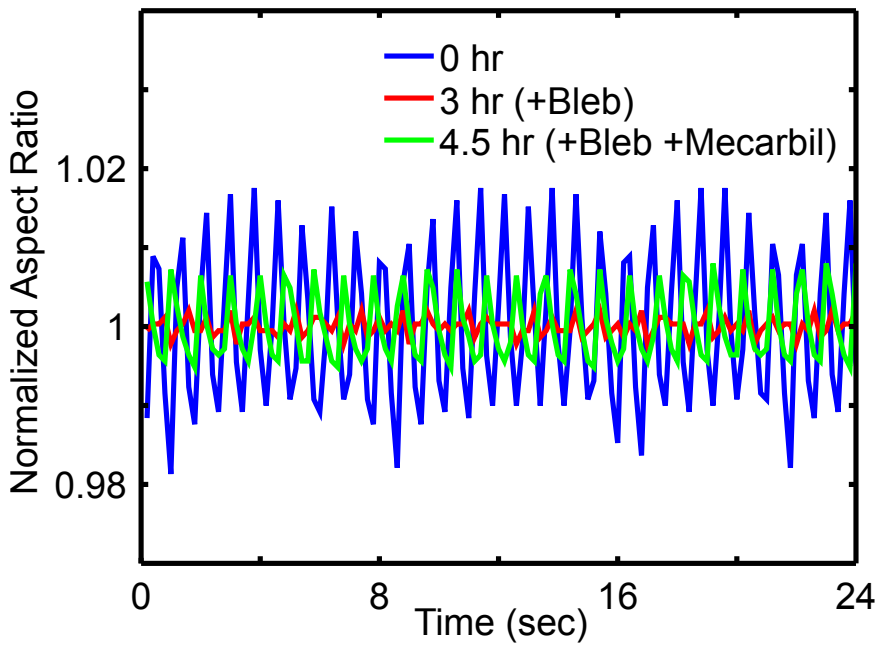

Figure A.11: Results from blebbistatin disruption with mecarbil rescue on E4 chick heart. Mean-normalized aspect ratio is recorded over 24s intervals at time points before drug treatment, post-blebbistatin, and post-blebbistatin and mecarbil. At $t = 0$hrs the heart tube is treated with 20 μM blebbistatin dilution to disrupt actomyosin activity. At $t = 3$hrs, the blebbistatin solution is removed via aspiration and replaced with 1 μM mecarbil to enhance cardiac myosin activity. We observe rescued beat amplitude and coherence. This also demonstrates effective small molecule perfusion into isolated embryonic hearts. Additionally, force-enhancing rescue of beats is consistent with a mechanical signaling model.

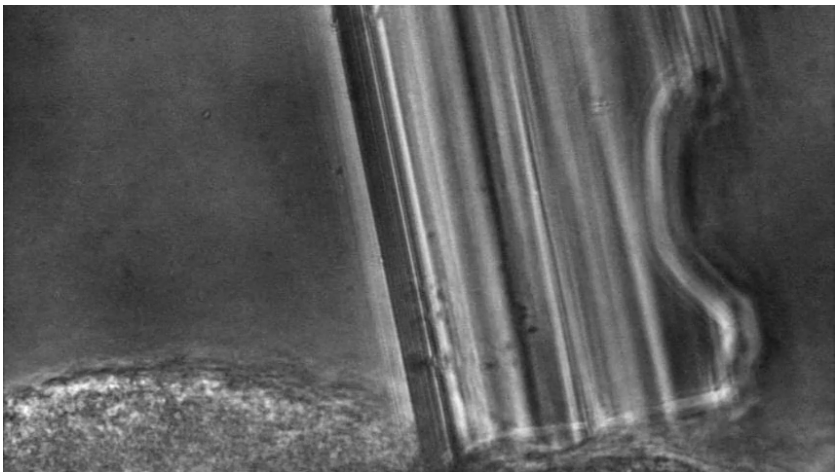

Figure A.12: Video of HH stage 10-11 (E1.5-2) chick hearts pre- and post-onset of beating. Pre-beating hearts exhibit "shivering" behavior of uncoordinated cardiomyocyte contractions. Post-beating hearts exhibit fully coordinated beats. Video plays at 3x real-time. Micropipette in view has an outer diameter of $\sim 50\mu$m (Note: Video can be found in Ref. [6]).

Figure A.13: Video of Langendorff-perfused adult mouse hearts pre- and post-administration of 25μM BGA drug dilution. Time points shown are -20min, 0min and +7min relative to BGA treatment (Note: Video can be found in Ref. [6]).

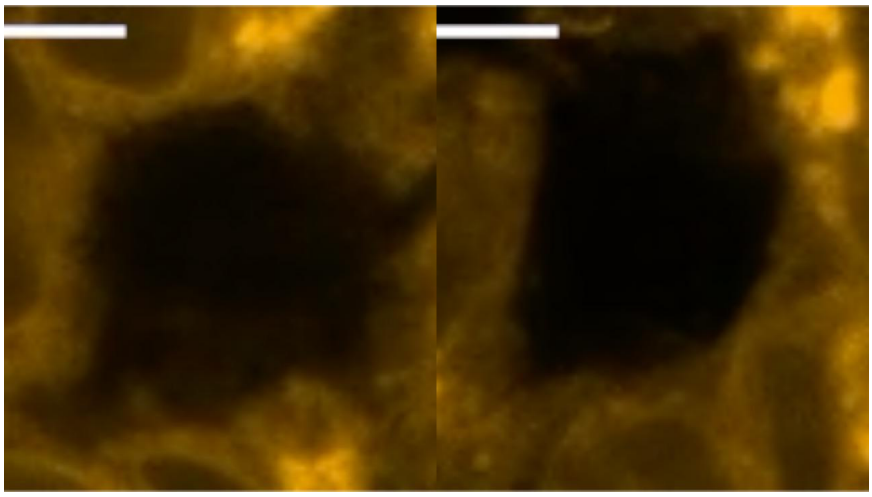

Figure A.14: Video comparison of FRAP experiments on calcein-labeled CMs in E4 hearts in control and BGA conditions. The left video demonstrates fluorescence recovery under control conditions, while the right corresponds to a BGA-treated heart. Scale bars are 5 μm. Videos are over the course of four minutes and synchronized to the onset of photobleaching (Note: Video can be found in Ref. [6]).

Bibliography

[1] Banerjee, S. and Marchetti, M. C. 2011. Instabilities and oscillations in isotropic active gels. *Soft Matter*, 7(2): 463–473.

[2] Bhana, B., Iyer, R. K., Chen, W. L. K., *et al.* 2010. Influence of substrate stiffness on the phenotype of heart cells. *Biotechnology and Bioengineering*, 105(6): 1148–1160.

[3] Bischofs, I. B. and Schwarz, U. S. 2003. Cell organization in soft media due to active mechanosensing. *Proceedings of the National Academy of Sciences*, 100(16): 9274–9279.

[4] Böhmer, C., Kirschner, U., and Wehner, F. 2001. 18-β-Glycyrrhetinic Acid (BGA) as an electrical uncoupler for intracellular recordings in confluent monolayer cultures. *Pflügers Archiv*, 442(5): 688–692.

[5] Burridge, P. W., Keller, G., Gold, J. D., and Wu, J. C. 2012. Production of De Novo Cardiomyocytes:Human Pluripotent Stem Cell Differentiationand Direct Reprogramming. *Cell Stem Cell*, 10(1): 16–28.

[6] Chiou, K. K., Rocks, J. W., Chen, C. Y., *et al.* 2016. Mechanical signaling coordinates the embryonic heartbeat. *Proceedings of the National Academy of Sciences*, 113(32): 8939–8944.

[7] Dasbiswas, K., Majkut, S., Discher, D. E., and Safran, S. A. 2015. Substrate stiffness-modulated registry phase correlations in cardiomyocytes map structural order to coherent beating. *Nature Communications*, 6: 6085.

[8] Davidson, J. S., Baumgarten, I. M., and Harley, E. H. 1986. Reversible inhibition of intercellular junctional communication by glycyrrhetinic acid. *Biochemical and Biophysical Research Communications*, 134(1): 29–36.

[9] Dawson, S. P., Keizer, J., and Pearson, J. E. 1999. Fire–diffuse–fire model of dynamics of intracellular calcium waves. *Proceedings of the National Academy of Sciences*, 96(11): 6060–6063.

[10] Dealy, C. N., Beyer, E. C., and Kosher, R. A. 1994. Expression patterns of mRNAs for the gap junction proteins connexin43 and connexin42 suggest their involvement in chick limb morphogenesis and specification of the arterial vasculature. *Developmental Dynamics*, 199(2): 156–167.

[11] DeVille, R. E. L. and Peskin, C. S. 2008. Synchrony and asynchrony in a fully stochastic neural network. *Bulletin of mathematical biology*, 70(6): 1608–1633.

[12] DuFort, C. C., Paszek, M. J., and Weaver, V. M. 2011. Balancing forces: architectural control of mechanotransduction. *Nature reviews Molecular cell biology*, 12(5): 308.

[13] Engler, A. J., Carag-Krieger, C., Johnson, C. P., *et al.* 2008. Embryonic cardiomyocytes beat best on a matrix with heart-like elasticity: scar-like rigidity inhibits beating. *Journal of Cell Science*, 121(Pt 22): 3794–802.

[14] Gourdie, R. G., Green, C. R., Severs, N. J., Anderson, R. H., and Thompson, R. P. 1993. Evidence for a distinct gap-junctional phenotype in ventricular conduction tissues of the developing and mature avian heart. *Circulation Research*, 72(2): 278–289.

[15] Gourdie, R. G., Kubalak, S., and Mikawa, T. 1999. Conducting the embryonic heart: orchestrating development of specialized cardiac tissues. *Trends in Cardiovascular Medicine*, 9(1-2): 18–26.

[16] Guevorkian, K., Gonzalez-Rodriguez, D., Carlier, C., Dufour, S., and Brochard-Wyart, F. 2011. Mechanosensitive shivering of model tissues under controlled aspiration. *Proceedings of the National Academy of Sciences*, 108(33): 13387–13392.

[17] Hazeltine, L. B., Simmons, C. S., Salick, M. R., *et al.* 2012. Effects of substrate mechanics on contractility of cardiomyocytes generated from human pluripotent stem cells. *International Journal of Cell Biology*, 2012.

[18] Hersch, N., Wolters, B., Dreissen, G., *et al.* 2013. The constant beat: cardiomyocytes adapt their forces by equal contraction upon environmental stiffening. *Biology Open*, 2(3): 351–361.

[19] Hu, Z., Metaxas, D., and Axel, L. 2003. In vivo strain and stress estimation of the heart left and right ventricles from MRI images. *Medical Image Analysis*, 7(4): 435–444.

[20] Idema, T. and Liu, A. J. 2014. Mechanical signaling via nonlinear wavefront propagation in a mechanically excitable medium. *Physical Review E*, 89(6): 62709.

[21] Iribe, G., Ward, C. W., Camelliti, P., *et al.* 2009. Axial stretch of rat single ventricular cardiomyocytes causes an acute and transient increase in Ca2+ spark rate. *Circulation Research*, 104(6): 787–795.

[22] Jacot, J. G., McCulloch, A. D., and Omens, J. H. 2008. Substrate stiffness affects the functional maturation of neonatal rat ventricular myocytes. *Biophysical journal*, 95(7): 3479–87.

[23] Kanno, S. and Saffitz, J. E. 2001. The role of myocardial gap junctions in electrical conduction and arrhythmogenesis. *Cardiovascular pathology*, 10(4): 169–177.

[24] Keith, A. and Flack, M. 1906. The auriculo-ventricular bundle of the human heart. *The Lancet*, 168(4328): 359–364.

[25] Le, A.-C. N. and Musil, L. S. 1998. Normal differentiation of cultured lens cells after inhibition of gap junction-mediated intercellular communication. *Developmental biology*, 204(1): 80–96.

[26] Majkut, S., Idema, T., Swift, J., *et al.* 2013. Heart-specific stiffening in early embryos parallels matrix and myosin expression to optimize beating. *Current Biology*, 23(23): 2434–9.

[27] McCain, M. L., Lee, H., Aratyn-Schaus, Y., Kléber, A. G., and Parker, K. K. 2012. Cooperative coupling of cell-matrix and cell–cell adhesions in cardiac muscle. *Proceedings of the National Academy of Sciences*, 109(25): 9881–9886.

[28] Mikawa, T. and Hurtado, R. 2007. Development of the cardiac conduction system. In *Seminars in Cell & Developmental Biology*, volume 18, pages 90–100. Elsevier.

[29] Mirollo, R. E. and Strogatz, S. H. 1990. Synchronization of pulse-coupled biological oscillators. *SIAM Journal on Applied Mathematics*, 50(6): 1645–1662.

[30] Mow, V. C., Kuei, S. C., Lai, W. M., and Armstrong, C. G. 1980. Biphasic Creep and Stress Relaxation of Articular Cartilage in Compression: Theory and Experiments. *Journal of Biomechanical Engineering*, 102(1): 73.

[31] Mura, T. 1987. Isotropic inclusions. In *Micromechanics of Defects in Solids*, pages 74–128. Springer.

[32] Nash, M. P. and Panfilov, A. V. 2004. Electromechanical model of excitable tissue to study reentrant cardiac arrhythmias. *Progress in Biophysics and Molecular Biology*, 85(2-3): 501–522.

[33] Nitsan, I., Drori, S., Lewis, Y. E., Cohen, S., and Tzlil, S. 2016. Mechanical communication in cardiac cell synchronized beating. *Nature Physics*, 12(5): 472.

[34] Panfilov, A. V., Keldermann, R. H., and Nash, M. P. 2007. Drift and breakup of spiral waves in reaction–diffusion–mechanics systems. *Proceedings of the National Academy of Sciences*, 104(19): 7922–7926.

[35] Prosser, B. L., Ward, C. W., and Lederer, W. J. 2011. X-ROS signaling: rapid mechano-chemo transduction in heart. *Science*, 333(6048): 1440–1445.

[36] Rapila, R., Korhonen, T., and Tavi, P. 2008. Excitation–contraction coupling of the mouse embryonic cardiomyocyte. *The Journal of General Physiology*, 132(4): 397–405.

[37] Salameh, A., Wustmann, A., Karl, S., *et al.* 2010. Cyclic mechanical stretch induces cardiomyocyte orientation and polarization of the gap junction protein connexin43. *Circulation Research*, 106(10): 1592–1602.

[38] Sasse, P., Zhang, J., Cleemann, L., *et al.* 2007. Intracellular Ca2+ oscillations, a potential pacemaking mechanism in early embryonic heart cells. *The Journal of General Physiology*, 130(2): 133–144.

[39] Sato, T., Nishishita, K., Okada, Y., and Toda, K. 2009. Effect of Gap Junction Blocker β-Glycyrrhetinic Acid on Taste Disk Cells in Frog. *Cellular and Molecular Neurobiology*, 29(4): 503–512.

[40] Shaw, J., Izu, L., and Chen-Izu, Y. 2013. Mechanical analysis of single myocyte contraction in a 3-D elastic matrix. *PLoS One*, 8(10): e75492.

[41] Stacy Jr, G. P., Jobe, R. L., Taylor, L. K., and Hansen, D. E. 1992. Stretch-induced depolarizations as a trigger of arrhythmias in isolated canine left ventricles. *American Journal of Physiology-Heart and Circulatory Physiology*, 263(2): H613—-H621.

[42] Tang, X., Bajaj, P., Bashir, R., and Saif, T. A. 2011. How far cardiac cells can see each other mechanically. *Soft Matter*, 7(13): 6151–6158.

[43] Thompson, S. A., Copeland, C. R., Reich, D. H., and Tung, L. 2011. Mechanical coupling between myofibroblasts and cardiomyocytes slows electric conduction in fibrotic cell monolayers. *Circulation*, 123(19): 2083–2093.

[44] Thompson, S. A., Blazeski, A., Copeland, C. R., *et al.* 2014. Acute slowing of cardiac conduction in response to myofibroblast coupling to cardiomyocytes through N-cadherin. *Journal of Molecular and Cellular Cardiology*, 68: 29–37.

[45] Vinnakota, K. C. and Bassingthwaighte, J. B. 2004. Myocardial density and composition: a basis for calculating intracellular metabolite concentrations. *American Journal of Physiology-Heart and Circulatory Physiology*, 286(5): H1742—-H1749.

[46] Vogel, V. and Sheetz, M. 2006. Local force and geometry sensing regulate cell functions. *Nature Reviews Molecular Cell Biology*, 7(4): 265.

[47] von Zglinicki, T. and Bimmler, M. 1987. The intracellular distribution of ions and water in rat liver and heart muscle. *Journal of microscopy*, 146(1): 77–85.

[48] Wang, N., Tytell, J. D., and Ingber, D. E. 2009. Mechanotransduction at a distance: mechanically coupling the extracellular matrix with the nucleus. *Nature Reviews Molecular Cell Biology*, 10(1): 75.

[49] Wiens, D., Jensen, L., Jasper, J., and Becker, J. 1995. Developmental expression of connexins in the chick embryo myocardium and other tissues. *The Anatomical Record*, 241(4): 541–553.

[50] Wozniak, M. A. and Chen, C. S. 2009. Mechanotransduction in development: a growing role for contractility. *Nature Reviews Molecular Cell Biology*, 10(1): 34.

[51] Xia, Y. and Nawy, S. 2003. The gap junction blockers carbenoxolone and 18β-glycyrrhetinic acid antagonize cone-driven light responses in the mouse retina. *Visual Neuroscience*, 20(4): 429–435.